Systèmes luminescents BaTiO3 : Ln(Ln= Er3+, Yb3+, Eu3+) préparés par chimie douce : poudres, nanopoudres et films nanostructurés

Margarita Garcia-Hernandez

N° d'Ordre: D.U. 2040

UNIVERSITE BLAISE PASCAL
U.F.R. Sciences et Technologies

ECOLE DOCTORAL DES SCIENCES FONDAMENTALES
N° 649

THESE en Cotutelle

présentée pour obtenir le grade de

DOCTEUR D'UNIVERSITE

Spécialité : Chimie, Science des Matériaux

Par **Margarita GARCIA-HERNANDEZ**
Titulaire du Master of Science on Chemistry

"Luminescent system of Ln (Ln=Er^{3+}; Yb^{3+}, Eu^{3+}) doped $BaTiO_3$ nanostructured powders and films prepared by soft chemical routes"

Soutenue publiquement le 29 juin 2010 devant la commission d'examen.

Président:	Mohamed BOUAZAOUI
Rapporteurs:	Felipe CARRILLO-ROMO
	Mohamed BOUAZAOUI
Examinateurs:	Antonieta GARCIA-MURILLO
	Geneviève CHADEYRON
Invités:	Damien BOYER
	Rachid MAHIOU

DEDICATION

I dedicate this thesis to my parents: Antonio and Rafaela, to my brothers and sister: Alejandro, Antonio and Isabel. And, to my director of thesis: Geneviève, Felipe and Antonieta.

Acknowledgements

This work was realized in cotutelle between Research Center of Applied Science and Advanced Technology of the National Polytechnic Institute of Mexico and Inorganic Material Laboratory of Blaise Pascal University of France.

I am grateful to CONACYT financial support of projects 59408 and 100764, National Polytechnic Institute (SIP20100090 and 20100091) and Institutional Program by the research's formation (PIFI-IPN) for the financial support. Also, I would like to acknowledge to EGIDE-530901H for Ph.D scholarship grant in its program Eiffel-doctorat during the stage in the Inorganic Materials Laboratory of Blaise Pascal University in Clermont-Ferrand, France.

I would like to send my sincere thanks to the director of laboratory, Professor Rachid MAHIOU to accept me to his laboratory. I wish to express my inner thankfulness to the directors of the thesis, Genevieve CHADEYRON and Antonieta GARCIA-MURILLO for their valuable and kind suggestions throughout all this research.

Professor Mohamed BOUAZAOUI Ph. D (Researcher of Lille University, France) and Professor Felipe de Jesus CARRILLO-ROMO (Researcher of National Polytechnic Institute, Mexico) accepted to examine this work as reporters and members of the jury. I thank them strongly for their helpful advices and observations.

I would like to express my gratefulness to members of the jury that they accepted to judge this work: Antonieta GARCIA-MURILLO, Geneviève CHADEYRON, Damien BOYER and Rachid MAHIOU.

I would also like to say thank you to the different institutions and professors who supported this work in the side of experimental techniques: Joël CELLIER, Nathalie GAILLARD-CAPERAA and Rodolphe THIROUARD (LMI-UBP); Thierry ENCINAS (ENSCCF); Marco Antonio MENESES-NAVA, Oracio C. BARBOSA-GARCIA and Martin OLMOS-LOPEZ (CIO, A. C.); Humberto and Mauricio TERRONES-MALDONADO and Daniel RAMIREZ GONZALEZ (IPICYT); Salvador

PALOMARES-SANCHEZ (UASLP), Pascual BARTOLO (CINVESTAV Merida); Vicente GARIBAY-FEBLES, Nicolas CAYETANO-CASTRO and Joel RAMIREZ-SALGADO (IMP) and finally Leticia TORRES (UANL).

I would like to thank at my director of thesis and good friend, Professor Antonieta GARCIA-MURILLO. Without her constant help, direction and encouragement, I would not be where I am today. She believed in me when I began in this way. For this and so more, I am truly grateful.

Finally, I wish to express my greatest gratitude to my parents (Antonio and Rafaela) and my brothers and sister (Alejandro, Antonio and Isabel) for their unlimited support in all moment.

Thank you!

Summary

This work is devoted to the synthesis as well as the structural, morphological and optical characterizations of barium titanate matrices ($BaTiO_3$) doped with Eu^{3+}, Er^{3+} and Yb^{3+} ions. Three synthesis ways have been investigated: sol-gel, hydrothermal and solid state.

It has been shown that the hydrothermal one leads to nanometric powders constituted of 20 nm particles, ten times smaller than the ones obtained in powders prepared by classic solid state synthesis. Synthesis dependence of crystallographic structure of titanates has been evidenced. Adding of chelating agents during the synthesis of sol-gel process enables to modify the morphology of powders and stabilize the sols dedicated to coating achievements. Monolayer thick coatings (800 nm) of Er^{3+} and Eu^{3+} doped barium titanates were obtained through this route. A study of optical properties related to rare earth ions in these different matrices was performed by recording the excitation and emission spectra. Energy transfer processes between rare earth ions have been investigated in co-doped compounds.

Several characterization techniques have been used to assess the purity, the structure and the morphology of powders and films of barium titanates: infrared and Raman spectroscopies, X-ray diffraction, thermogravimetric analysis, scanning and transmission electron microscopies.

Résumé

Ce travail concerne, la synthèse, la caractérisation structurale, morphologique et optique de matrices de titanates de baryum ($BaTiO_3$) activées par les ions Eu^{3+}, Er^{3+} et Yb^{3+}. Trois voies de synthèse sont étudiées : sol-gel, hydrothermale et solide.

Il a été montré que la synthèse hydrothermale conduisait à des poudres nanométriques constituées de particules de 20 nm, dix fois plus petites que celles rencontrées dans les poudres obtenues par les techniques classiques de céramisation. L'influence de ce paramètre sur la structure cristallographique des titanates a pu être mise en évidence. L'ajout d'agents chélatants au cours de la synthèse sol-gel permet de modifier la morphologie des poudres et de stabiliser les sols destinés à l'élaboration de revêtements. Des films épais monocouche (800 nm) de titanates de baryum dopés Er^{3+} et Eu^{3+} ont ainsi été obtenus. Une étude des propriétés optiques des ions de terres rares dans les différents systèmes synthétisés a été menée en enregistrant les différents spectres d'excitation et d'émission. Les phénomènes de transfert d'énergie entre les ions de terres rares ont été étudiés dans les matrices co-dopées.

Plusieurs techniques de caractérisations ont été mises en œuvre pour évaluer la pureté, la structure et la morphologie des poudres et films de titanates de baryum préparés : spectroscopies infra rouge et Raman, diffraction des rayons X, analyse thermogravimétrique, microscopies électroniques à balayage et à transmission.

Table of Contents

Chapter 3. Luminescence

Chapter 4. Synthesis of $BaTiO_3$ doped with rare earth ions (Eu, Er, Yb)

Chapter 5. Results and discussion

List of Figures

CHAPTER 3

CHAPTER 4

CHAPTER 5

List of Tables

Chapter 1. Introduction

1.1 Host matrix

Perovskites compounds with formula ABO_3 are technologically important materials due to their great use in the fabrication of electronic components as capacitors, multilayer ceramics, thermistors, etc. [1,2]. $BaTiO_3$, $SrTiO_3$ and $CaTiO_3$, among others are examples of perovskite materials; in the case of $BaTiO_3$ systems, the unit cell in ABO_3 structure, the A atoms are at (0 0 0); the B atoms are at (½, ½, ½) ante three O atoms at (0, ½, ½); (½, 0, ½); (½, ½, 0). Figure 1-1 shows the unit cell of $BaTiO_3$ of perovskite structure where atom B for Ti^{4+} sits in the center of cube.

The stability of the perovskite compounds arises mainly of the electrostatic charge of the ions perfectly integrated [3].

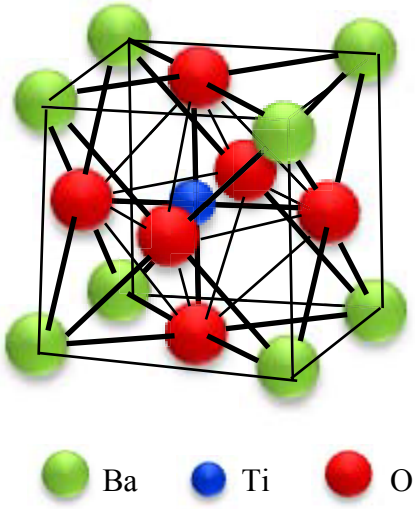

Figure 1-1. *Cubic structure of $BaTiO_3$; lattice constant a=4.0165Å with symmetry* Oh.

The perovskite structure of $BaTiO_3$, is recognized due to its dielectric properties, this present 5 polymorphic cases. The structural transitions observed are: tetragonal→cubic →hexagonal, theses phases are observed successively from 120 °C to 1460 °C.

For lower temperatures, the orthorhombic structure is observed in the range 0-90 °C, below this, the rhombohedral phase is presented. A general scheme of the structural transitions is presented in Table 1-1 including spatial groups for each phase.

Table 1-1. *Structural transitions of $BaTiO_3$.*

Ref.	Phase	Temperature	Spatial Group
[4]	**Hexagonal**	> 1460 °C	$P6_3/mmc$
[5]	**Cubic**	120- 1460 °C	$Pm\bar{3}m$
[3]	**Tetragonal**	0-120 °C	$P4mm$
[3]	**Orthorhombic**	-90-0 °C	$Amm2$
[3]	**Rhombohedral**	< 90 °C	$R3m$

The pure $BaTiO_3$ system is difficult to obtain, although good quality is obtained when the stoichiometric calculations are done and this is the origin of high quality crystalline growth. The tetragonal ferroelectric $BaTiO_3$ have been investigated in the last decades due to the potential applications in electronics and optics devices, these properties are provided with the stable phase at room temperature. However, studies related to the $BaTiO_3$ structure have reported the relationship between particle size and crystalline structure, i.e, it has been found that it is possible to obtain the cubic phase at room temperature, if particle's size is less than 50 nm as proposed by different authors Strek and Zhang at. al. [6,7] an approximately 38 nm by J. Amami [8].

The method of elaboration for $BaTiO_3$ represents a crucial aspect related with particle size and crystalline structure. The conventional method for preparation of this material is generally solid state reaction at high temperature (1100-1300 °C) [9], resulting in cost increase. An alternative is to use soft techniques due to the multiples advantages over

conventional techniques. The sol-gel process is an appropriate method for the preparation of $BaTiO_3$, due to the possibility to produce crystalline materials at low temperatures, therefore, powders and films with high homogeneity and purity are possible to obtain. However, the hydrothermal and solid state reactions are valuable methods to compare the final properties of $BaTiO_3$.

J. H. Lee et. al [10], synthesized $BaTiO_3$ powders by hydrothermal method using a molar ratio Ba/Ti=1, the temperature was fixed at 180 °C. The structure of $BaTiO_3$ obtained was tetragonal presenting a particle size of around 0.3 μm. Agglomeration of powders was difficult to control using their experimental conditions.

T. Fukui et. al. [11] prepared $BaTiO_3$ powders using metal alkoxide methods. A complex alkoxide used as a precursor was hydrolyzed; to obtain submicrometer powders of perovskite compounds were obtained. The simultaneous use of a dipolar aprotic solvent, such as acetone with ethanol was found to be effective for the preparation of the nearly spherical powders with submicrometer diameter (0.7-1.6 μm). The $BaTiO_3$ powders presented cubic structure at 900 °C while tetragonal structure was obtained after 1100 °C. The $BaTiO_3$ submicrometer powders were formed through nucleation–aggregation, but not by the usual nucleation–grain growth.

An important investigation was reported by S. Doeuff et. al. [12], in which the molecular precursor modification of TiO_2 was analyzed, particularly using acetic acid during hydrolysis step. TiO_2 monolithic gels were obtained during titanium hydrolysis step in presence of acetic acid. In this case, the acetic acid was not catalyzed but leads a molecular modification of precursor and changed the hydrolysis process. The last process is important because, the titanium precursor is the essential component for the elaboration of barium titanate and it is indispensable to control due to its high reactivity.

Another study was reported by Madona Boulos et. al. [13] in 2005, which revealed the elaboration of $BaTiO_3$ nanoparticles (20 nm in size) for electronic applications using hydrothermal method. In this work the cubic phase of $BaTiO_3$ nanoparticles was obtained, in agreement with Amami et. al. studies [8]. Amami proposed that it is possible to obtain cubic phase of $BaTiO_3$ when the particle size is less than 30 nm.

On the other side, $BaTiO_3$ powder and film studies have been reported at low temperatures of synthesis showing good electronic properties. Therefore, when some rare earth ions doped barium titanate it is possible to obtain luminescent properties, Nowadays, the rare earth ions are added to a wide variety of metallic oxides in order to improve electric, electronic, magnetic and optical properties [14,15].

1.2 Emission properties of rare earth ions: ytterbium, erbium and europium

The lanthanide elements are the group of elements with atomic number increasing from 58 (cerium) to 71 (lutetium). They are termed lanthanide because the lighter elements in the series are chemically similar to lanthanum. The electronic structure of the lanthanide elements, with minor exceptions is $[Xe]6s^2 4f^n$. In their compounds, the 6s electrons are lost and the ions have the configuration $[Xe]4f^m$ [16].The chemistry of the lanthanides differs from main group elements and transition metals because of the nature of the 4f orbitals. These orbitals are "buried" inside the atom and are shielded from the atom's environment by the 4d and 5p electrons. All the lanthanide elements exhibit the oxidation state +3. In addition Ce^{3+} can lose its single f electron to form Ce^{4+} with the stable electronic configuration of xenon. Also, Eu^{3+} can gain an electron to form Eu^{2+} with the f^7 configuration which has the extra stability of a half-filled shell. The similarity in ionic radius between adjacent lanthanide elements makes it difficult to separate them from each other in naturally occurring ores and other mixtures. The trivalent lanthanides mostly form ionic salts. This makes them suitable for use in lasers as it makes the population inversion easy to achieve. The Nd:YAG laser is one that is widely used [17]. Lanthanide ions are also fluorescent as a result of the forbidden nature of f-f transitions. Europium-doped yttrium vanadate was the first red phosphor to enable the development of color television screens [18].

Ytterbium, erbium and europium ions of atomic numbers 70, 68 and 63 respectively form the rare earths group. The trivalent ions are hard acceptors and form more stable complexes with oxygen-donor ligands than with nitrogen-donor ligands [19]. As f-f transitions are forbidden, once an electron has been excited, decay to the ground state will be slow [20].

The effect of synthesis method and grain size is very important in the properties of $BaTiO_3$ and is manifested in the change of all them: phase transition temperature, crystalline structure, non-lineal properties, between others [21]. Recently, has been reported the efficiency of the europium ion as structural probe in the crystalline structure of $BaTiO_3$ [7]. The europium ion was employed due to their properties for structural probe; this property allows to study the structural phase from luminescent view point in synthesis as hydrothermal. From this method nanoparticles are obtained. The europium ion excitation is the Uv region, in 356 nm and its characteristic emission is about 611 nm, red region. Figure 1-2 it is shown the relationship between synthesis method and particle size obtained through each one of them. Also it is presented the excitation source and their characteristic emission in the red region.

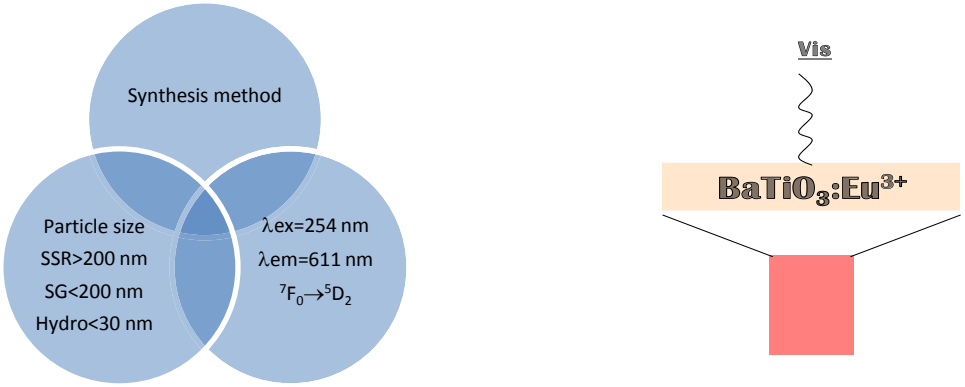

Figure 1-2. *Relationship between the methods and particles sizes for elaboration of $BaTiO_3$(a): Solid State Reaction (SSR), Sol-Gel (SG) and Hydrothermal (Hydro) after excitation in the visible region of $BaTiO_3:Eu^{3+}$(b), for example after using λ_{ex}=254nm one emission is obtained at ~611 nm in the red region, being $^7F_0 \rightarrow {}^5D_2$ the characteristic transition of Eu^{3+} ions.*

Erbium doped barium titanate was studied by Jin Jun Hwang and Young Ho Han [22], these authors obtained the $BaTiO_3$ host matrix doped through organometallic compounds, denominated Pechini method. The as-prepared samples were polymerized and calcined. The powders were pulverized and then pressed for 5h at 1380 °C. These materials allowed the study of conductivity after doping at different erbium concentrations. The results shown that this compound present a minimum conductivity due to the acceptor dopant behavior when the erbium ion replace Ti, also it has been observed that an electronic compensation occurred in the cation vacancies after doping at 0.5 %mol because to the low solubility of the erbium ions in the barium.

In other report, the erbium doped barium titanate was studied by H. X. Zhang et. al. [23]. In this study the synthesis was by a sol-gel modification; specifically the $BaTiO_3$:Er^{3+} was prepared with acetate type precursors. The authors analyzed the luminescent properties, specifically the emission after 514 and 980 nm excitations. The luminescent measurements revealed a quenching for erbium concentration lower than 3.0 mol %. The quenching process can be explained by the energy transfer and relaxation processes between erbium sites presenting close packing.

W. Strek et. al. [7], prepared europium doped $BaTiO_3$ films by sol-gel method obtaining excellent luminescent properties after doping the matrix at 0.5, 1 and 2 % mol, exhibiting low decay times, also, it was analyzed the structural transition phase of $BaTiO_3$ nanocristalline particles by means of fluorescence spectroscopy using Eu^{3+} ions as optical structural probe.

J. Amami et. al. [8,24] in 2006 and 2007 prepared $BaTiO_3$:Yb^{3+} powders with particle sizes of about 20 and 60 nm by sol-gel method. In this case the luminescent properties were studied; the ytterbium ion performed the function of optical structural probe revealing the cubic and tetragonal coexistence of structural phases with size between 30 to 60 nm. This result was estimated through the second harmonic generation study.

Nowadays, the decreasing particle size has been the main goal of many researchers, for example, Madona Boulos has synthesized $BaTiO_3$ particles with mean size of 20 nm as previously mentioned. Ersin E. Oren et. al. [25] in 2007, prepared pure barium titanate

particles and Dy doped barium titanate from experimental procedure proposed by Boulos, the result shown a pseudocubic phase with particle size of 22 nm, the Dy ions were employed to stabilized the cubic structure a room temperature.

1.3 Interest on codoped materials

The codoped materials are candidate for increase some luminescent properties in particular visible or infrared combined emission, this behavior is so different if only one ion is present as dopant. In a particular case, Er^{3+}-Yb^{3+} has been studied in some systems as YAG [26], obtained by precipitation. In this matrix energy transfers processes were presented in the codoped samples, consequently of this fact, red emissions were obtained and up conversion took place through a energetic transference of $^4I_{13/2}$ al $^4I_{9/2}$ level erbium ions. In this study the green emission in 550 nm was the high intense emission when is excited at 973 nm while after 816 nm excitation a quenching process was observed in the luminescent properties.

The purpose of the present research is to establish the methodology for the elaboration of Er^{3+}, Yb^{3+} codoped $BaTiO_3$ system to optimize the erbium ion concentration, to obtain high efficiency in the optical properties mainly in the luminescent properties, presenting red, blue and green emissions after different wavelength excitations. So far, only a few works of Er^{3+} and Yb^{3+} codoped $BaTiO_3$ powders has been reported [27]. Up conversion process are expected in this materials as was observed in YAG matrix [28,29].

1.4 Proposed research

1.4.1 Main goal

"Elaboration of rare-earth (Eu^{3+}, Er^{3+}, Yb^{3+}) doped $BaTiO_3$ powders, nanopowders and films with high optical efficiency to study the luminescent properties".

1.4.1 Specific goals

- Elaboration of $BaTiO_3$ system by three methods of synthesis: hydrothermal, solid state reaction and sol-gel processes.
- Study and comparison of structural and morphological properties of $BaTiO_3$ system prepared by hydrothermal route and solid state reaction.
- Study of structural and morphological properties of $BaTiO_3$ films obtained by sol-gel method and dip-coating technique.
- Analyses of the luminescent properties of the $BaTiO_3$:Eu^{3+} powders synthesized by hydrothermal route and solid state reaction and $BaTiO_3$:Er^{3+},Yb^{3+} powders obtained by sol-gel method.
- Analyses of the luminescent properties of Er^{3+} and/or Yb^{3+} doped and codoped $BaTiO_3$ films obtained by sol-gel method.

1.5 Organization of the work

The present work is organized in the following form: in chapter 2 it is described the theoretical aspects of the main stages involved in each synthesis method: sol-gel, hydrothermal and solid state reaction. In chapter 3, the general aspects about the luminescent are presented. In chapter 4, the experimental procedures used to obtain the nanopowder, powder, thin and thick films are detailed. In chapter 5, the results and discussion of structural and morphological properties of rare earth doped and/or codoped $BaTiO_3$ of powders, nanoparticles and thin and thick films are presented. In chapter 6, the optical properties of the obtained system are described. Finally, the conclusions of this work are given.

Chapter 2. Theoretical aspects of "Methods of Synthesis"

Previous to begin with the analyses of structural, morphological and optical properties for one specific material it is very important to establish the preparation technique since the physical and chemical properties depends on of the synthesis route used i.e. the size, crystalline structure and morphology of the particles are controlled by preparation method. Throughout this chapter, the synthesis methods used in this work are described below.

2.1 Sol-gel method

Sol-gel processing has been known for a long time, the first gels were made in 1845 by M. Ebelmen at the "Manufacture of Céramiques de Sévres" in France [30]. However this processing technique has known a very important development during the last two decades [31]. Sol-gel processes have brought a new view in the domain of glass and ceramics fabrication and they have enlightened the importance if chemistry involves the complete fabrication lines of materials, from initial chemical precursors to the final products. The basic idea is to progressively create an oxide network by polymerization reactions of chemical precursors dissolved in a liquid medium. Sols and gels are two forms of matter that have been known to exist naturally for a long time. They include various materials such as ink, clays, and a number of other substances such as the eye vitrea, blood, serum, and milk [32]. Sols and gels have raised scientific interest for a long time. The oldest sols

prepared in laboratory were synthesized with gold by Faraday in 1853. They are still stable nowadays [33].

Table 2-1. *Advantages and disadvantages of the sol-gel method.* [34]

Advantages	*Disadvantages*
✓ High homogeneity of the products compared with conventional method.	× Precursor expensive.
✓ High purity of the products obtained.	× Long time of reaction.
✓ Low temperatures of preparation: • Save energy. • Decrease the evaporation losses. • decrease air pollution • Possibility to control morphology and structural phases.	× Fine porous materials. × Presence of residual hydroxyl groups.
✓ Preparation of new amorphous materials out of normal range of obtaining temperatures.	× Residual carbon.
✓ Formation of crystalline phases from amorphous materials.	
✓ Better crystalline products from special properties of gels.	
✓ Preparation of thin films on different kind of substrate with excellent optical quality.	
✓ Possibility to control doping.	

The sol–gel technology started with processing of dense, bulk materials, and great effort has been made to densify porous gels into glasses and ceramics. However, recently sol–gel processing of mesoporous and macroporous materials has also attracted much attention, including materials with well-controlled pore characteristics and highly porous materials, which have excellent chemical and photonic functions. So far, the new processes satisfy the

requirements to elaborate new and better products [35,36]. By this method it is has been possible to produce submicrometer powders with high purity, nuclear fuel, ionic and electronic conductors and magnetic materials among others.

The sol-gel is a very effective and important process when it is required the production of homogeneous complexes ceramics reproducible as the new technologies demand. Though this, sol-gel process is an excellent option for producing high quality and purity materials, since grinding and compression operations are avoided and since temperatures involved does not exceed 150 °C, well below those used in conventional processes. For this reason the sol-gel method has been called "soft chemistry method." Some of the advantages and disadvantages of sol-gel method are presented in Table 2-1.

2.1.1 Chemistry and stages

Sols and inorganic gels can be obtained by several methods; these are often synthesized from chemical reagents dissolved in a liquid. The chemical reactants which can contain a cation M present in the sols or final inorganic gels are called *chemicals precursors.* Its chemical transformations are complex and involve a competition between the reaction at the molecular level responsible for the formation of open structures that lead to the formation of solids and dense materials. Some of these reactions are responsible for controlling the colloidal dispersion of the particles in the sol or avoid the agglomeration in the gel. There are two main groups of precursors: metal salts and alkoxides. The general formula of a metal salt is M_mX_n where M is the metal, X is the anion group and *m* and *n* the stoichiometric coefficients, an example is aluminum chloride, $AlCl_3$. In the case of alkoxides, the general formula M(OR)n, which indicates a combination of the cation M with n groups of alcohol ROH, an example is the aluminum ethoxide, Al $(OC_2H_5)_3$.

The solution chemistry of these two precursors is different, but the selection of the solvent can be H_2O or another organic medium, depending on the selected precursor. Ceramics synthesized by sol-gel, for example, are mainly oxides; water is one of the best candidates to dissolve the precursor when it comes to sales but not for alkoxide precursors. Another

important factor is that the electronic properties of water are important in the process of transforming the precursor to the sol. Precursors other than alkoxides or metal salts have also been investigated, as is the case of organometallic compounds in which a metal M is directly bonded to a carbon atom.

2.1.2 The sol

A colloid is a suspension in which the dispersed phase is so small (~1-1000 nm) that gravitational forces are negligible and interactions are dominated for short-range forces, such as Van der Waals attraction and surface charges. The inertia of the dispersed phase is small enough that it exhibits Brownian motion, a random walk driven by momentum imparted by collision with molecules of the suspending medium. A sol is a colloidal suspension of solid particles within a liquid. An aerosol is a colloidal suspension of particles in a gas and emulsion is a suspension of liquid droplets in another liquid. All of these types of colloids can be used to generate polymers or particles from which ceramic materials can be made. A ceramic is usually defined by saying what it is not nonmetallic or inorganic; some would also say it is not a chalcogenide. In the sol-gel process, the precursors (starting compounds) for the preparation of a colloid consist of a metal or metalloid element surrounded by various ligands. In the sol-gel method it is used, as precursor metallic salts or alkoxides compounds [37].

In the present work, for the preparation of $BaTiO_3$:Er^{3+}-Yb^{3+} sols, metallic alkoxides were used. An alcoxy is a ligand formed by removing a proton from the hydroxyl on an alcohol, as in methoxy ($\bullet OCH_3$) or ethoxy ($\bullet OC_2H_3$). A list of the most commonly used alcoxy ligands is presented in Table 2-2. Organometallic compounds are defined as having direct metal-carbon bonds, not metal-oxygen-carbon linkages as in metal alkoxides, thus, alkoxides are not organometallic compounds, although that usage turns up frequently in the literature.

Table 2-2. *Commonly ligands used in the sol-gel process.*

Alkoxy		**Alkyl**	
Metoxi	$\cdot OCH_3$	**methyl**	$\cdot CH_3$
Etoxi	$\cdot OCH_2CH_3$	**ethyl**	$\cdot CH_2CH_3$
n-propoxy	$\cdot O(CH_2)_2CH_3$	**n-propyl**	$\cdot (CH_2)_2CH_3$
Iso-propoy	$H_3C(\cdot O)CHCH_3$	**iso-propyl**	$H_3C(\cdot C)HCH_3$
n-butoxy	$\cdot O(CH_2)_3CH_3$	**n-butyl**	$\cdot CH2(CH_2)_2CH_3$
Sec-butoxy	$H_3C(\cdot O)CHCH_2CH_3$	**sec-butyl**	$H_3C(\cdot C)HCH_2CH_3$
Iso-butoxy	$\cdot OCH_2CH(CH_3)_2$	**iso-butyl**	$\cdot CH_2CH(CH_3)_2$
Ter-butoxy	$\cdot OC(CH_3)_3$	**tert-butyl**	$\cdot C(CH_3)_3$

The chemical structure of the precursors employed in this work, 2-4, barium pentanedionate and titanium isopropoxide are presented in Figure 2-1. In this case, an appropriate solvent for iso-propoxi type is isopropyl alcohol.

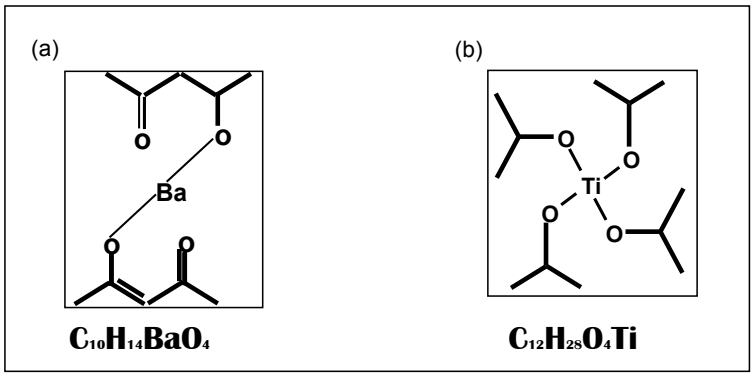

Figure 2-1. *Chemical structure of precursors used for the elaboration of $BaTiO_3$, 2-4, barium pentanedionate (a) and (b) titanium tetraisopropoxide.*

During the sol formation stage several reactions are carried out with the starting materials and solvent as is following presented:

$$Ba(C_5H_7O_2)_2 + C_3H_7O \rightarrow Ba(OC_3H_7)_2 + (C_5H_7O_2)OH \quad (1)$$

$$Ti(H_7C_3O)_4 + C_3H_7OH \rightarrow Ti(OC_3H_7)_4 + (H_7C_3O)OH \quad (2)$$

a) Hydrolysis

Metal alkoxides are popular precursors because they react readily with water. The reaction is called hydrolysis, because a hydroxyl ion becomes attached to the metal atom, as in the following reactions:

$$Ba(C_5H_7O_2)_2 + H_2O \rightarrow HO-Ba(C_5H_7O_2) + (C_5H_7O_2)OH \quad (3)$$

$$Ti(H_7C_3O)_4 + H_2O \rightarrow HO-Ti(H_7C_3O)_3 + (H_7C_3O)OH \quad (4)$$

Depending on the amount of water and catalyst presents, hydrolysis may go to completion (so that all of the OR groups are replaced by OH), or stop while the metal is only partially hydrolyzed $(H_3COCHCH_3)_{4-1}(OH)_n$, and later hydrolyze adding water to the initial synthesis [38].

$$Ti(H_7C_3O)_4 + 4\ H_2O \rightarrow Ti(OH)_4 + 4\ (H_7C_3O)OH \quad (5)$$

b) Condensation

The colloidal particles are formed for condensation reaction in the dissolved species. Condensation can proceed by either of throw nucleophilic mechanism depending on the coordination of the metal. When the preferred coordination is satisfied, condensation occurs by nucleophilic substitution. When the preferred coordination is not satisfied, condensation can occur by nucleophilic addition [23]. In the case of barium titanate, two molecules hydrolyzed partially can be cross linked and generate a condensation reaction as following:

$$HO\text{-}Ti(H_7C_3O)_3 + HO\text{-}Ti(H_7C_3O)_3 \rightarrow (H_7C_3O)_3Ti\text{-}O\text{-}Ti(H_7C_3O)_3 + H_2O \quad (6)$$

or

$$(O_3C_5H_7)_3Ba\text{-}(O_3C_4H_7) + HO\text{-}Ba(C_5H_7O_2) \rightarrow (C_5H_7O_3)_3Ba\text{-}O\text{-}Ba(C_5H_7O_3)_3 + (C_5H_7O_3)OH \quad (7)$$

In this stage a small quantity of water or alcohol are liberated. This kind of reaction can follow up to create long chains of Ba and Ti by means of polymerization process (gel formation).

2.1.3 The gel

A gel is a porous 3-dimensionally interconnected solid network that expands in a stable fashion throughout a liquid medium and is only limited by the size of the container (Figure 2-2). The continuity of the solid structure gives elasticity to the gel. The gel structuring is showed in Figure 2-3 [39].

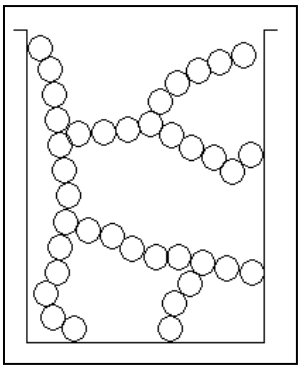

Figure 2-2. *Gel scheme, solid network imbibed in a liquid phase (solvent).*

The nature of gels depends on the coexistence between the solid network and the liquid medium. The liquid is presented between the mesh of solid network that composes the gel, it does not flow out spontaneously and is in thermodynamic equilibrium with the solid network. If the solid network is made of colloidal sol particles the gel is said to be colloidal. If the solid network is made of sub-colloidal chemical units the gel is polymeric. There is a great diversity of organic and inorganic gels, one of them is presented in Figure 2-3 [23].

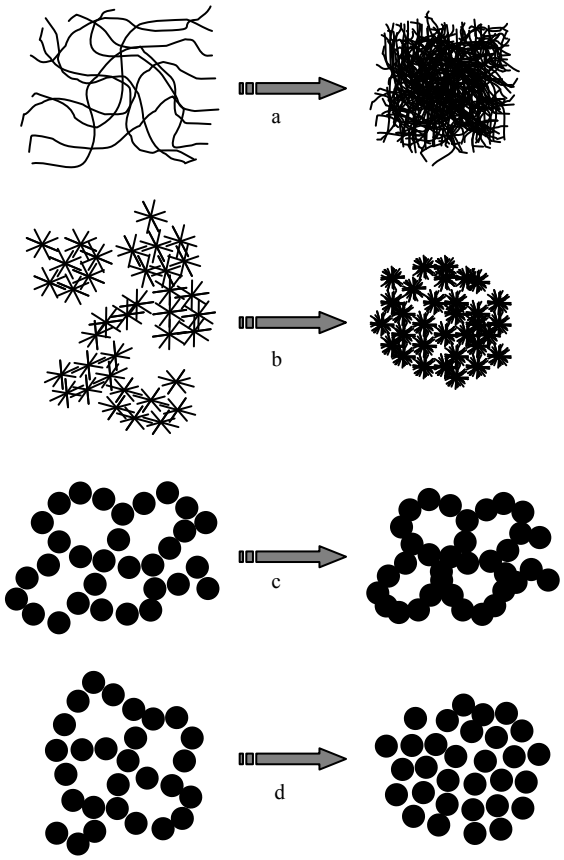

Figure 2-3. *Gel structuration. In a gel, the bonds can be reversible as in the particulate system (c, d) or permanents as in polymeric systems (a, b).*

2.1.4 Thermal treatments

a) Xerogel

If the liquid is removed, a little brittle solid obtained is either called a xerogel or an aerogel depending on the drying method. The solvent are removed at moderate temperatures (<100 °C) producing a high hydrolized metallic oxide with organic residues. In this step, some chemical compounds can be added to the solution in order to increase the yield of the reaction, as a catalyzer, a stabilizing additive or a chelating agents with the aim of to control of rate of dried.

$BaTiO_3$ has been studied in the gel form, for example, when it is prepared from acetate and titanium alkoxides and dried at 100 °C it produces second compounds like carbonates. The carbonates are difficult to remove during heat treatment [40]. In this specific case, the alkoxide precursor, titanium isopropoxide is similar to utilized in the present work. Figure 2-4 is shows a transmission electron microscopy (TEM) of $BaTiO_3$ gel obtained by sol-gel method.

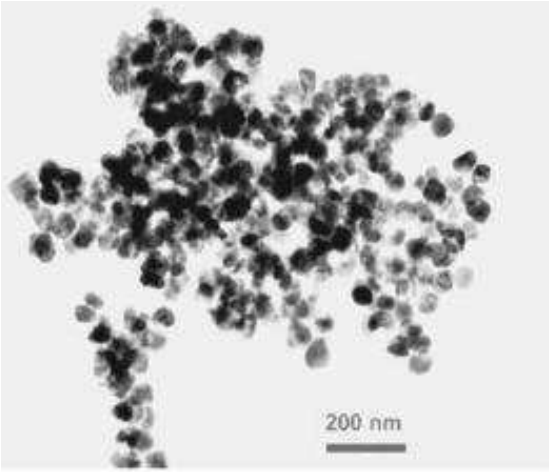

Figure 2-4. *$BaTiO_3$ gel image from acetate y TPOT precursors dried at 100 °C (gel analysis).*

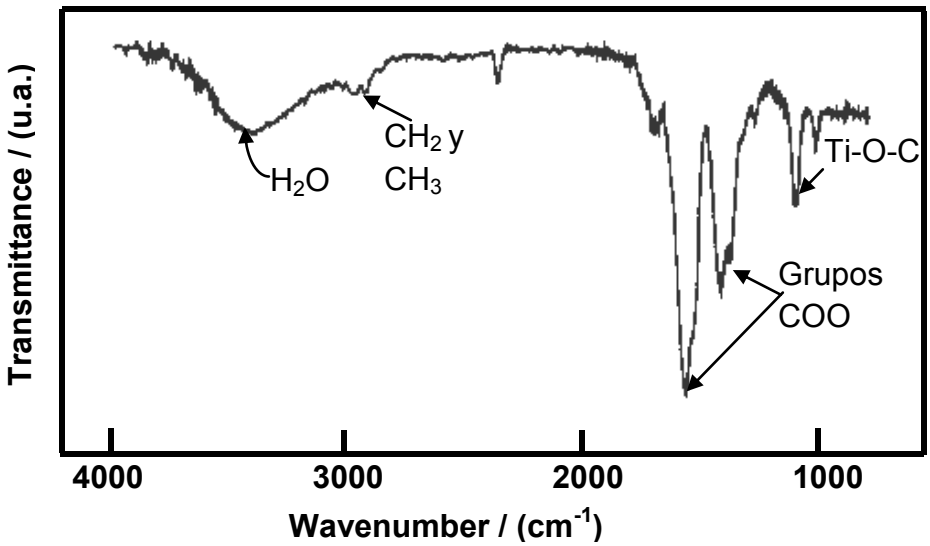

Figure 2-5. *IR spectra of $BaTiO_3$ gel dried at 100 °C elaborated by sol-gel method using acetic acid during the synthesis.*

O. Harizanov et. al. [41] studied the $BaTiO_3$ gel using acetic acid as chelating agent, in the Figure 2-5 is presented the IR spectrum of $BaTiO_3$ dried at 100 °C. In this figure is observed absorption bands situated at 3400 cm^{-1} associated to the existence of water, the bands located at 2930-2960 cm^{-1} are attributed to aliphatic compounds as CH_2 y CH_3 and the bands at 1580 y 1420 cm^{-1} revealed the presence of symmetric and asymmetric COO groups, the amplitude of this bands are due to the contribution of the chelating agents (acetic acid) and the formation of Ti and Ba complex. The absorption bands at 1120 cm^{-1} is characteristic of Ti-O-C groups.

2.2 Hydrothermal method

The term hydrothermal is purely of geological origin. It was first used by the British geologist, Sir Roderick Murchison (1792-1871), to describe the action of water at elevated temperature and pressure in bringing about changes in the earth's crust, and leading the formation of various rocks and minerals. The largest-known single crystal formed in nature and some of the largest quantities of single crystals created in one experimental run are both of hydrothermal origin [42].

Hydrothermal processing can be defined as any homogeneous (bulk material) reaction in the presence of aqueous solvents or mineralizers under high pressure and temperature conditions to dissolve and recrystallize (recover) materials that are relatively insoluble under ordinary conditions. Byrappa and Yoshimura (2001) define hydrothermal as any homogeneous or heterogeneous chemical reaction in the presence of a solvent (whether aqueous or non-aqueous) above the room temperature and at pressure greater than 1 atm in a closed system [42]. However, there is still some confusion with regard to the very usage of the term hydrothermal. For example, chemists prefer to use a term, solvothermal, meaning any chemical reaction in the presence of a non-aqueous solvent or solvent in supercritical or near supercritical conditions. Similarly there are several other terms like glycothermal, alcothermal, ammonothermal, carbonothermal, lyothermal, and so on (for

different solvents used). Many researchers call this green processing or green chemistry [43].

The hydrothermal technique has a lot of other advantages like it accelerates interactions between solid and fluid species, single phase and homogeneous materials can be achieved, reaction kinetics can be enhanced, the hydrothermal fluids offer higher diffusivity, lower viscosity, facilitate mass transport and higher dissolving power. Most important is that the chemical environment can be suitably tailored. Although the process involves a slightly a longer reaction time compared to the vapor deposition, or milling processes, it provides highly crystalline particles with a better control over its size and shape. A great variety of materials like native elements, metal oxides, hydroxides, silicates, carbonates, phosphates, sulphides, tellurides, nitrides, selenides, etc., both as particles and nanostructures like nanotubes, nanowires, nanorods, and so on, have been obtained using the hydrothermal method. The method is also popular for the synthesis of a variety of forms of carbon like sp2, sp3 and intermediate types.

2.2.1 Equipment

In recent years, there is not much of focus on the designing of new instrumentation for conventional hydrothermal processing of materials.
We can divide this aspect into two areas. The first one deals with the geological and geophysical studies, where extreme pressure reactors, belt apparatus, piston cylinder and anvil type apparatus are popularly used. The second area deals with the materials processing in industries and academia, wherein the pressure and temperature conditions of processing are becoming more and more environmentally benign through operations under milder conditions.

Many researchers and industrialists/commercial manufacturers of materials use large volume simple design reactors, flowcells, the Tuttle type batch reactors for higher temperature and pressure operations for academic interest, general purpose autoclaves. In

Table 2-5 different types of autoclaves employed in the hydrothermal synthesis are listed. Figure 2-6 shows a cold-cone seal, Tuttle Roy type (conventional autoclaves).

Table 2-3. *List of autoclaves employed in the hydrothermal synthesis.*

Type	Characteristic data
Pyrex tube 5 mm	6 bars at 250 °C
Quartz tube 5 mm	6 bars at 300 °C
Flat plate seal, Morey type	400 bars at 400 °C
Welded Walker-Buehler closure 2600 bar at 350 °C	2 Kbars at 480 °C
Delta ring, unsupported area	2.3 Kbars at 400 °C
Full Bridgman, unsupported area	3.7 Kbars at 500 °C
Cold-cone seal, Tuttle Roy type (used in the present work)	3.7 Kbars at 750 °C
Piston cylinder	40 Kbars at 1000 °C
Opposed anvil	200 Kbars at >1500 °C
Opposed diamond anvil	Up to 500 Kbares a >2000 °C

Figure 2-6. *Image of a cold-cone seal, Tuttle Roy type (conventional autoclaves).*

2.2.2 Synthesis conditions

Nowadays, the hydrothermal route is a soft chemistry method highly efficient in the synthesis of advanced materials, as nanomaterials with shape and size controlled. As evident from Table 2-4, the hydrothermal technique is ideal for the processing of very fine powders having high purity, controlled stoichiometry, high quality, narrow particle size distribution, controlled morphology, uniformity, less defects, dense particles, high crystallinity, excellent reproducibility, controlling of microstructure, high reactivity/ sinterability, and so on. Figure 2-7 shows the major differences in the products obtained by ball milling or sintering or firing and hydrothermal methods [44].

The important step in the processing of fine particles of advanced materials is the use of surfactants and chelates to control the nucleation of a desired phase, such that the phase homogeneity, size, shape and dispersibility could be achieved during the crystallization of these fine particles. This is in fact the beginning of the study of precursor preparation for different systems, the surface interactions with the capping agents or surfactants, and polymerized complexes.

The surfaces of the particles could be altered to hydrophobic or hydrophilic depending upon the applications [30, 68]. Today this approach is playing a key role in nanotechnology to prepare highly dispersed, oriented and self-assembled particles.

Table 2-4. *Advance in oxide powders process comparison* [45].

Parameter	Solid state reaction	Co-precipitation	Sol-gel	Polymerizable complex	hydrothermal
Cost	Low to moderate	Moderate	High	High	Moderate
State of development	Commercial	Demonstration /commercial	research	research	research / demonstration
Compositional control	Poor	Good	Excellent	Excellent	Good/excellent
Morphology control	Poor	Moderate	Moderate	Moderate	Good

Powder reactivity	Poor	Good	Good	Good	Good
Purity (%)	<99.5	>99.5	>99.9	>99.9	>99.9
Calcination step	Yes (multiple)	Yes	Yes	Yes	Yes
Grinding steps	Yes (multiple)	Yes	Yes	Yes	Yes

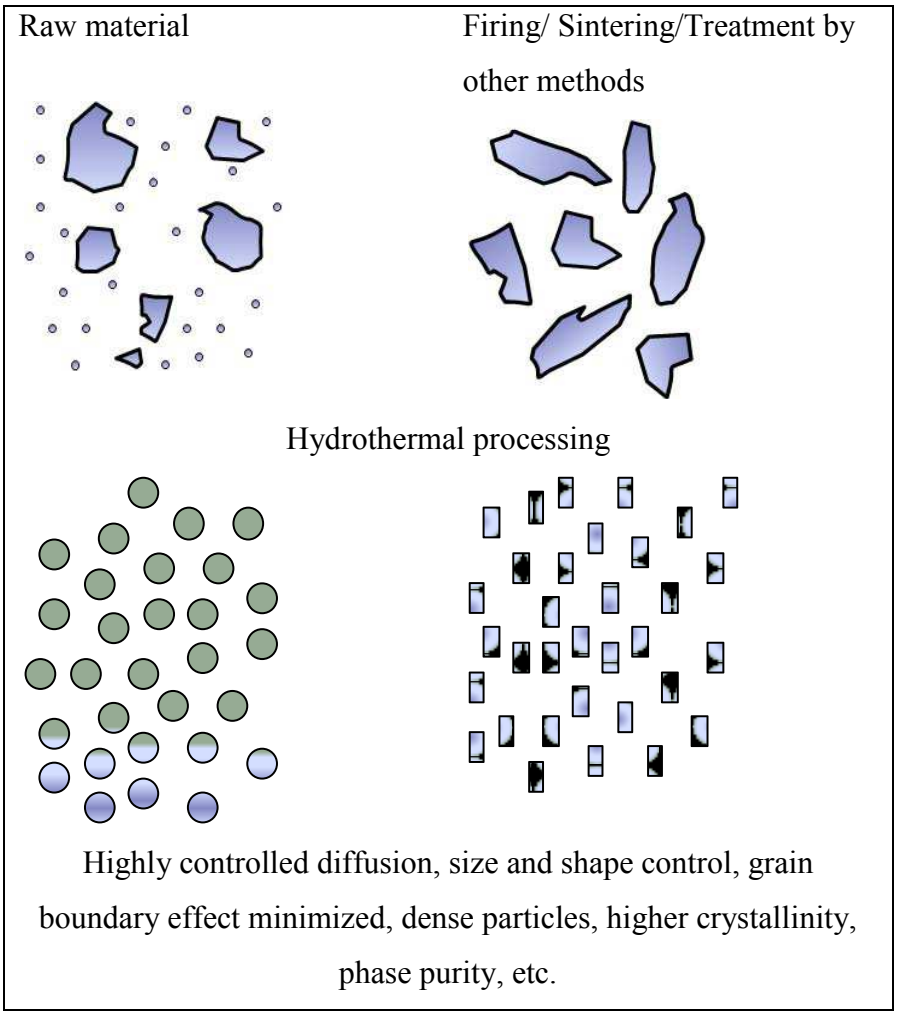

Figure 2-7. *Difference in particle processing by hydrothermal and conventional ball milling techniques.*

2.2.3 Crystal growing

The focus of hydrothermal technology in the earlier days was exclusively on the growth of bulk single crystals. Today much of the commercial production of bulk single crystals using hydrothermal technology is still restricted to quartz, colored quartz, emerald, corundum, ruby, etc. Hence, since 1970s the use of hydrothermal technology for the growth of other large single crystals declined significantly.

In recent years there is again a growing interest in the use of hydrothermal technology for the single crystal growth of ZnO, GaPO4, GaN, and Langesite. We briefly discuss here the growth of perovskites ceramic materials obtained by this method.

a) Hydrothermal preparation of perovskita type: $BaTiO_3$

The general formula for perovskite can be written as ABO_3 where A=Ba, Ca, Sr, Pb. Aksay et. al. [46] in 1996 have prepared nanometer sized $BaTiO_3$ particles under hydrothermal conditions of $Ba(OH)_2$. For the preparation of fine particles of this perovskite type mixed oxide, knowledge of stability diagrams under hydrothermal conditions is very important. The stability diagram shows the regions of reagents concentration and pH at which various species predominate in the system (Figure 2-8). Ecker Jr et. al. [47] in 1996 have proposed in situ reaction mechanism and dissolution-precipitation reaction mechanism, Figure 2-9 and 2-10.

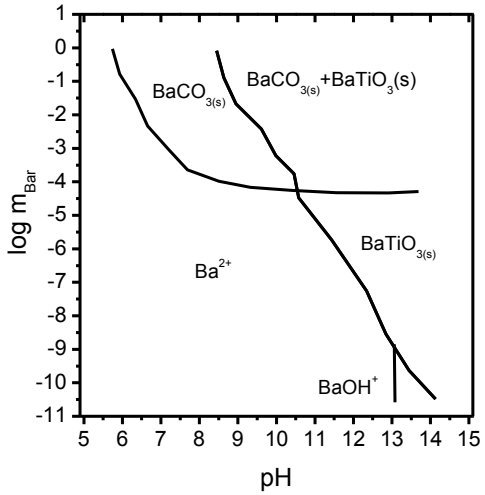

Figure 2-8. *Stability diagram for barium titanate system.*

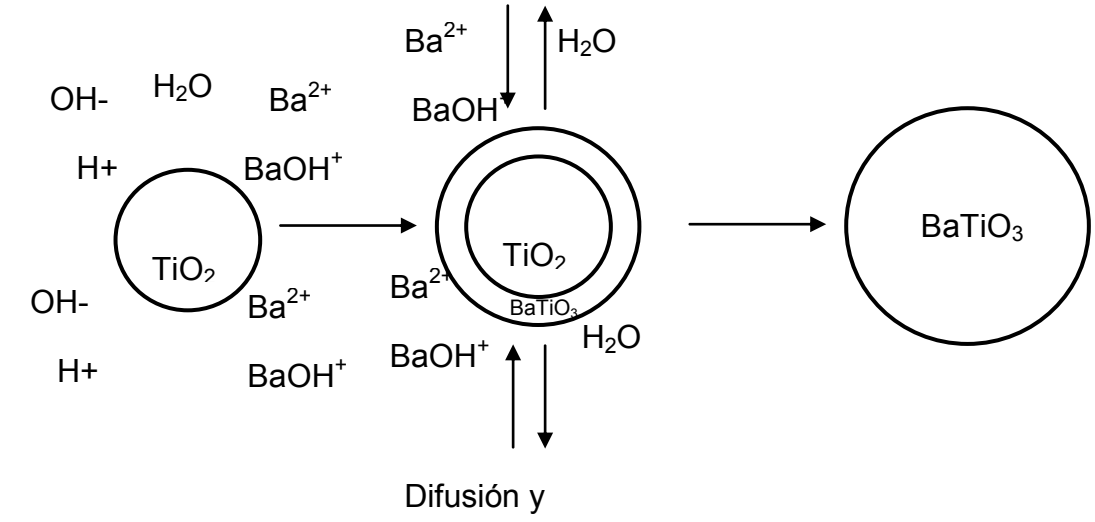

Figure 2-9. *In situ reaction mechanism.*

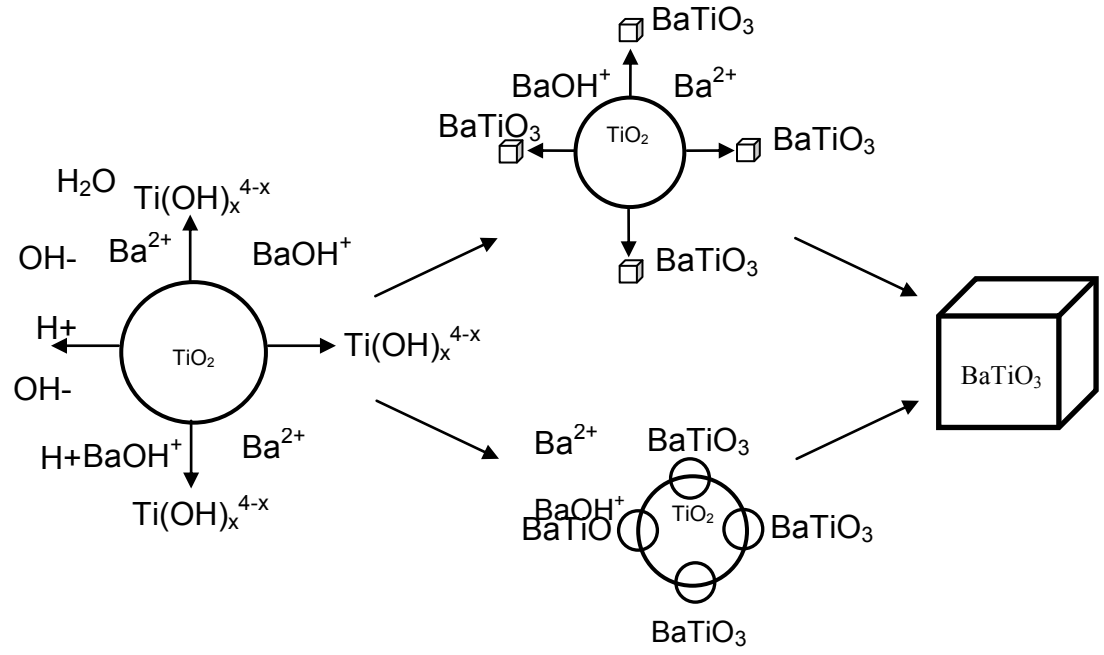

Figure 2-10. *Dissolution-precipitation reaction mechanism.*

As evident from these figures, the in situ transformation model assumes that TiO_2 reacts initially with dissolved barium. This produce a continuous layer of $BaTiO_3$ through which additional barium must be diffuse in order to continue reaction until TiO_2 supply is exhausted.

The product layer may be either a dense or a porous layer of monocrystalline or polycrystalline nature. The dissolution-precipitation method involved multiple steps. For an anhydrous TiO_2 precursor, Ti-O bonds must be broken via hydrolytic attack, to form hydroxyl-titanium complexes ($Ti(OH)_x^{4-X}$) capable of dissolution and reaction with barium ions or complexes (Ba^{2+} o $BaOH^+$) in solution to precipitate $BaTiO_3$.

From the above review, we can conclude that hydrothermal route is a hard tool in the elaborations of materials since the used conditions are "soft" in comparison with conventional methods which use high temperature, therefore, this method produce fine and ultrafine particles with controlled properties. In general, morphology, grain size, and quality, can be controlled through several parameters, like temperature, pH of the solution at the interface, impurities (dopants) and time of the experiment.

The combination of hydrothermal technology and nanotechnology could solve most of the problems associated with advanced materials processing in 21st century. Similarly the combination of polymerizing sol–gel and hydrothermal has a great potential to process materials under environmentally benign conditions. The gel chemistry of metal alkoxides would provide new avenues for precursor preparation for hydrothermal processing of advanced materials. Thus, an interdisciplinary approach will be the most effective solution for the future materials processing strategies, which would be not only cost effective but also environmentally benign.

Al these advantages present a great perspective for hydrothermal technology in the 21^{st} century for advanced materials processing.

2.3 Solid state reaction

The synthesis of solid materials, particularly when they are polycrystalline materials in powder form, usually takes place through solid-state precursors. This synthetic route involves the transformation of the starting reagents in another desired final phase, which usually requires high temperatures and pressures. Under these conditions the atoms of the reactive species can diffuse through solid materials to react more effectively. The high temperatures and pressures used decrease the response time of these processes and help to occur full crystallization, ensuring the absence of impurities in the final compound. The solid state reaction process can be divided into two stages: the nucleation of reaction product and subsequent growth [48,49]. The nucleation process is usually difficult because the reagents and the products often have very different structures and therefore this step involves a structural reorganization of the crystal lattice of the reagents. The energy cost of this structural rearrangement is very high and hence the need to use higher reaction temperatures. The nucleation process is simplified when any of the reagents has a crystalline structure similar to the reaction product, i.e. bond distances and similar atomic structures. Once formed the core, output growth is limited by diffusion of ions from the reactants through the product layer already formed, until the end of the reaction.

An inconvenient of this method of synthesis is the possible formation of secondary phases of the final product by reaction with any of the reagents that have not reacted completely. To avoid this problem successive heat treatments are performed with processing times increasing and grindings between each of these treatments, in order to achieve a complete homogenization of the reaction mixture. Table 2-5 details the main features of the reagents used in the process of synthesis by solid state reaction.

Table 2-5. *Raw materials used in the $BaTiO_3:Eu^{3+}$ synthesis by solid state reaction.*

Starting materials	Purity
$BaCO_3$	≥99 %
TiO_2	99.9 %
$EuCl_3$	99.99%

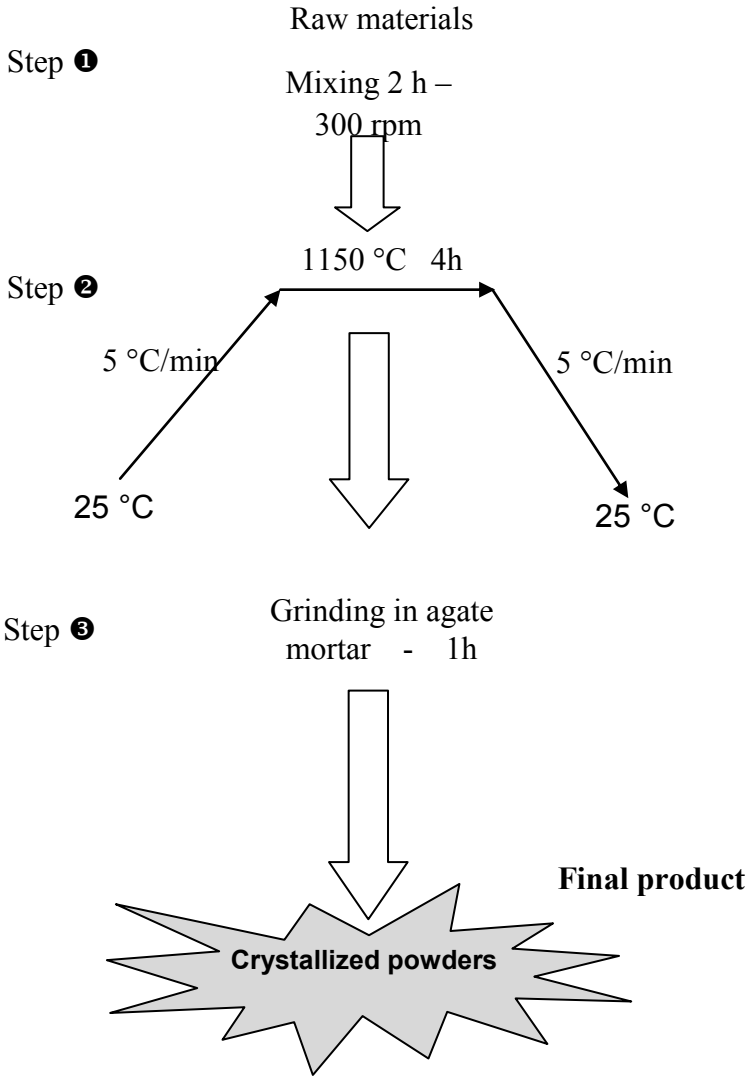

Figure 2-11. *General scheme for the $BaTiO_3$ synthesis by solid state reaction.*

Chapter 3. Luminescence

The optical behavior of a solid material is a function of their interaction with electromagnetic radiation. These interactions include, among other the absorption and emission phenomena. To understand the optical behavior of rare earths ions doped barium titanate, this chapter presents the theoretical aspects of the emission and absorption spectroscopy, so that in the chapter of results will be presented to a large extent. The spectroscopic properties of rare earths ions employed in this work are also described briefly in this chapter.

3.1 Introduction

Ultraviolet (UV) and visible radiation comprise only a small part of the electromagnetic spectrum, which includes such other forms of radiation as radio, infrared (IR), cosmic, and X rays (see Figure 3-1) [50].

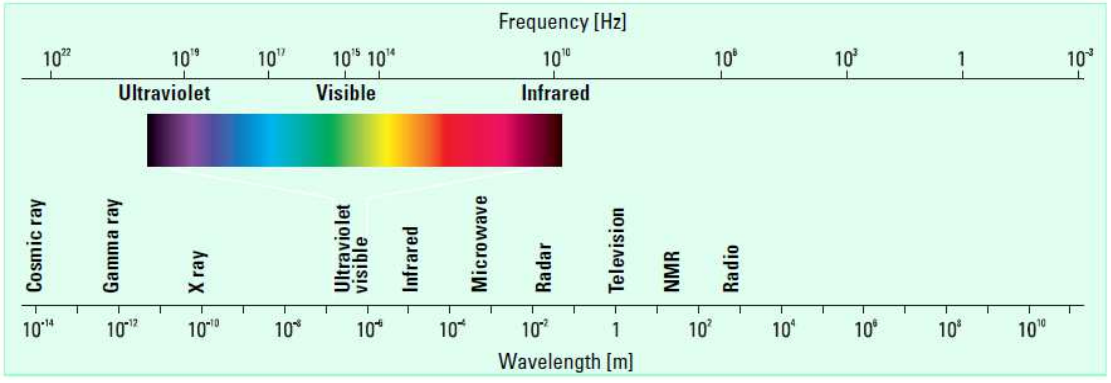

Figure 3-1. *The electromagnetic spectrum.*

The energy associated with electromagnetic radiation is defined by the following equation: $E=h\nu$, where E is energy (in joules), h is Planck's constant ($6.62x10^{-34}$Js), and ν is the frequency (s).

a) Wavelength and frequency

Electromagnetic radiation can be considered a combination of alternating electric and magnetic fields that travel through space with a wave motion. Because radiation acts as a wave, it can be classified in terms of either wavelength or frequency, which are related by the following equation: $\nu = c/\lambda$ where ν is frequency (in seconds), c is the speed of light (3×10^8 ms^{-1}), and λ is wavelength (in meters). In UV-visible spectroscopy, wavelength usually is expressed in nanometers (1 nm = 10^{-9} m). It follows from the above equations that radiation with shorter wavelength has higher energy. In UV-visible spectroscopy, the low-wavelength UV light has the highest energy. In some cases, this energy is enough to provoke undesirable photochemical reactions after measuring sample spectra (remember, it is the UV component of light that causes sunburn). When radiation interacts with matter, a number of processes can occur, including reflection, scattering, absorbance, fluorescence/phosphorescence (absorption and reemission), and photochemical reaction (absorbance and bond breaking). From here, the focus will be in the process of luminescence.

3.2 Luminescence

A luminescent material, also called phosphorus, is a solid which converts energy in various types of radiation with certain characteristics, in the case of luminescent materials is usually in the visible range, but can also be in other regions of the spectrum, such as infrared or ultraviolet [51]. The luminescence may be caused by different types of energy, a general outline of the types of luminescence are shown in Figure 3-2. The photoluminescence results of the absorption of photons causing re-radiation of photons, the cathodoluminescence of a beam of electrons, the electroluminescence is obtained from of a response to an electric current passed through it, triboluminescence is generated when

bonds in a material are broken when that material is scratched, crushed, or rubbed; the X ray luminescence is produce by X rays and the chemiluminescence results of a chemical reaction. Among the important, fluorescence and phosphorescence, are briefly described below.

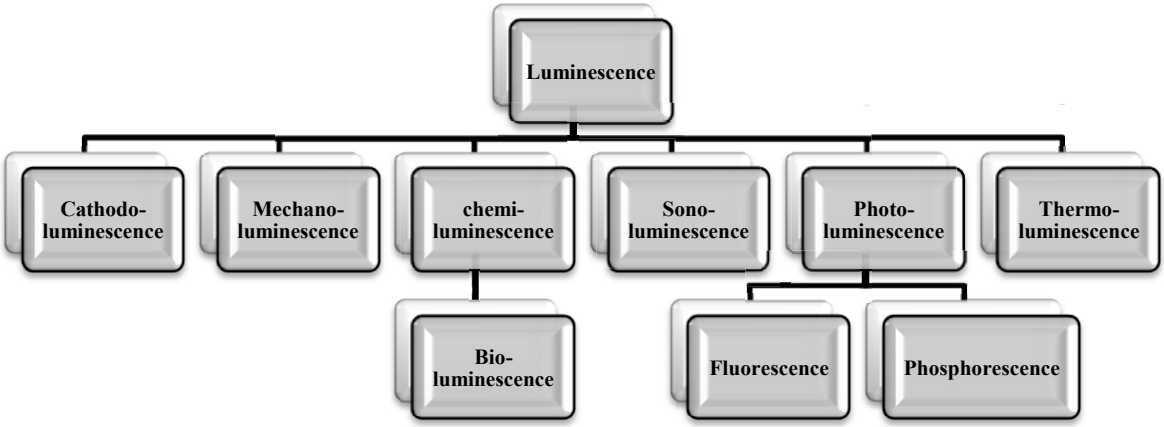

Figure 3-2. *Different types of energy used for excitation of a luminescent material.*

3.2.1 Fluorescence and phosphorescence

Luminescence is most conveniently defined as the radiation emitted by a molecule, or an atom, after it had absorbed energy to go to an excited state. The main types of luminescence consist of fluorescence and phosphorescence. Once a molecule arrives at the lowest vibrational level of an excited singlet state, it can do a number of things, one of which is to return to the ground state by photon emission. This process is called fluorescence. The lifetime of an excited singlet state is approximately 10^{-9} to 10^{-7} s and therefore the decay time of fluorescence is of the same order of magnitude. If fluorescence is unperturbed by competing processes, the lifetime of fluorescence is the intrinsic lifetime of the excited singlet state. The quantum efficiency of fluorescence is defined as the fraction of molecules that will fluoresce. The change in photon energy causes a shift of the fluorescence spectrum to longer wavelength, relative to the absorption spectrum; this is referred to as the Stokes Shift.

If a molecule is placed in a rigid medium where collisional processes are minimized, a *radiative transition* between the lowest triplet state and the ground state is observed. This emission is called *phosphorescence*. As phosphorescence originates from the lowest triplet state, it will have a decay time approximately equal to the lifetime of the triplet state. Therefore phosphorescence is often characterized by an afterglow which is not observed for fluorescence.

Figure 3-3 shows the radiation absorbed by the activator ion, reaching the excited state. The excited state returns to basal state through the emission radiation. The main characteristics for the measurement of these systems are the energy distribution spectra (emission spectra) absorption excitation and radiative and non radiative frequencies when the electron returns to the ground stated. Luminescent materials emit radiation only when the excitation energy is absorbed.

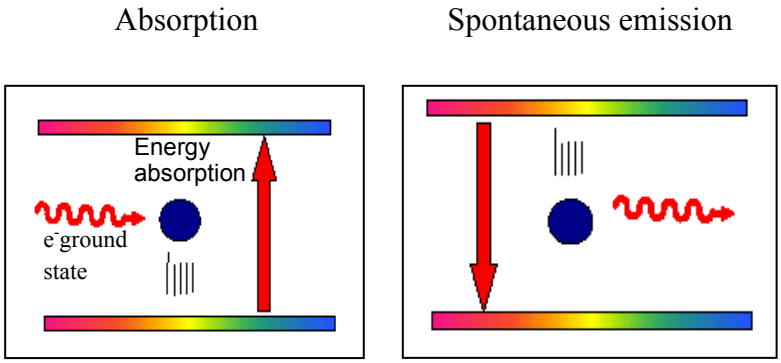

Figure 3-3. *Energy diagram for a photoluminescence system.*

3.3 Energy level diagrams of rare earth ions

Rare earth ions ($4f^n$, where n is the atomic number) are characterized because its 4f orbital is incomplete. The 4f orbital allows the ion to enter and be protected from the surroundings by $5s^2$ and $5p^6$ orbitals. The influence of host matrix on the optical transitions in the $4f^n$ configuration is small (but essential). Figure 3-4 presents a substantial part of the energy levels arising from the $4f^n$ configuration as a function of n for trivalent ions [28,52].

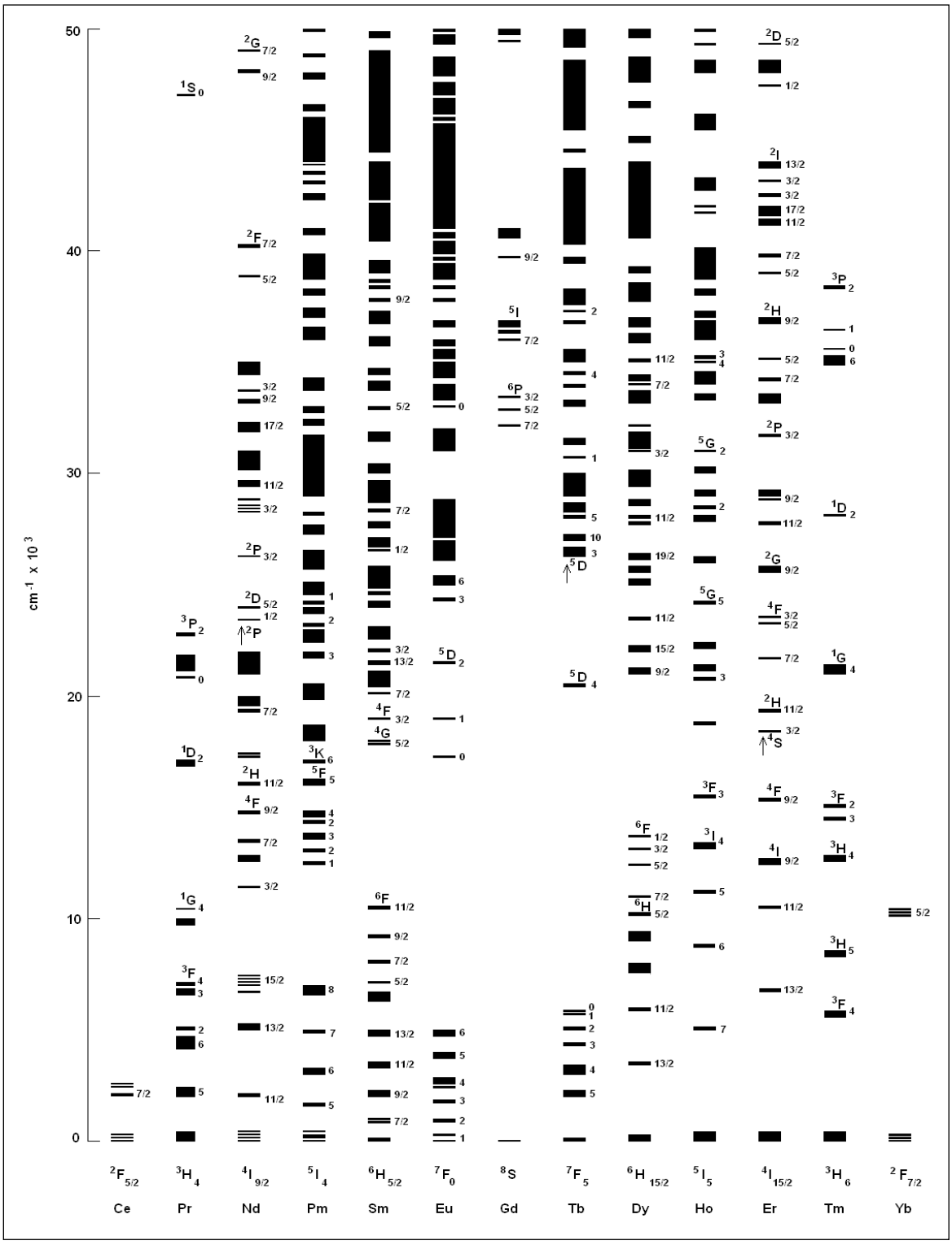

Figure 3-4. *Complete $4f^n$ energy–level diagram for the trivalent lanthanides*.

The allowed optical transitions of rare earth ions are configurational and they consist of two different types:

- Charge transfer transitions ($4f^n \rightarrow 4f^{n-1}L^{-1}$, where L is a ligand) and
- Transitions $4f^n \rightarrow 4f^{n-1}5d$

Both transitions are allowed and appear in the absorption spectrum as a broadband connection.

Divalent rare earth ions (Sm^{2+}, Eu^{2+}, Yb^{2+}) show $4f \rightarrow 5d$ transitions, Sm^{2+} in the visible range, while the Eu^{2+} and Yb^{2+} appear throughout the ultraviolet region. Less electronegative ions such as Nd^{3+}, Dy^{3+}, Ho^{3+}, Er^{3+} and Tm^{3+} show charge transfer transitions in the region of 30 000 cm^{-1} approximately.

Trivalent ions with tendency to become tetravalent (Ce^{3+}, Pr^{3+}, Tb^{3+}) reveal the absorption bands $4f \rightarrow 5d$ in the ultraviolet region.

3.4 Emission

Figure 3-5 shows a configurational coordinated diagram, considering that there is a shift between the excited state and ground state. The absorption occurs in a broad optical band. Luminescent centers (doping ions) firstly return to the lowest vibrational level of the excited state providing excess energy to the surroundings.

Another way to describe this process is that the core adjusts its positions to the new situation (excited state) and the fact that interatomic distances are equal to the equilibrium distances, which belong to the excited state. This process is called relaxation, during which emission usually does not occur. This can be seen with the relaxation rates involved: areas exhibiting fast emission with a velocity of 10^8 ms^{-1}. Finally, the lowest vibrational levels of excited states, systems can return to its ground state emitting radiation spontaneously.

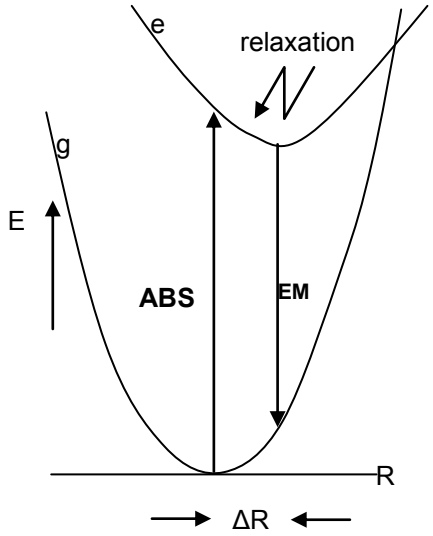

Figure 3-5. *Configurational coordinated diagram. The configurational coordinated diagram provides a useful route for qualitative representation of the process of luminescence.*

For emission, the luminescent centers reach high vibration levels of the excited state. Relaxation occurs again, but now for the low vibrational levels of the ground state. The emission occurs at a lower energy than the absorption due to relaxation processes.

3.4.1 Up-conversion process

The up-conversion principle is presented in Figure 3-6, this figure shows the energy levels of the structure in an ion at ground state A, and excited to B and C level. The energy difference between level C and B and the levels A and B are equal. The excitation occurs with a radiation energy equivalent to the energy difference between levels, so the ion is excited from A to B. If the lifetime of the B level is not to small, radiation excite this ion from B to C. Finally, the emission from C to A occurs. It is considered that the energy difference BA and CB is 10000 cm^{-1} (corresponding to the infrared excitation) then, the emission is at 20000 cm^{-1}, i.e. in the green region.

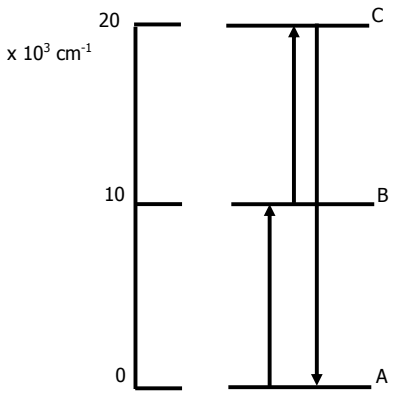

Figure 3-6. *Up-conversion principle. The infrared excitation (10000 cm^{-1}) is converted to green emission (20000 cm^{-1}).*

Up-conversion can only occur in materials in which multiphonon relaxation processes are not predominant, thus allowing more than one metastable excited state. In rare-earth compounds, the 4f or 5f electrons are efficiently shielded and thus not strongly involved in the metal-to-ligand bonding. As a consequence, electron-phonon coupling to f-f transitions is reduced, and multiphonon relaxation processes are less competitive. The phenomenon of up-conversion is therefore most common and best studied in materials containing lanthanide ions. But there are also transition-metal systems and rare-earth/transition-metal combinations which show this phenomenon.

A large number of possible up-conversion processes has been discovered. According to Auzel, its energy schemes are presented in Figure 3-7 [16]:

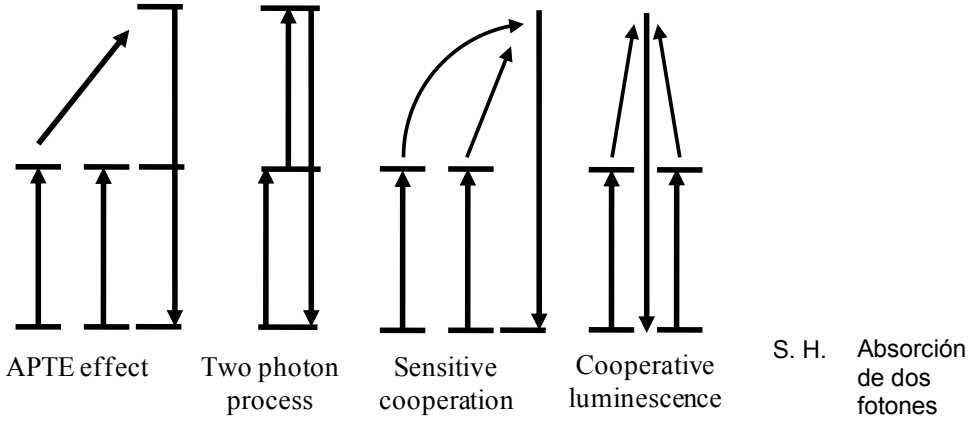

Figure 3-7. *Up-conversion process according to Auzel* [16].

The processes are:

- Up-conversion by energy transfer also called APTE effect (energy transfer by the addition of photons). Here the ions A subsequently transfer its excitation energy to another ion B which can now deliver a higher level.
- Up-conversion by two photon process which needs only the ion B. (Figure 3-6).
- Up-conversion by sensitive cooperation two ions simultaneously transfer their excitation energy to ion C which does not have an energy level in the position of the excited level A. The emission occurs from the excited level C.
- Up-conversion by cooperative luminescence: two ions combine their excitation energy to a quantum which is emitted (although there is no real emission of the level).

Recently has increased the study of up-conversion processes in rare earth ions doped materials with for applications in laser devices [53,54], three-dimensional display [55], sensors [56] and biological fluorescent labels [57-59]. The energy radiation of the up-conversion process can be by intraionic successive absorptions, cooperative energy transfer or electron avalanche process [60,61]. The investigation of these mechanisms provides a better understanding of the physics of the energy transfer processes and fluorescent converters. It has now been studied, radiation green and red up-conversion induced by a laser diode excitation at 980 nm in Y_2O_3: Er^{3+}-Yb^{3+} nanocrystals and ZrO_2:Er^{3+}-Yb^{3+} [62,63]. It is known that the Er^{3+} ion absorbs a photon of the laser and move from one ground state $^4I_{15/2}$ to state $^4I_{11/2}$, this process is called the ground state absorption (GSA). So, excited state absorption (ESA) may come to populate the state $^4F_{7/2}$. Subsequently, the Er^{3+} ion in the state $^4F_{7/2}$ can relax quickly to the $^2H_{11/2}$/$^4S_{3/2}$ states through a multiphononic process, from which the green bottom emission takes place. Thus, the up conversion emission green is a result of the process of two-photon excitation (GSA followed by ESA).

When the ytterbium ion is codoped, the ion provides excitation to the $^4I_{11/2}$ level of Er^{3+} through energy transfer processes due to the fact that Yb^{3+} ion have a big transversal section of absorption compared with the erbium ions [64]. The first example of material which

presented the up-conversion process was reported in 1966 by Auzel, for the couple Yb^{3+}, Er^{3+} in $CaWO_4$ [16]. Infrared radiation (970 nm) is absorbed by the ytterbium (($^2F_{7/2} \rightarrow {}^2F_{5/2}$) and transferred to Er^{3+}. During the lifetime of the level $^4I_{11/2}$ a second photon is absorbed by the Yb and the energy transferred to Er. The erbium ion now go to $^4I_{11/2}$ level to $^4F_{7/2}$ of this rapid non-radiative decay and the $^4S_{3/2}$ level which occurs green emission ($^4S_{3/2} \rightarrow {}^2I_{15/2}$). This form of green emission is obtained from the near-infrared excitation.

Similar processes have been observed in YAG ceramic matrices [65], Y_2O_3 [66] and $BaTiO_3$ [67] when it is doped with Er^{3+} ions and/or Yb^{3+}. The details of the energy transfer mechanisms in $BaTiO_3$ when it is doped with Er^{3+} ions and / or Yb^{3+} will be discussed in chapter 6.

Chapter 4. Synthesis of $BaTiO_3$ doped with rare earth ions (Eu, Er, Yb)

The reproducibility in the synthesis of ceramic powders is a problem that must be confronted in the production of new materials. This chapter describes the experimental procedures for the elaboration of rare earth ions doped barium titanate ceramic powders and films using solid state reaction and chemical routes (sol-gel and hydrothermal).

4.1 Proposed systems

Pure and doped barium titanate matrix with different rare earth ions was synthesized using three routes. Table 4-1 presents all the system synthesized**.** It is noteworthy that "key" systems to describe synthesis procedures are shadow in the table 4-1.

4.2 Synthesis of Eu^{3+} doped $BaTiO_3$

The synthesis of $BaTiO_3$ powders by hydrothermal procedure was carried out with the raw materials barium chloride anhydrous [$BaCl_2$] (99.95 %, Aldrich), europium chloride anhydrous [$EuCl_2$] (99.99 %, Aldrich), titanium (IV) butoxide, reagent grade $Ti[OC_4H_9]_4$ (97 %, Aldrich), potassium, chunk in mineral oil, [K] (98 %, Aldrich), methyl alcohol [CH_3OH](Fermont). For the solid state reaction synthesis the raw materials used were barium carbonate [$BaCO_3$] (99.5%, Aldrich) and titanium (IV) oxide [TiO_2] (99.0 %, Interchim).

Table 4-1. *Rare earth (Er, Yb, Eu, Er-Yb.*doped *$BaTiO_3$ system prepared in this work.*

$BaTiO_3$ (%mol)	Method of synthesis
Eu^{3+}	
2.5	❷, ❸
5	❷, ❸

❶ Sol-gel: powders and films

❷ Hydrothermal

❸Solid state reaction

$BaTiO_3$(%mol)		Method of synthesis
Er^{3+}	**Yb^{3+}**	
-	**0.5**	❶
-	**1**	❶
-	**2**	❶
-	**4**	❶
-	**5**	❶, ❷, ❸
-	**6**	❶
-	**10**	❶
-	**15**	❶
0.5	-	❶
1	-	❶
3	-	❶
5	-	❶, ❷, ❸
10	-	❶
15	-	❶

$BaTiO_3$ (%mol)		Method of synthesis
Er^{3+}	**Yb^{3+}**	
0.5	**1**	❶
1	**1**	❶
3	**1**	❶
1	**5**	❶
1	**10**	❶
1	**15**	❶
1	**1**	❶
1	**2**	❶
5	**1**	❶
10	**1**	❶
15	**1**	❶
5	**6**	❶

a) Solid state reaction

The $BaTiO_3$ powders were prepared following the solid-state synthesis by firing at high temperature a mixture of $BaCO_3$ and TiO_2 [68]. Two steps were involved; first ball milling for 2 h at 300 rpm and then the product was calcined at 1150 °C for 4 h as is observed in Figure 4-1.

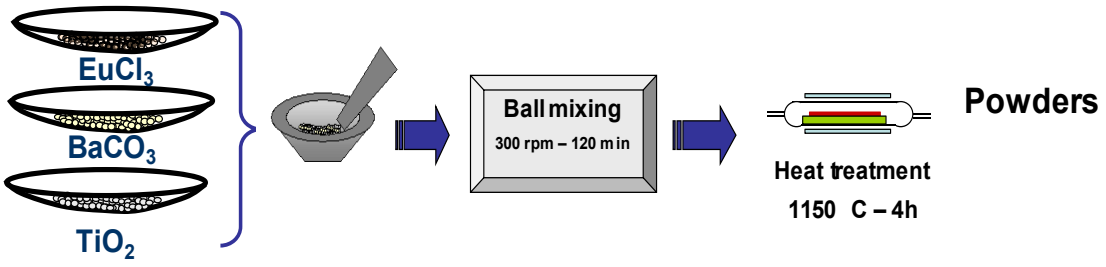

Figure 4-1. *General scheme for the $BaTiO_3:Eu^{3+}$ powders by solid state reaction.*

The processing steps were: the precursors were mixed in an agata morter for 15 min, then, ball milling for 2 h at 300 rpm in a SPEX homogenizer. Finally the $BaTiO_3:Eu^{3+}$ powders were calcined at 1150 °C for 4 h.

The main reaction involved in the formation of $BaTiO_3$ ceramic powders is follows: the first part of the formation of $BaTiO_3$ result of the decomposition of $BaCO_3$ into BaO and CO_2:

$$BaCO_3(s) \leftrightarrows BaO(s) + CO_2(g) \quad (9)$$

Decomposition of $BaCO_3$, is followed by an exothermic reaction between BaO and TiO_2 to form $BaTiO_3$:

$$BaO + TiO_2 \rightarrow BaTiO_3 \quad (10)$$

The $BaTiO_3:Eu^{3+}$ powders were obtained from before mentioned precursor using a molar ratio of Ba/Ti=1. By solid state method it was possible obtaining nanoparticles. The ceramic powders required now are in the range of nanometers. The soft chemical routes offer an important alternative of synthesis for the elaboration of powders with high purity, homogeneity and ultrafine powders, also, the doped or not nanoparticles can be obtained with optical properties, specific, luminescent properties like this study case.

b) Hydrothermal method

Barium titanate was prepared by hydrothermal method according to the procedure presented in Figure 4-2. All experiments were carried out under a free-moisture atmosphere and room temperature. To optimized the procedure of barium titanate nanoparticles, the synthesis was prepared using methyl alcohol (MeOH) as solvent. $BaCl_2$ (1.680 mMoles) y $EuCl_2$ (0.884 mMoles) were dissolved in separate flasks in an appropriate amount of MeOH under vigorous magnetic stirring for 2 h. The n, metallic potassium (2 eq.) which act as mineralizer was dissolved in MeOH, an exothermic reaction took place leading the precipitation of potassium chloride. Potassium was used rather than sodium because the size of K^+ ions (d=0.266 nm), strongly larger than of Na^+ ions (d=0.190 nm) makes its fixation in the $BaTiO_3$ lattice more difficult [13]. After 2 hours, 1.105 mMoles of titanium (IV) butoxide was introduced drop by drop and a milky solution with a pH ~14 is obtained.

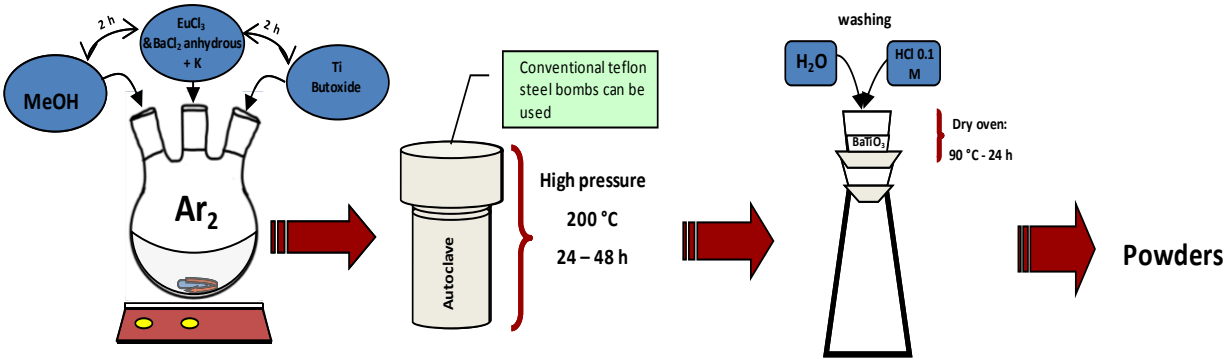

Figure 4-2. *General scheme for the elaboration of $BaTiO_3$:Eu^{3+} powders synthesized by hydrothermal method.*

The precursor molar ratios Ba/Ti=1.6 was fixed according with previous experiments proving the formation of $BaTiO_3$ reported by M. Boulos et al. [13]. The reafter, the suspension obtained above was transferred into cylindrical autoclave (Teflon lined stainless steel) filled at 2/3 of its volume. The autoclave was put inside the oven and the reaction was performed for 24 h at 200 °C. After cooling down to room temperature, the insoluble reaction products were washed several times using a solution 0.1 M HCl and water. Excess Ba^{2+}, Cl^-, K^+ ions were removed during washing. Finally the $BaTiO_3$ powders were oven dried at 90 °C for 24 h.

The general reaction for $BaTiO_3:Eu^{3+}$ powders synthesized by hydrothermal route are:

$$BaCl_2 \rightarrow Ba_2 + Cl^- \quad (11)$$

$$EuCl_3 \xrightarrow{MeOH} Eu^{3+} + Cl^- \quad (12)$$

$$K \xrightarrow{MeOH} K^+(CH_2)O^- + \frac{1}{2}H_2 \uparrow \quad (13)$$

$$Ba^{2+} + Cl^- + K^+(CH_2)O^- + Eu^{3+} \longrightarrow Eu^{3+}Ba(OCH_2)_2 + KCl \quad (14)$$

$$Eu^{3+}Ba(OCH_2)_2 + Ti(OCH_2(CH_2)_2CH_3 \longrightarrow BaTiO_3 : Eu^{3+} + CO_3 + CH_3OH + H_2O \quad (15)$$

4.3 Synthesis of $BaTiO_3:Ln^{3+}$ (Ln =Yb^{3+},Er^{3+}, Eu^{3+}) using sol-gel method (Table 4-1)

Sol-gel process allows synthesizing ceramic materials of high purity and homogeneity in a variety shapes: ultrafine powders with controlled shaped, films, fibers, aerogels, between others. In this work, $BaTiO_3:Ln^{3+}$ (Ln =Yb^{3+},Er^{3+}, Eu^{3+})powders and films obtained by sol-gel process are studied, since the concentration of dopant does not affect in the experimental procedure only keys system (Table 4-1) will be described.

a) Sol elaboration of $BaTiO_3:Ln^{3+}$ (Ln =Yb^{3+},Er^{3+}, Eu^{3+})

Ln^{3+} (Ln =Yb^{3+},Er^{3+}, Eu^{3+}) doped $BaTiO_3$ powders were prepared, using the sol-gel process, from barium 2,4-pentanedionate ($Ba(C_5H_7O_2)_2$, Alfa Aesar), titanium tetra-iso-propoxide ($Ti(OPr^i)_4$, 97 %, Aldrich), ytterbium chloride hydrate ($YbCl_3 \cdot 6H_2O$, 99.9%, Alfa Aesar) and erbium (III) nitrate hydrate ($Er(NO_3)_3 \cdot 5H_2O$, 99.9%, Alfa Aesar). Isopropylic alcohol (C_3H_7OH; 99.9%, Fermont) and water were used as solvents. The chelating chemical stabilizing agents were: glacial acetic acid (($C_2H_4O_2$), 99.8%, Fermont) and acetylacetone (2,4-pentanedione, $C_5H_8O_2$, ≥99%, Aldrich). The two experimental routes employed to obtain $BaTiO_3$:Er,Yb sols (with and without chelating agents) are depicted in Figs. 4-3 a and b respectively.

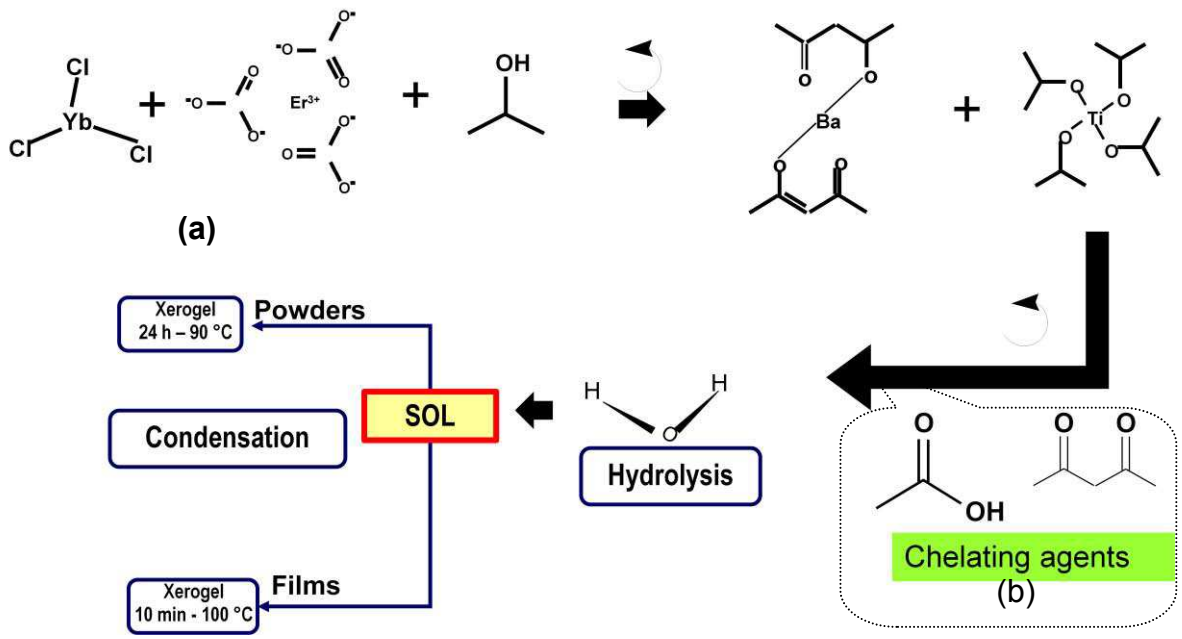

Figure 4-3. *Scheme synthesis for the elaboration of Ln^{3+} ($Ln = Yb^{3+}, Er^{3+}, Eu^{3+}$) doped $BaTiO_3$.*

In the first experimental procedure without chelating agents (Fig. 4-3a), both ytterbium chloride hydrate and/or erbium nitrate hydrate were mixed with isopropylic alcohol. The barium 2,4-pentanedionate is a more stable precursor to ambient moisture than barium alkoxides, and was dissolved with ytterbium chloride hydrate, erbium nitrate hydrate, and isopropylic alcohol solutions in molar ratios 0.89:0.06:0.05:20 after $Ti(OPr^i)_4$ was added. The solution was stirred for 24h and left to rest for 4 days at room temperature. When distilled water was added to the precursor solution as droplets under constant stirring, the hydrolysis reaction occurred immediately. At this stage, a clear yellowish sol with a concentration of 0.9 M was obtained. A portion of the sol was then maintained at 90 °C to yield a xerogel.

In order to elaborate $BaTiO_3$:Er,Yb systems (powders and films, Fig. 4-3b), it is of technical importance to obtain precursor solutions with long-term stability. For this purpose, the sol was obtained according to the first experimental procedure. Before the addition of water, the precursor solution was stabilized by adding acetylacetone and acetic acid. Chemical modification of the transition metal alkoxide with chelating ligands was used to control the condensation route and the evolution of the polymer [69]. (AcAc)H and

H-(OAc) were added in a complexation molar ratio Ti:(AcAc)H=1:10 and Ti:OAc=1:8. Then, distilled water was added to the precursor solution in a molar ratio of Ti:H_2O=1:40 and the hydrolysis occurred immediately. When we used acetic acid to chelate titanium isopropoxide to obtain a highly condensed product, an exothermic reaction took place, with the formation of (AcAc)H-Ti bonds.

By this method, stable transparent sols were obtained to produce reproducible films [70]. The pH was maintained at 5 for both experimental routes. The solution was stable for more than 4 months. Erbium nitrate was used instead of erbium chloride, erbium nitrate contributed to decrease the homogenization time in the solution. The main reactions of this synthesis are presented in Figures 4-4 and 4-5.

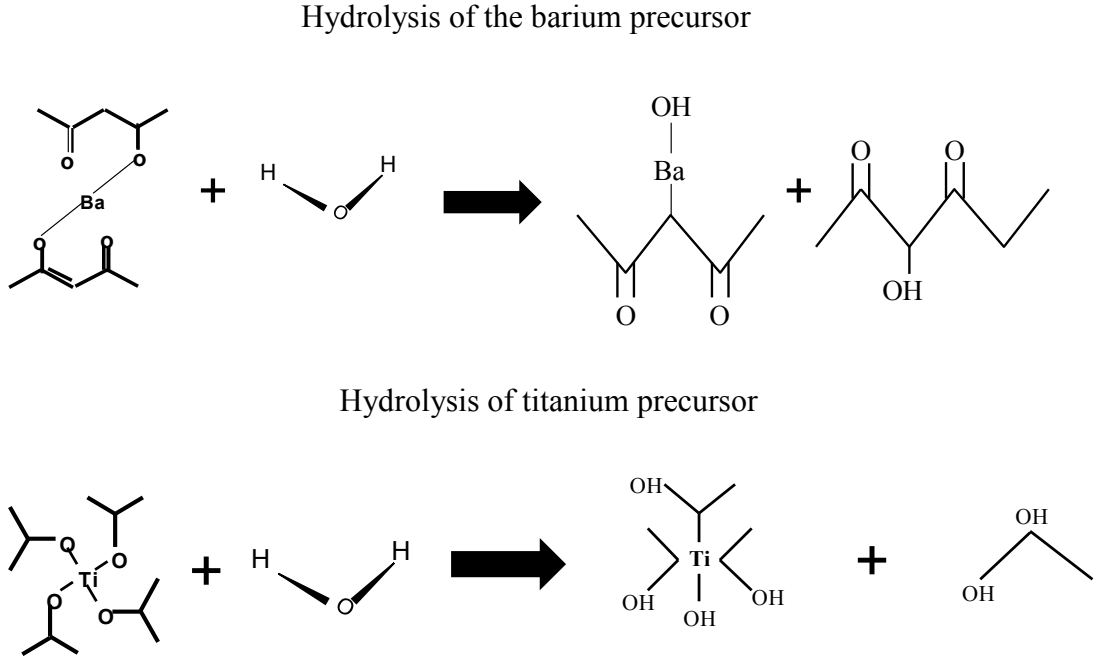

Figure 4-4 *General reaction of hydrolysis for the $BaTiO_3$ by sol-gel method.*

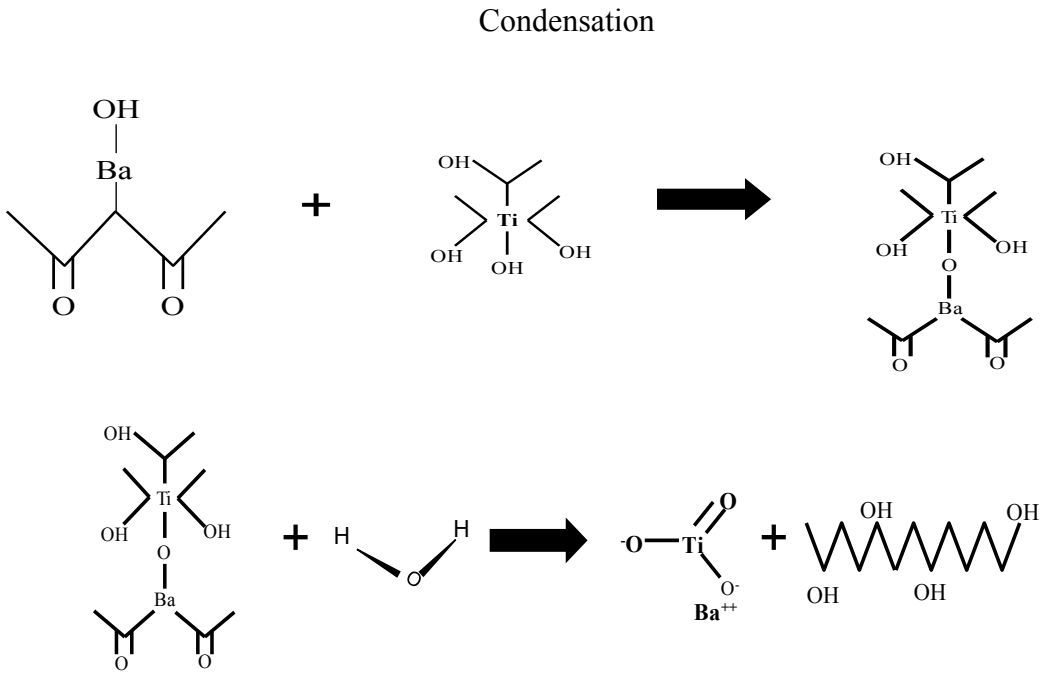

Figure 4-5. *General reaction of condensation for the $BaTiO_3$ by sol-gel method.*

From these sols, powders and films were elaborated. To include the study of powders is essential to know the material properties. The preparations of powders cheaper than to prepare films for this reason, it is convenient to work first with powders, considering the hypothesis that optical properties of the powders will be the same as for the films.

b) $BaTiO_3:Ln^{3+}$ (Ln=Yb^{3+},Er^{3+}, Eu^{3+}) ceramic powders

Precursor solutions and thin films synthesized with and without chelating agents were dried at 90 °C for 24h to evaporate the organic compounds and yield the $BaTiO_3$:Er,Yb xerogels. Finally, different thermal treatments were carried out on the xerogels prepared by the different routes at 300 °C, 500 °C, 700 °C, 950 °C and 1150 °C for 1h. Also, un-doped $BaTiO_3$ powders were prepared with chelating agents, using a similar procedure, as a reference. A general scheme for the powder elaboration is presented in Figure 4-6.

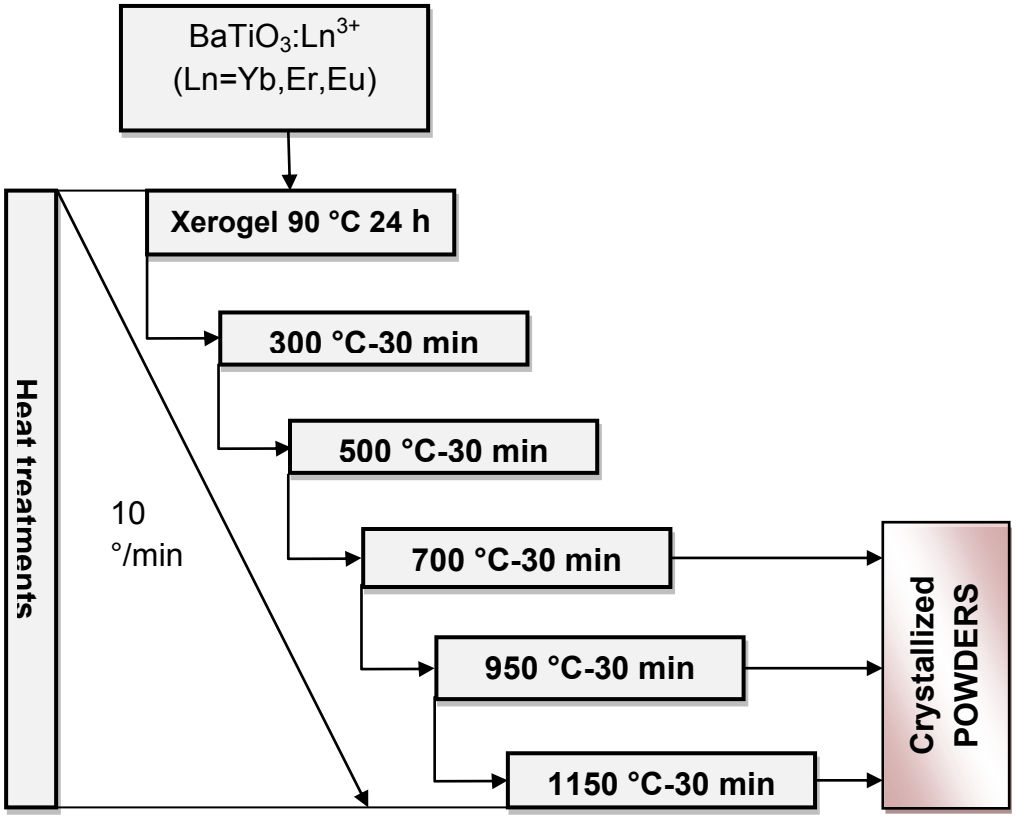

Figure 4-6. *Heat treatments of $BaTiO_3:Ln^{3+}$ ($Ln=Yb^{3+}$,Er^{3+}, Eu^{3+})powders by sol-gel method.*

c) $BaTiO_3:Ln^{3+}$ ($Ln=Yb^{3+}$,Er^{3+}, Eu^{3+}) thin films elaboration

$BaTiO_3:Ln^{3+}$ ($Ln=Yb^{3+}$,Er^{3+}) thin films [71] were obtained by the dip-coating technique, using sols with and without chelating agents (CA) and coated onto fine-polish optical silica substrates (Herasil from ®Heræus). To obtain optical and reproducible films, prior to the deposition stage the substrate was carefully cleaned using a special protocol [72]. Thereafter, silica substrates were wet uniformly with the precursor solution, which was previously, filtered using a 0.22 µm filter. The substrates were dip-coated using a withdrawal speed of 40 mm min^{-1} and annealed at 300 °C for 10 min between each coating until achieving 10 layers, with thermal treatments similar to those of xerogels. The dip-coating equipment used in the preparation of films is presented in figure 4-7.

Figure 4.7. *Dip-Coating equipment.*

d) $BaTiO_3$:Ln^{3+} (Ln=Yb^{3+},Er^{3+}, Eu^{3+}) thick films elaboration

The experimental route used to obtain $BaTiO_3$:Ln^{3+} (Ln=Yb^{3+},Er^{3+}, Eu^{3+}) thick films was as following. Barium 2,4-pentanedionate was dissolved in previous solutions (described in 4.3 (a)) by using chelating agents to decrease the reactivity of titanium alkoxide and to stabilize the sol. $Ti(OPr^i)_4$ was chosen because transition metal alkoxides are highly reactive due to the presence of strongly electronegative OR groups that stabilize the metal in the highest oxidation state and make nucleophilic attack on the metal possible [73,74]. The resulted stabilized sol was stirred for 2h, then water was added. At this stage, a clear yellowish sol with a concentration of 0.9 M was obtained. For the second experimental procedure with PVP, the *sol* was obtained according to the first experimental procedure, incorporating PVP in the initial solution in a molar ratio Ba/PVP= 0. 25 to elaborate rare earth doped $BaTiO_3$ thick films in a single step. This molar ratio was established from preliminary experimental work, the results of which showed that molar ratios higher than 0.25 resulted in non-transparent films.

Rare earth doped $BaTiO_3$ films were obtained by the dip-coating technique, using *sols* with PVP, and coated onto fine-polished optical silica substrates (Herasil from ®Heræus). To obtain optical and reproducible films, prior to the deposition stage the substrate was

carefully cleaned using a special protocol [72]. Thereafter, silica substrates were wetted uniformly with the precursor solution. The substrates were dip-coated using sols with PVP, and using a withdrawal speed of 0.0843 cm min^{-1}, respectively. The single layer obtained using the sol with PVP was annealed from room temperature up to 700 °C at 0.5 °C min^{-1}, resting 5 min at this temperature. The furnace was cooled at the same rate. The rare earth doped $BaTiO_3$ films were analyzed using different techniques, with the aim of studying the structural, morphological and luminescent properties.

Chapter 5. Results and discussion

Previously we have discussed the Eu^{3+} doped $BaTiO_3$ powders and films prepared by two routes: the solid state reaction and hydrothermal method. In this work, this matrix was also synthesized using the sol-gel method; this fact was supported by the reported studies which were specifically focused on the preparation of pure $BaTiO_3$ system by the hydrothermal method. Recently, many studies of the preparation of europium doped barium titanate have been carried out using the solid state reaction, to synthesize this system using the hydrothermal process it was important to optimize the synthesis conditions taking into account numerous reports to realize a comparative study.

Finally in this work, the sol-gel process was used to elaborate Yb and Er monodoped $BaTiO_3$ powder and film. For this purpose, in the sol-gel process, the use of chelatings agents was an important factor. The the incorporation of acetic acid, acetylacetone and the polyvinylpirrolidone allows us the preparation of optical films exhibiting 800 nm in thickness.

In this chapter the first results correspond to the thermogravimetric analyses corresponding to europium doped barium titanate synthesized by hydrothermal method.

5.1 $BaTiO_3$:Eu^{3+} synthesized by hydrothermal method

5.1.1 TG – TD analyses

Figure 5-1 shows the TG analysis of BT hydrothermal powder revealing some mass losses arising from the decomposition occurred in two steps.

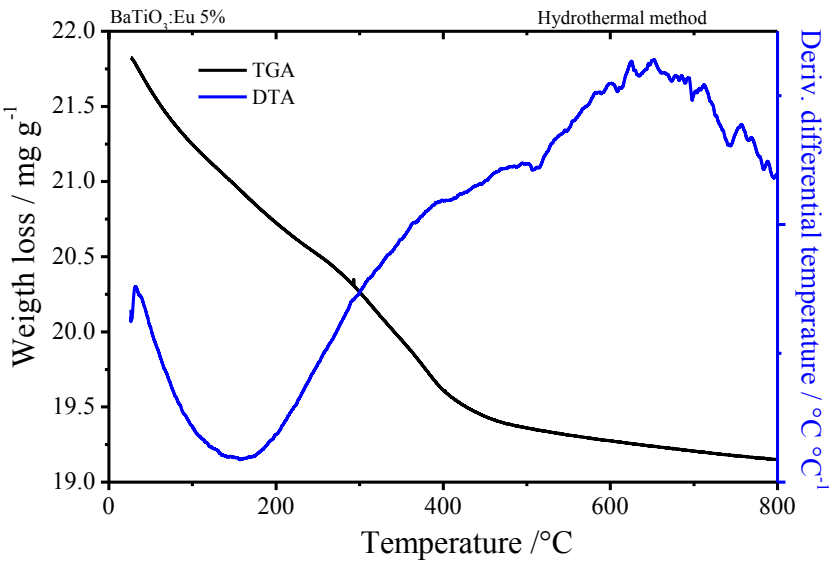

Figure 5-1. *DTA and TGA curves of $BaTiO_3:Eu^{3+}$ 5 mol% obtained from hydrothermal method.*

The TG curve revealed an amount of weight loss found out up to 800 °C which is lower compared than that observed for powders synthesized by solid state reaction. The first loss was found below 200 °C and this weight loss was attributed to the release of physisorbed OH^-, and chemisorbed OH^- at ranging temperature 200-420 °C. This chemisorbed water is considered as defects such as hydroxyl ions (OH^-), protons (H^+) and the carbonates (CO_3^{2-}) which are defectively incorporated into the lattice during the hydrothermal process achieved at high water pressure [1,75]. These defects stabilize the cubic phase, and hence decrease the tetragonality of the powder [75,76].

5.1.2 FT-IR analyses

Figure 5-2b shows the FT-IR spectrum of the (Ba-Ti) hydrothermal powder. The hydrothermal powder is characterized by a fundamental stretching band of hydroxyl (free and bonded) group in the $BaTiO_3:Eu^{3+}$ powder in the range 3600-3100 cm^{-1} and 1632 cm^{-1} arising of bending vibrations of coordinated H_2O as well as Ti-OH [77].

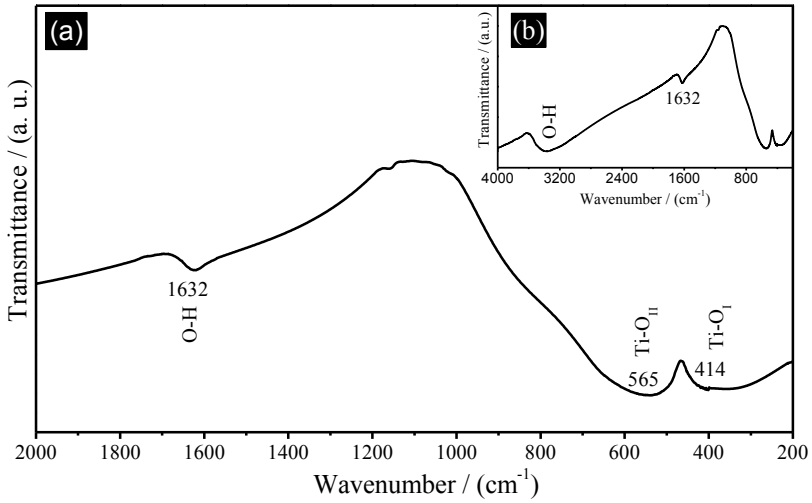

Figure 5-2. *IR spectra of $BaTiO_3$:Eu^{3+} 5% mol of hydrothermal powders.*

Figure 5-2a, presents two strong important bands, related to the (Ti-O) bond observed in the vicinity of 600-480 and 480-350 cm^{-1} and the center positions of 565 cm^{-1} and 414 cm^{-1}. This bands were found to almost agree with those of the Ti-O_I stretching vibration to the vertical and the O_I-Ti-O_{II} bending vibrations [78], respectively, of a TiO_6 (Figures 5-3 a-b shows symmetric and asymmetric vibrations) octahedron in the crystalline $BaTiO_3$ hydrothermal powders.

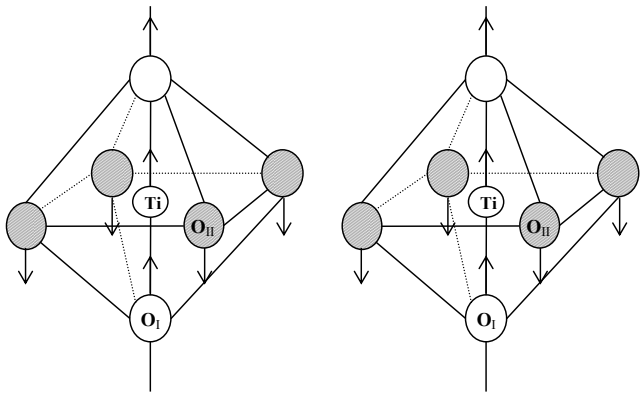

Figure 5-3. *Vibration modes of octahedricTiO_6 (a) symmetric and asymmetric (b) of Ti-O in $BaTiO_3$.*

5.1.3 X-Ray diffraction

The phases present in the $BaTiO_3$ powders after hydrothermal treatment were identified by recording the XRD pattern at room temperature. Fig. 5-4 shows the full XRD for the crystallized powder characterized by large diffraction peaks. This figure present also the peak situated at 2θ = 45° enlarged, in this case no splitting of the peak was observed. The crystallized phase of $BaTiO_3$ system is characteristic of a cubic perovskite structure formed at 200 °C and dried at 90 °C. The mean crystallite size was calculated from the broadening of the XRD peaks using the Scherrer formula [79].

$$D = \frac{K\lambda}{B\cos\theta}$$

Where, λ (nm) represents the wavelength of the Cu Kα radiation (1.54056 Å), θ is the Braggs's angle and *B* represents the full with at half maximum (FWHM), where $B = (B^2_{meas} - B^2_{equip})^{1/2}$. B_{meas}= measured FWHM and B_{equip} = FWHM due to instrumental broadening, K is Scherrer constant (it value depends on the crystal shape and the diffraction line indexes). Analyses of XRD peaks for various samples showed that crystallite size is approximately 20 nm.

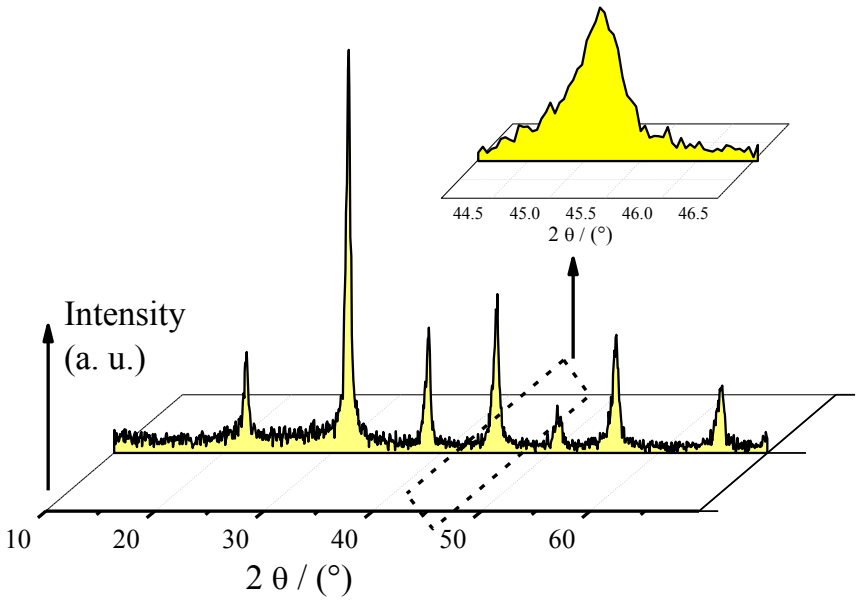

Figure 5-4. *XRD patterns of $BaTiO_3$:Eu^{3+}(5%) synthesized by hydrothermal process.*

To evaluate the stability of the barium titanate at high temperature, a sample from the Ba/Ti=1.6 molar ratio was heat treated from room temperature to 1200 °C in the HT-XRD chamber (Figure 5-5). The XRD patterns were taken every 30 min from room temperature since each pattern required approximately 30 min, the total calcination time for each temperature was one hour. Thus, for the specimen heat treated at 800 °C time around was 8 h. The cubic structure formed immediately after hydrothermal treatment was stable up to 800 °C.

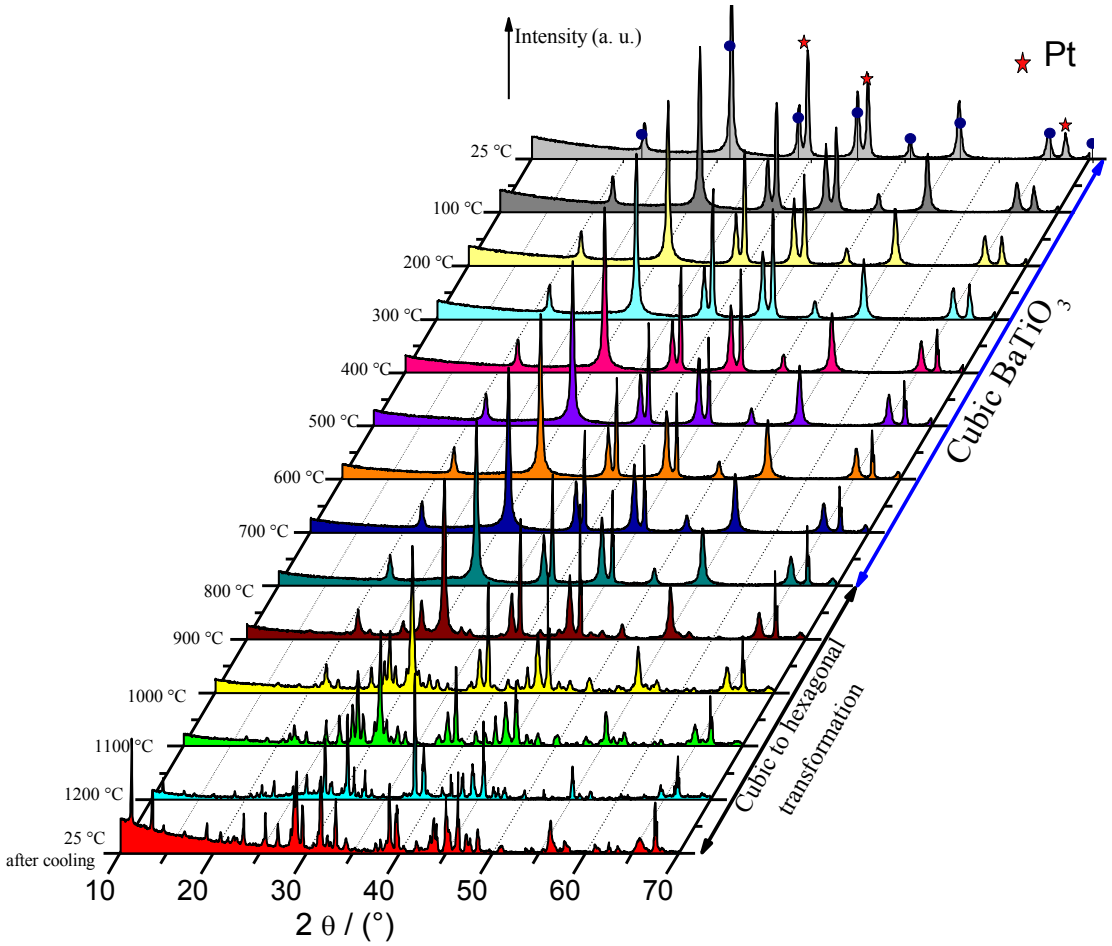

Figure 5-5. *HT-XRD patterns of $BaTiO_3:Eu^{3+}$ 5 mol % synthesized by hydrothermal process.*

At higher temperatures from 800 °C to 1200 °C, this structure reveals a mixture of cubic, hexagonal, $BaTi_2O_5$ indicating powder with poor purity as reported by S. Lee [80].

5.1.4 Raman spectroscopy

The Raman spectrum shown in Fig. 5-6 for hydrothermal $BaTiO_3$ powders reveal spectral features at 715, 515, 306, 260 and 185 cm^{-1}. [8,15]. Although, according to the selection rules, only active bands of $BaTiO_3$ with perfect cubic symmetry should be Raman inactive, predicting only infrared bands [81]:

$\Gamma_{optical} = 3F_{1u}$ (IR) + $1F_{2u}$ (inactive)

and in the tetragonal symmetry, 12 fundamental optical modes with the following irreducible representation are expected:

$\Gamma_{optical} = 3A_1$ (IR & R) + 4E (IR & R) + B_1

thus, all of the optic modes of tetragonal structure should be Raman active modes [82], the relation between Raman-active modes and wavenumber is still a matter of controversy as could be observed in Table 1.

In this investigation, the Raman spectrum of the hydrothermal $BaTiO_3$ powder present bands situated at [A1, E(LO4)] 718 cm^{-1}, A1(TO4) at 515 cm^{-1} can be assigned to the characteristic phonon modes of the tetragonal phase [83]. The peaks situated (B1,TO1-LO1) at 305 cm^{-1} is suggested to be characteristic of the tetragonal phase [83-87], and its absence could be related with the cubic crystal structure [13,83,88]. However the presence of this sharp peak is considered the tetragonal phase is not the dominant phase by some authors [8,89]. The Raman active mode A1(TO1) at around 260 cm^{-1} is ascribed to cubic phase when the [B1, E(TO1LO)] peak at ~ 305 cm^{-1} is not present [88,90,91], according to Boulos [13], the bands at 272 and [A1(TO), E(LO)] at ~ 183 cm^{-1} are highly related to the presence of cubic phase. Referring to Amami et al. [8] two sharp peaks (185 and 235 cm^{-1}) are associated to cubic phase. Nevertheless, it is accepted by many researchers that the Raman peak at around 260 cm^{-1}, which is somewhat variable, in relation to particles size, shape, and aggregation, is due to the characteristics of tetragonal $BaTiO_3$ [83, 85-87].

Table 5-1 *Raman modes presented in different $BaTiO_3$ crystallines structure.*

Method	Structure	$\nu_1(cm^{-1})$ [A1(TO), E(LO)]	$\nu_2(cm^{-1})$ [A1(TO)]	$\nu_3(cm^{-1})$ [B1, E(TO1LO)]	$\nu_4(cm^{-1})$ [A1, E(TO)	$\nu_5(cm^{-1})$ [A1, E(LO)]	Ref.
Hydro-thermal	"Cubic-rich"	185	260	306	515	715	This work
Hydro-thermal	Tetra-gonal	175	260	305	515	715	[83]
Sol-Gel	Cubic	185	260		519	720	[88]
Sol-Gel	Cubic	189		303	517	721	[89]
Hydro-thermal	Tetra-gonal			306	518	715	[84]
Sol-Gel	Tetra-gonal		245	303	510	710	[85]
Hydro-thermal	Cubic	183	272		516	707	[13]
Hydro-thermal	Tetra-gonal	187	260	300	515	716	[86]
Sol-gel	cubic	185	235	305	515	720	[92]
Hydro-thermal	Tetra-gonal		260	305	515	715	[87]
Sputtering	Pseudo-cubic	185	270		519	718	[90]

Finally, the origin of the above described bands in the cubic phase has been disputed due to the presence of Raman modes in this phase indicating that it does not have perfect cubic symmetry but with small distortions [93]. The origin of these bands observed in cubic phase has been disputed whether if they are disorder-induced first- or second-order Raman scattering. Recent temperature-dependent Raman studies on single-crystalline $BaTiO_3$ systems has shown that those bands are characteristic of first-order [94,95] due to the fact

that the cubic-to-tetragonal phase transition when cooling down the sample through the Curie temperature has not obviously taken place.

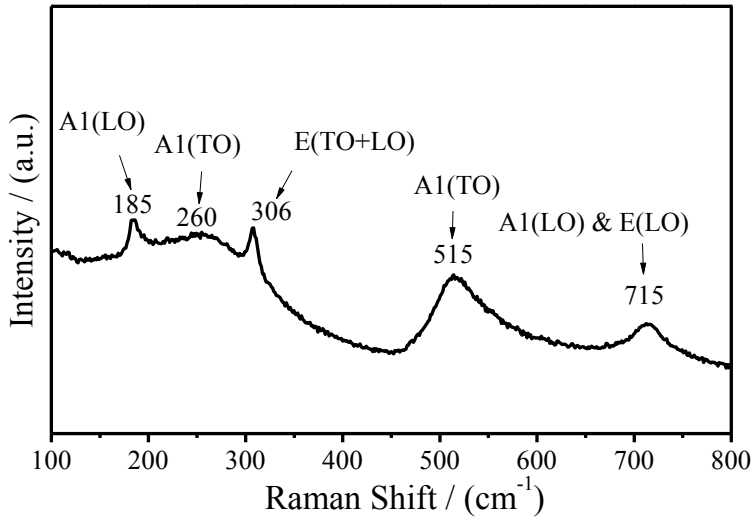

Figure 5-6 *Raman spectra of $BaTiO_3$:Eu^{3+} 5 mol% of hydrothermal powders*.

The presence of first-order Raman bands in $BaTiO_3$ nanopowders is explained by the occurrence of the distortion of the TiO_6 octahedra from the displacement of Ti along the cubic diagonals destroying the perfect symmetry and thus allows Raman activity in the cubic phase [96]. Also X. Zhu [83] suggest that the presence of structural defects in the small grains of the $BaTiO_3$ nanopowders, lead to high strains within the crystals and prevent the completion of the structural transition. The structural defects of $BaTiO_3$ nanopowders synthesized by hydrothermal method are accordingly to some authors [97] which are compensated by the creation of compensating defects like barium vacancies ($V_{Ba}^{"}$) on the surface of individual particles [75, 98-100]. By using these Raman-active modes discussed above, it could be concluded that tetragonal phase is present in the powders synthesized by hydrothermal method, nevertheless taking into account the observations related on the Raman mode situated at 305 cm^{-1} and the size of hydrothermal nanopowders, the dominant phase was not the tetragonal [83] resulting a "cubic-rich" $BaTiO_3$ structure, containing more amount of OH^- ions than that of the "tetragonal-rich" $BaTiO_3$ observed in the solid state reaction powders.

5.1.5 Scanning and transmission electron microscopy

The particle size and morphology were analyzed by SEM. Fig. 5-7a shows the SEM micrograph of $BaTiO_3:Eu^{3+}$ nanoparticles just after the product was washed and dried in an oven at 90 °C during 24 h. The particles produced using this route retain an expanded structure and the surface morphology is smoother and rounder which is typical of powders synthesized by hydrothermal route [83,101,102]. From this figure, it is observed the coalescence of nanocrystals. The basic forces responsible for agglomeration process are Van der Waals forces. To reduce surface energy, the primary particles have tendency to form agglomerates. By forming nearly spherical or equi-axed agglomerates, maximum packing density, minimum ratio of surface to volume and hence minimum surface energy can be achieved [103].

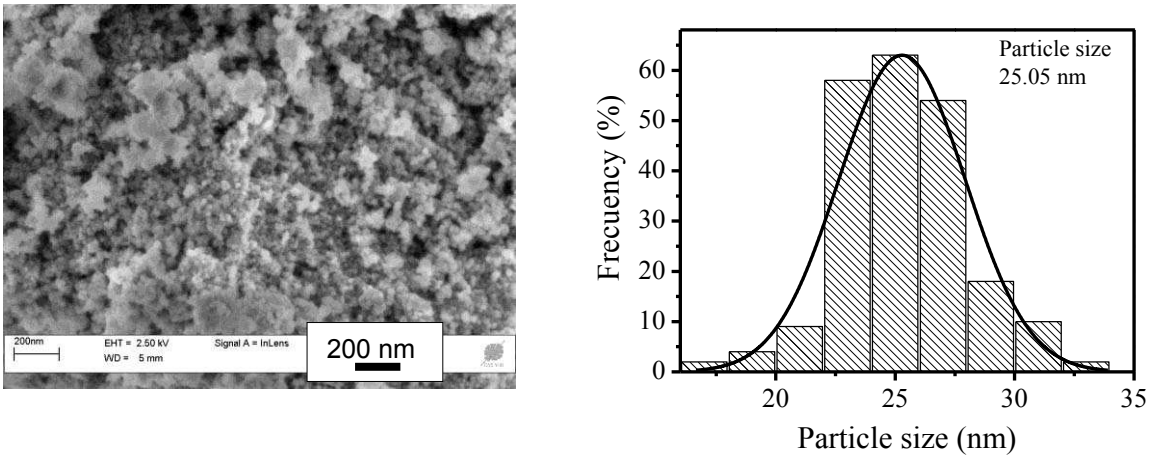

Figure 5-7. *SEM micrographs of $BaTiO_3:Eu^{3+}$ 5% mol of hydrothermal powders and their b) particle distribution.*

The average particle size distributions measured by image analyzer software, was statistically estimated to be ~25 nm as observed in Fig. 5-7b. From this result, it is stated that the surfaces of the nanoparticles were incorporated within the $BaTiO_3$ particle during the hydrothermal treatment, acted as lattice defects then hindered the transformation to tetragonal phase.

Fig. 5-8a shows TEM micrograph of $BaTiO_3:Eu^{3+}$ hydrothermal powders. In Fig. 5-8b it can be observed monosized distribution equi-axed particles of size 20 nm. The particle size as estimated by TEM micrographs was consistent with the Scherrer calculation from XRD analysis.

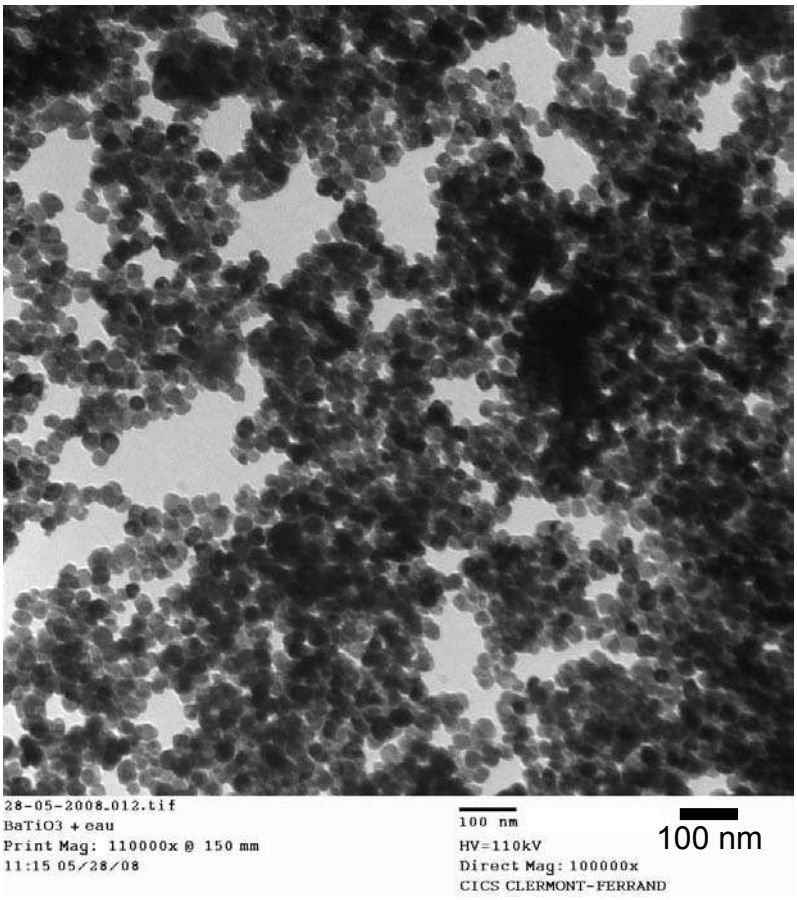

(a)

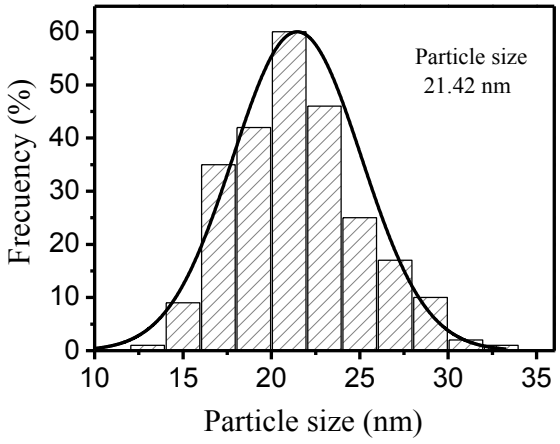

(b)

Figure 5-8. *TEM micrographs of $BaTiO_3:Eu^{3+}$ 5% mol of hm powders a), and particle distribution b).*

5.2 $BaTiO_3:Eu^{3+}$ synthesized by solid state reaction

5.2.1 TG – TD analyses

To understand the synthesis process for $BaTiO_3$, TGA/DTA measurements were performed for the $BaTiO_3$ solid state reaction powders (Fig. 5-10).

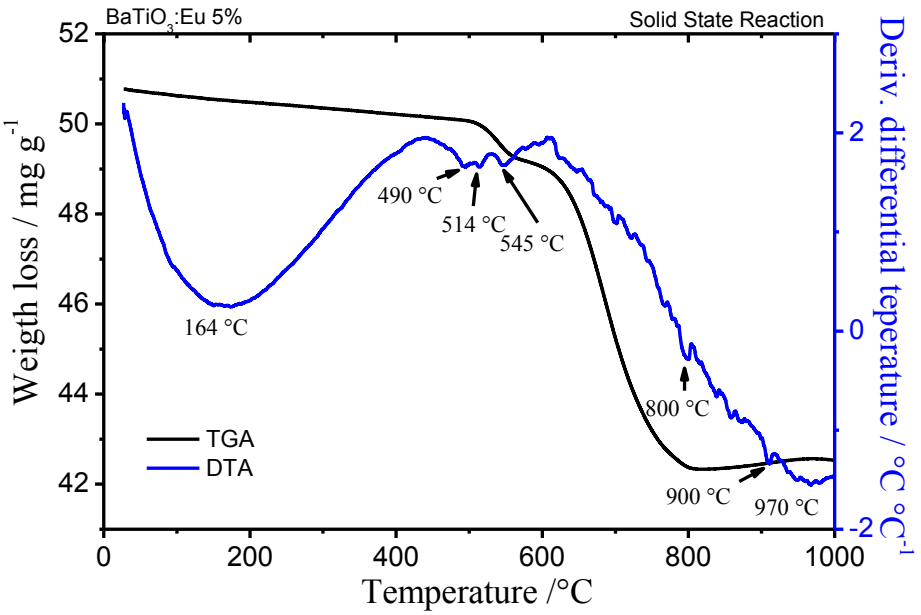

Figure 5-9. *DTA and TGA curves of $BaTiO_3:Eu^{3+}$ 5% mol obtained from solid state reaction method.*

The first endothermic phenomenon appearing in the range 20-300 °C, is accompanied by a minimal mass loss interpreted as a physical transformation. The next important event reveal an important mass loss starting from 600 to 800 °C corresponding to a large endothermic peak observed at around 800 °C arising to the transition from witherite orthorhombic $BaCO_3$ to the rhombohedral phase and the formation of $BaTiO_3$ occurring from 800 to 1000°C according to the reaction: $BaCO_3+TiO_2 \rightarrow BaTiO_3+CO_2$.

5.2.2 FT-IR analyses

FTIR spectrum of the $BaTiO_3$ solid state reaction powder is presented in Fig. 5-10. Two weak bands attributed to the vibrations in CO_3^{-2} situated at 1430 cm^{-1} and 860 cm^{-1} are assigned to asymmetric stretching vibrations $\upsilon_s(COO^-)$ and bending out of plane vibrations of carboxylic groups respectively [104]. Also a weak large absoption band at about 1021 cm^{-1} is attributed to the alcoholic C-O stretching vibrations [105].

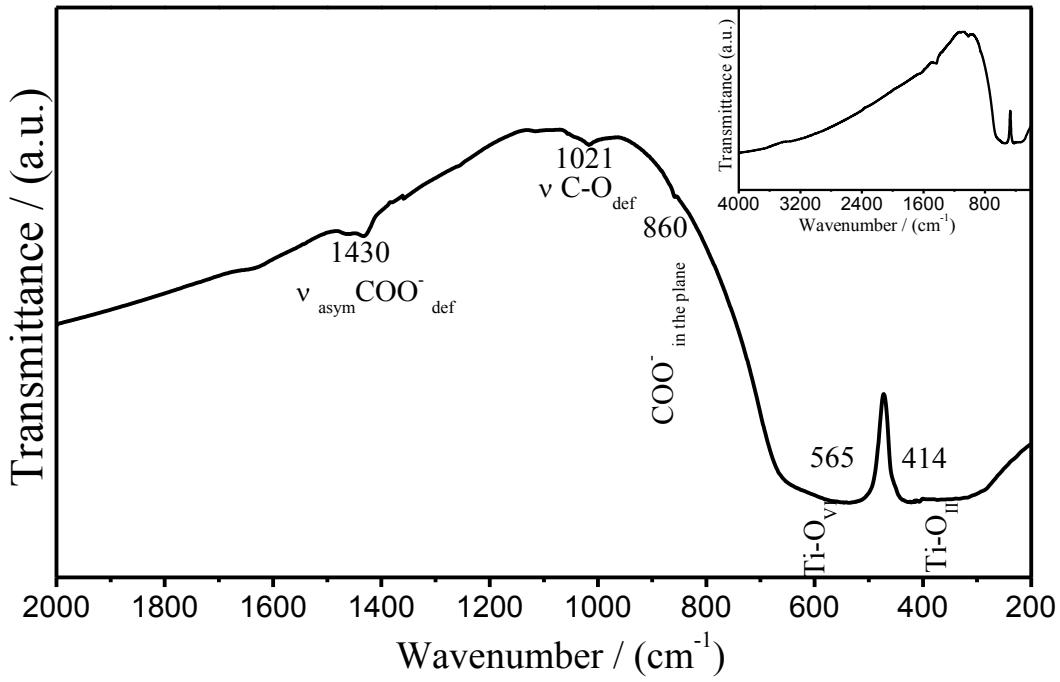

Figure 5-10. *IR spectra of $BaTiO_3$:Eu^{3+} mol% of solid state reaction powders.*

The characteristic infrared bands of $BaTiO_3$:Eu^{3+} are situated at 1410 cm^{-1} and 615 cm^{-1} corresponding to Ba-Ti groups and the occurrence of the TiO_6 octahedral connected with each other [106] and also is due to Ti-O_I stretching normal vibrations [107] of TiO_6 octahedra, while the weaker and broad peak at around 472 cm^{-1} can be attributed to Ti-O_{II} bending normal vibrations [108]. The weak peak situated around 560 cm^{-1} is attributed to the TiO_6 stretching vibrations connected to the barium [41].

5.2.3 Structural and microstructural analyses of $BaTiO_3:Eu^{3+}$ powders. Raman spectroscopy, X-ray diffraction and scanning electron microscopy

Raman characterization

There are detailed studies related to description of the Raman spectroscopy dependence on the temperature to probe local structure and symmetry changes on $BaTiO_3$ [109,110]. Raman scattering has been used as a powerful tool to investigate the evolution of Raman spectrum as a function of grain size, broadening of bands, frequency shifts and absence of some Raman active modes [111]. Also, Raman spectroscopy has been used to determine the coexistence of different multiphase in $BaTiO_3$ nanocrystalline ceramics [76,112,113]. To characterize the evolution of bonding and structure in $BaTiO_3$ solid state powders, the Raman spectrum of the sample with Eu/Ti= 5 % mol was collected at room temperature and is shown in Fig. 5-11.

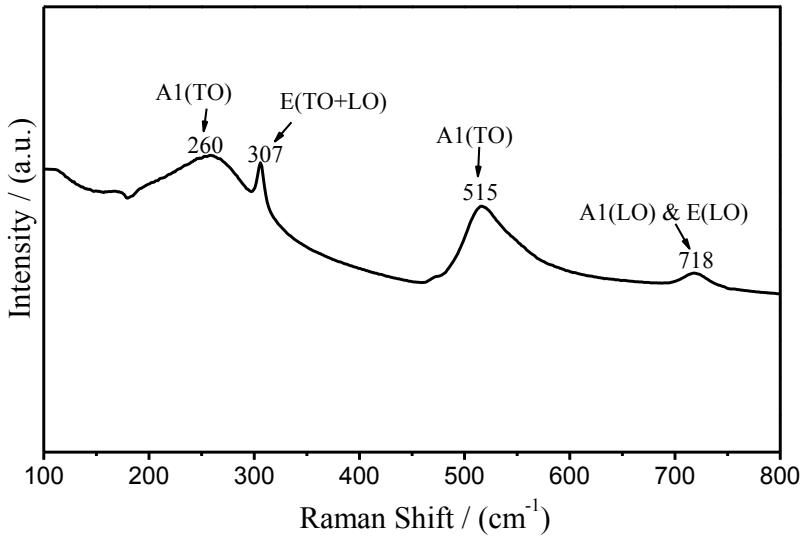

Figure 5-11. *Raman spectra of $BaTiO_3:Eu^{3+}$ 5 mol % of solid state reaction powders.*

According to Busca [99] and Lu [86], for cubic $BaTiO_3$ only infrared active bands without first-order Raman activity were predicted being only the three triply degenerate IR-active modes, while for tetragonal eight Raman-active modes (7 are IR active) were detected. From this figure it was observed the Raman fundamental modes (P4mm) 4E(TO+LO) + $3A_1$(TO+LO) + $1B_1$(TO+LO) [88] expected for tetragonal $BaTiO_3$ powders [114,115].

According to Kaiser et al. [116] and Asiaie [87], the weak shoulder below 300 cm^{-1} belongs to a A_1(TO+LO) phonon mode. The peak at ~307 cm^{-1} corresponds to a E(TO+LO) phonon mode of tetragonal $BaTiO_3$ [117]. The strong band peaking at ~ 515 cm^{-1} is attributed to a A_1(TO) phonon mode of tetragonal and cubic [118].The weak peak at ~ 718 cm^{-1} has been associated with the highest frequency longitudinal optical mode (LO) of A_1 symmetry.

XRD studies

To investigate the structural characteristics of the $BaTiO_3$:Eu^{3+} synthesized by solid state reaction, the sample were put directly in the HTXRD chamber just after the ball milling (without 4 h heat treatment at 1150 °C). Figure 5-12 shows the HTXRD diffraction patterns.

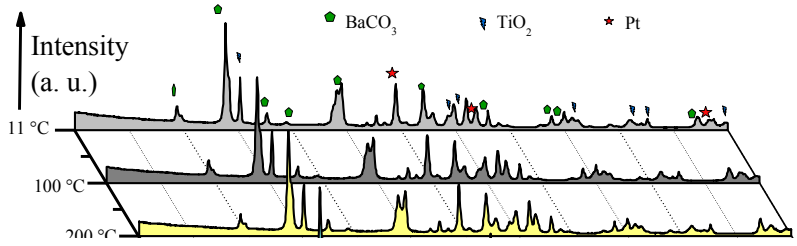

Figure 5-12. *HTXRD patterns of $BaTiO_3$:Eu^{3+} 5 mol% of solid state reaction powders.*

The first scan corresponds to the pattern for the as-synthesized $BaTiO_3:Eu^{3+}$ powder at room temperature. However, this powder reveals the presence of the $BaCO_3$ and TiO_2 up to 700 °C as can be observed in this figure. In the following scans between 700 and 1100 °C the powder began to crystallize, displaying some traces of $BaCO_3$. The complete crystallization of $BaTiO_3$ powder occurs above 1100 °C. Alternatively, the XRD pattern of $BaTiO_3:Eu^{3+}$ powders heat-treated at 1150 °C were recorded at room temperature. Figure 5-13 reveals fully crystallized and high purity barium titanate powders after 4h, confirmed by the absence of any $BaCO_3$ in both IR spectrum and XRD proving the completion of reaction.

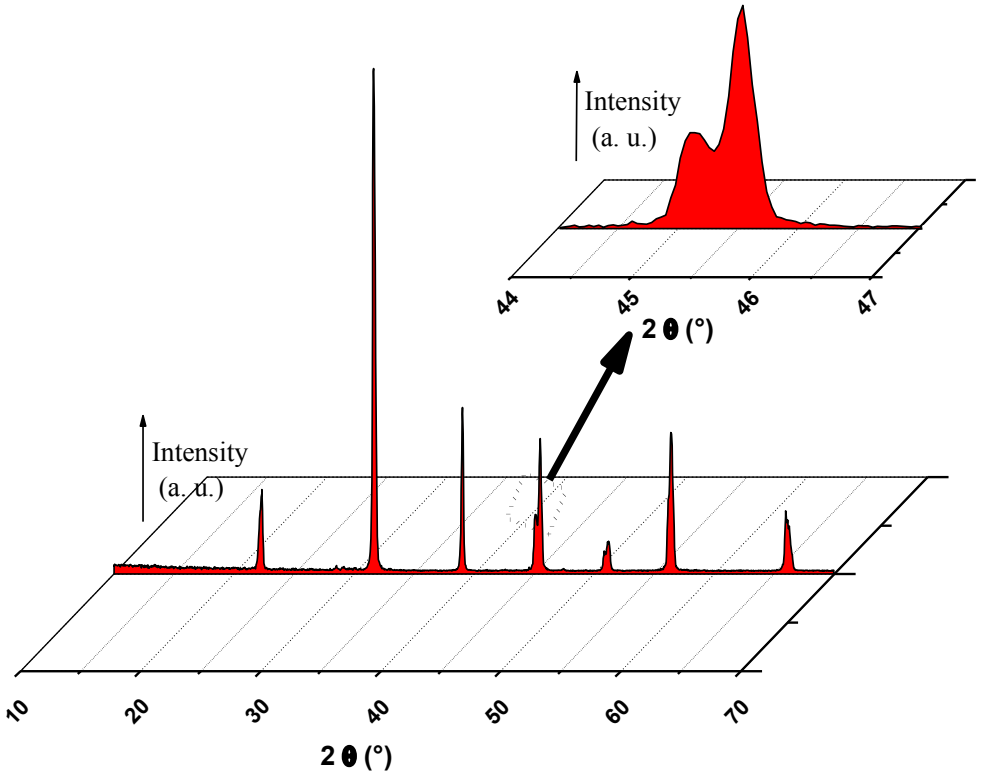

Figure 5-13. *XRD pattern of $BaTiO_3:Eu^{3+}$ 5mol% of solid state reaction powders.*

Fig. 5-13 shows the full XRD 2θ range of the crystallized powder and to solve the peaks for (0 0 2) and (2 0 0) planes at the peak was enlarged as shown in Fig. 5-13. This splitting is characteristic of tetragonal $BaTiO_3$ [119].

Morphological studies SEM

Fig. 5-14 shows SEM results for the $BaTiO_3$:Eu^{3+} powders obtained by solid state reaction method calcined 4 h at 1150 °C.

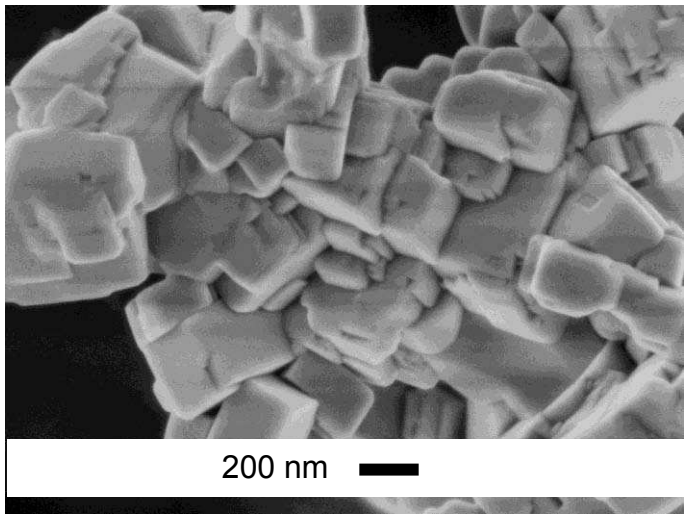

Figure 5-14. *SEM micrographs of $BaTiO_3$:Eu^{3+} 5 mol% of solid state reaction powders.*

As shown, the morphology of the resulting product consist of cube like $BaTiO_3$ particles well crystallized in tetragonal structure, in general the particles show noticeable agglomeration and basically present regular shape with average size of about 200 nm.

5.3 Comparative analyses of $BaTiO_3$:Eu^{3+} results synthesized by hydrothermal and solid state reaction methods

From infrared and structural studies carried out on $BaTiO_3$:Eu^{3+} powders obtained from hydrothermal and solid state reaction methods some aspects are important to point out. Both systems present adsorbed water in the lattice situated on the particles surface [120]. Additionally, the powders obtained by hydrothermal process present OH^- groups. These OH^- groups are considered as structural defects of $BaTiO_3$ and those are included on the lattice, these defects are compensated by the barium vacancies ($V_{Ba}^{"}$) created on particles surface to maintain the neutrality [121-124]. Viekanandan et al. [97] suggest that the presence of crystal stress are related with punctual defects in the lattice and also by the

presence of metastable cubic phase at room temperature resulting of compensation of residual hydroxyls ions in the oxygen lattice by cations vacancies. Shi et al. [125] reported the stabilization of cubic phase by the hydrothermal method, provoked by the presence of OH- on the surface and by the barium vacancies. In both systems it is possible to observe the characteristic Ti-O infrared bands of $BaTiO_3$ presented at 565 cm^{-1} y 414 cm^{-1} [23].

The crystalline structure of $BaTiO_3$ reveals that the powders elaborated by hydrothermal process are characterized for presenting cubic structure and spherical particles with mean diameter size of ~25 nm, characterized by only one diffraction peak situated at 45°, while the samples obtained by solid state reaction present a splitting of the 45° peak attributed with the presence of tetragonal phase. Additionally the mean particle size characterizing the solid state powders correspond to approximately 200 nm with cubic morphology. By using the Raman spectroscopy it was possible to confirm that tetragonal structure is not the dominant phase in the powders prepared by hydrothermal method due to the presence of Raman mode at 305 cm^{-1} and particle size [119]. This fact shows that hydrothermal powders reveals a $BaTiO_3$ "cubic phase" matrix rich with more OH^- ions than those observed for solid state reaction powders.

5.4 $BaTiO_3:Ln^{3+}$ (Ln =Yb^{3+},Er^{3+}) system synthesized by sol-gel method

5.4.1 FT-IR study

Thermal evolution of the organic compounds on both chelating and non-chelating xerogels, heat treated at 90, 300, 500, 700, 950 and 1150 °C for 1h were detected by FT-IR and the results are shown in Figs. 5-15, and 5-16. Both experimental procedures displayed the evolution of the organic compounds at the evaluated temperatures. Fig. 5-16 shows the infrared spectra of the $BaTiO_3$:Er,Yb without complexing agents (WOCA).

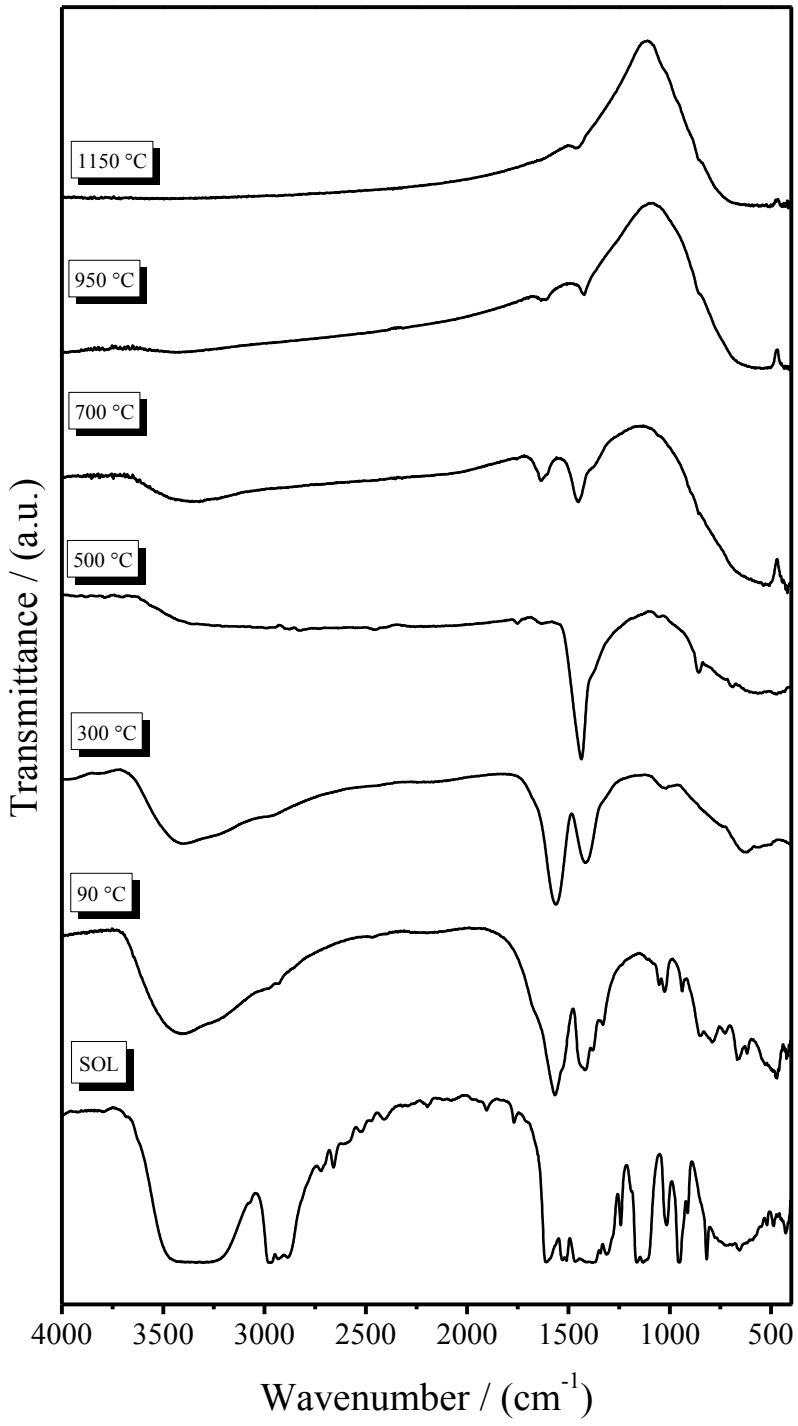

Figure 5-15. *Infrared spectra of BaTiO:Er,Yb powders heat treated at different temperatures without chelating agents (WOCA).*

The band situated at ~3400 cm^{-1} corresponds to the symmetric and asymmetric vibrations of weakly bonded water interacting with its environment via hydrogen bonding, and to the stretching vibrations of hydrogen-bonded OH groups [74]. The intensity of the infrared band in the sol is stronger than that of the xerogel; this is probably due to the fact the O-H bonds form a chelate organic complex. The absorption bands at 3000-2800 cm^{-1} are related to C-H stretching vibrations; the decreasing intensity of these bands, from sol to gel, is due to the evaporation of the isopropylic alcohol and other organic solvents in the system. The infrared spectra of the $BaTiO_3$ without chelating agents indicates that the two absorption bands at around 1534 and 1401 cm^{-1} are due to the organic groups, but these bands are almost masked by the carboxylate bands assigned to the asymmetric and symmetric –C-O–Ti and –C-O–Ti stretching vibrations, respectively. Kamalasan et al. [74] reported that the bands of the $BaTiO_3$ infrared spectrum are due to the titanium-acetilacetone ligands which are overlapped by carboxylate bands. It is noted that these peaks are overlapped by the C=C-C resonance peak. These bands are situated at 1565 and 1423 cm^{-1} in the xerogel. In the spectra of the gel (Fig. 5-15), the IR absorption bands due to titanium isopropoxide at 656 cm^{-1} are assigned to (Ti-O-Pr^i) and to CO stretching metal (Ti, Ba) alkoxides at around 1000 cm^{-1}. The peaks situated at 860 and 463 cm^{-1} are attributed to Ba-O and Ti-O stretching vibrations. The bands around 800 and 400 cm^{-1} are ascribed to the formation to metal oxide bonds (M-O) and appear wider and flatter in sol and powders heat treated up to 500 °C, while the bands become sharper and narrower at higher temperatures (e.g. 700 and 950 °C). When the temperature increased up to 700 °C, this compound disappeared, due to the crystallization of the $BaTiO_3$ structure. Due to the decreasing number of vibration molecules with the transformation of amorphous TiO_2 to the TiO_6-octahedra characteristic of the perovskite lattice, the typical band due to TiO_I stretching appeared at 564 cm^{-1}.

Figure 5-16 shows the IR spectra of $BaTiO_3$:Er,Yb powders with chelating agents. The region situated around 3420 cm^{-1} displayed O-H stretching vibrations and bands related with the C-H stretching vibrations in the range 3000-2800 cm^{-1}; for both regions, infrared bands displayed much lower intensity, and a significant reduction of organic content in xerogels was observed as the temperature increased.

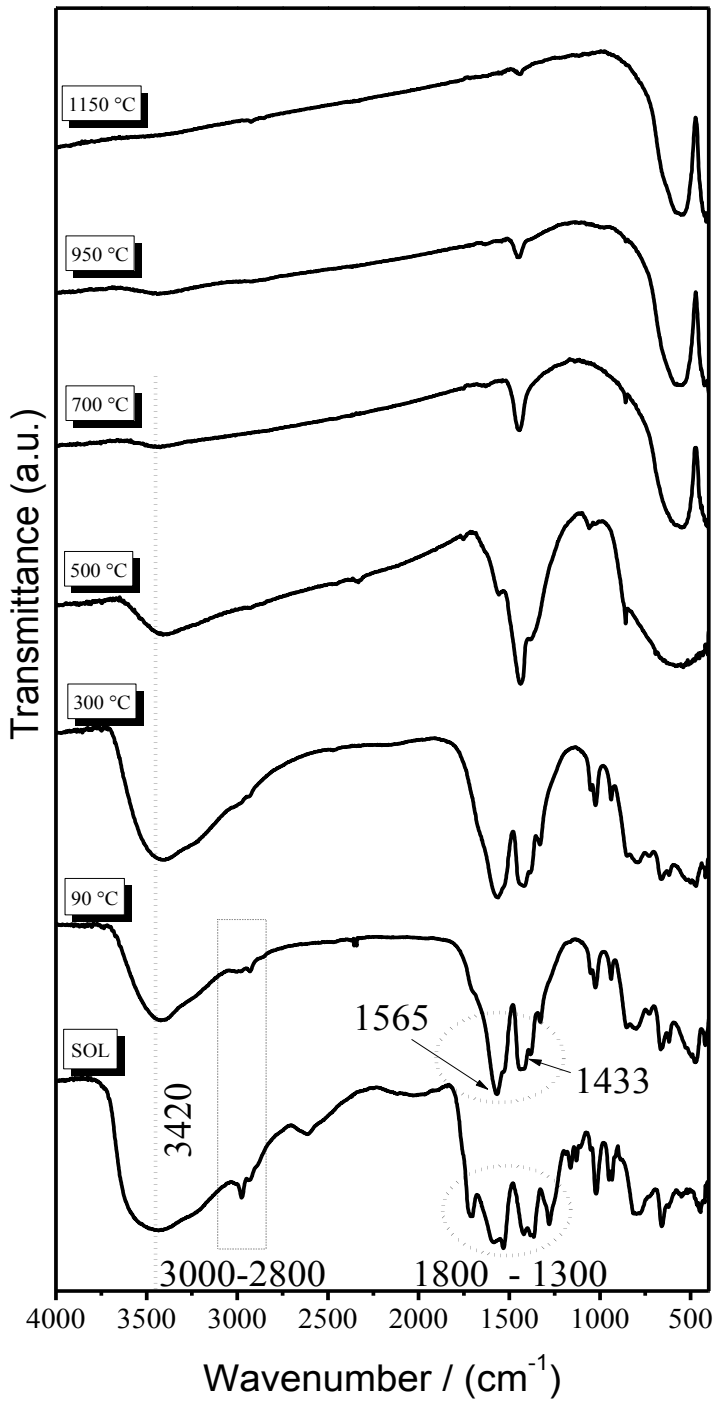

Figure 5-16. *Infrared spectra of BaTiO:Er,Yb powders heat treated at different temperatures with chelating agents (WCA).*

The main infrared bands between 1800 and 1300 cm^{-1} (sol), and in gel powder thermally treated at 90 and 300 °C, were produced by the intermediate products of Ti $(O\text{-}iPr)_4$ reacting with (AcAc)H and H-(OAc); the intensity of these bands becomes weaker as the temperature increases. For example, the two regions of bands situated at 1718-1530 cm^{-1} and 1420-1350 cm^{-1} changed to distinct bands located at 1565 cm^{-1} (ν_s) and 1433 cm^{-1} (ν_{as}), indicating the formation of a COO^--Ti (ν_s) complex coupled with O-H bending vibrations and C-O stretching vibrations. These C-O-Ti vibrations are attributed to the asymmetric and symmetric stretching modes of COO^- (ν_s) and COO^- (ν_{as}).

The -C-O- groups come from the (AcAc)H and H-(OAc), confirming the existence of a substitution reaction with chelatings agents. The presence of the (AcAc)H allows the decrease of titanium alkoxide and the stabilization of the sol as follows:

$$M(OR)_4 + (AcAc)H \rightarrow M(OR)_3(AcAc) + R\text{-}OH \quad (1)$$

$Ti(OPr^i)_4$ was chosen because it is known that the transition metal alkoxides are highly reactive due to the presence of strongly electronegative OR groups that stabilize the metal in the highest oxidation state and make the nucleophilic attack on the metal possible [126,127]. Such alkoxides are used as precursors in sol-gel processing because they are strongly electrophilic and thus less stable in hydrolysis, condensation, and other nucleophilic reactions. According to Thiele et al. [128], the frequency separation ($\Delta\nu$) between these two peaks strongly depends on the bonding modes of the acetate (-COO-) group, and four types of bonding modes of the acetate group to metal ions are possible: (a) mono-dentate, (b) chelating, (c) bridging ligands and (d) ionic bond; the largest (425 cm^{-1}) is in the monodentate ligand mode, and the smallest (135 cm^{-1}) is in the chelating one. For the present study, titanium isopropoxide $Ti(OPr^i)_4$ with a $\Delta\nu$ value of 138 cm^{-1} is more likely to exist in chelating acetate groups [129]. The ring of the acetylacetone ligands is very stable. The reduction of the number of functional groups and presence of the bulky (AcAc)H ligands of the titanium ions prevent the condensation of the titanium (AcAc)H molecules. Acetic acid (OAc) decreases the kinetics of hydrolysis and polycondensation via an esterification reaction [130].

$$M(OR)_4 + H\text{-}(OAc) \rightarrow M(OR)_3(OAc) + R\text{-}OH \quad (2)$$

This process depends on charge distribution in the alkoxide and the transition states. As a simple criterion, both the metal atom M and the leaving group ROH have to be positively charged to ensure repulsion. An estimate of the charge distribution can be deduced from the PCM (Partial Charge Model) [131]. As previously mentioned for the synthesis of $BaTiO_3$:Er,Yb systems, titanium isopropoxide, isopropylic alcohol and acetylacetone were used. Then, the calculations performed for $Ti(OPr^i)_4$ and H-(OAc) show that in the transition state $\delta(AcOH) = -0.7$, while $\delta(C_3H_7OH) = +0.1$. The negatively charged acetate group remains bonded to titanium (eq. 2). In the case of $Ti(OPr^i)_4$ and (AcAc)H, in the transition state $\delta(AcAc)H = -0.46$, while $\delta(C_3H_7OH) = +0.09$. Acetylacetone is strongly bonded to the metal atom and cannot be removed upon hydrolysis. In both cases, the positively charged alcohol molecules are removed.

Only one band was observed in the region 1020-1050 cm^{-1} in samples dried at 300 and 500 °C. It means the C-O-C bonds have broken up, indicating that hydroxyls and organics present in the precursor were removed. The bands around 860 cm^{-1} of the samples dried at 300 and 500 °C are related to the formation of carboxylate during the oxidative decomposition of the alkoxide radicals. These bands, as well as those associated with the chelating ligands, disappear after heat treatment at temperatures equal to or above 700 °C, clearly revealing the formation of a residual carbonate phase in calcined gels related to an absorption band at around 1450 cm^{-1} at 700, 950 °C and 1150 °C. The band present at ~ 421 cm^{-1} can be attributed to normal TiO_{II} bending vibrations [108]. The weak peak around 564 cm^{-1} is due to the TiO_I stretching vibrations connected to the barium [41]. The most important infrared characteristic regions present for the three temperatures are related to the Ti-O bond and are observed in the vicinity of 600-480 and 480-400 cm^{-1}, attributed to the TiO_I stretching vibration and the O_ITiO_{II} bending vibration, respectively, of a TiO_6 octahedron in the crystalline $BaTiO_3$:Er,Yb [88].

5.4.2 X-Ray diffraction analyses

Figs. 5-17 a-c show the characteristic X-ray diffraction patterns of $BaTiO_3$:Er,Yb powders obtained with and without chelating agents.

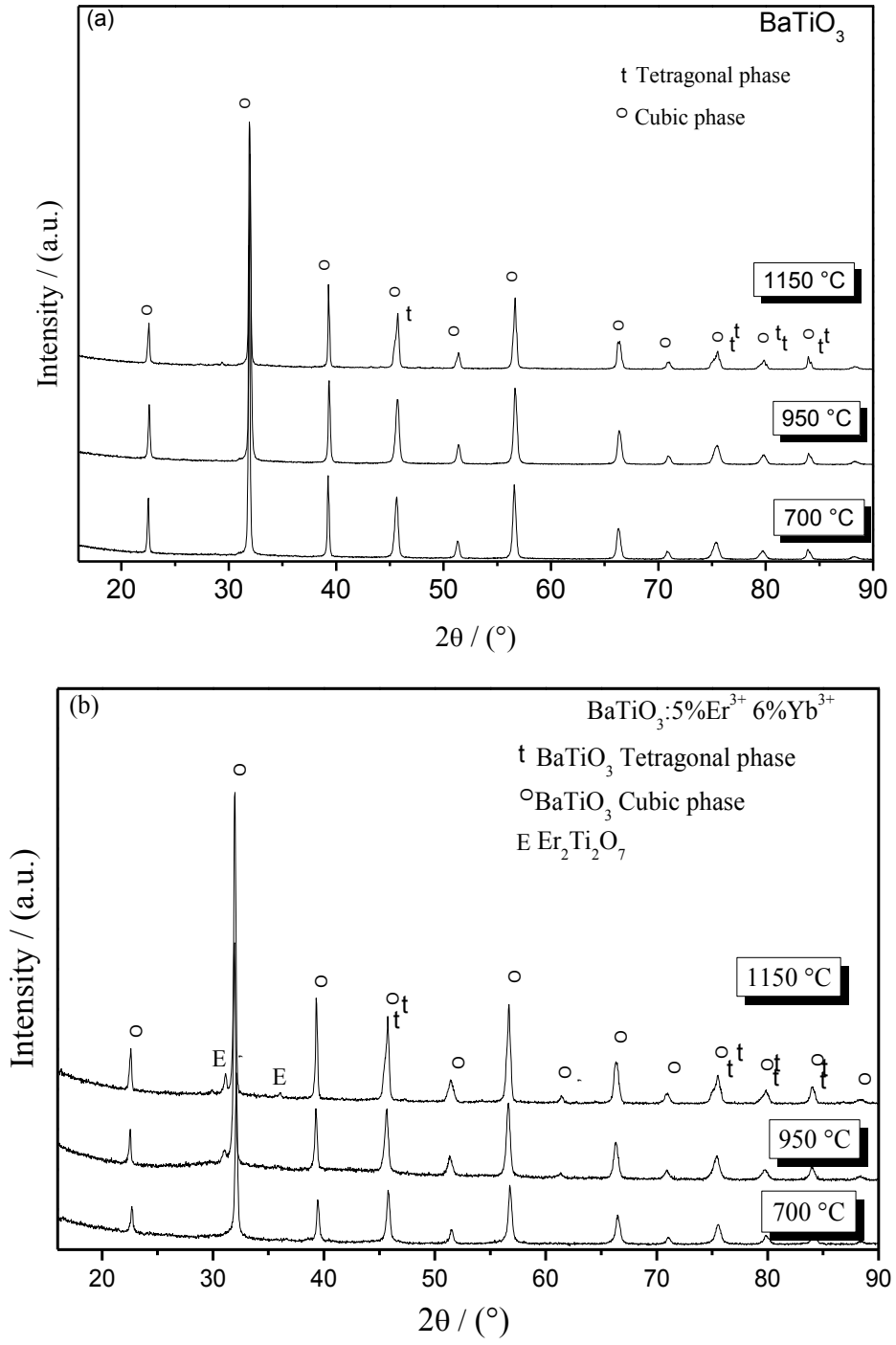

Figure 5-17. *XRD patterns of $BaTiO_3$ (a), non chelating (b) and chelating $BaTiO_3$:Er, Yb (c) powders heated at different temperatures.*

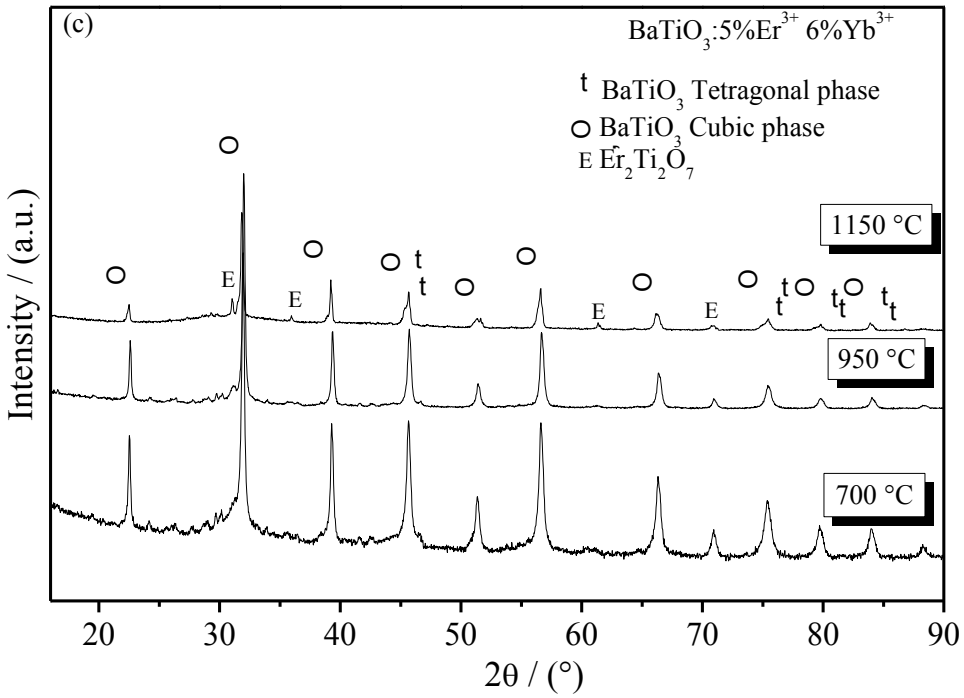

Figure 5-17. *XRD patterns of $BaTiO_3$ (a), non chelating (b) and chelating $BaTiO_3$:Er, Yb (c) powders heated at different temperatures (contin.)*

As a reference, un-doped powders ($BaTiO_3$) in the presence of chelating agents have been analyzed in relation to thermal treatment temperatures (Fig. 5-17a). In this figure, it is seen that the change of the peak intensity is not significant, which could indicate that the fully crystalline $BaTiO_3$ powders had already formed at 700 ºC. However, it can be seen that peaks split at around 2θ = 45, 75, 79, and 84º as a result of the tetragonal phase in this figure, which may imply that the crystalline tetragonal phase of $BaTiO_3$ particles is better formed at higher temperatures. The tetragonal phase was detected in addition to the cubic phase (Fig. 5-17a), indicating the coexistence of the tetragonal phase and the cubic phase, as was observed by Cernea et al. [132].

The Rietveld refinement of the XRD provides precise information about the amount and the lattice parameters of the tetragonal and cubic phases in annealed treatment $BaTiO_3$ powders. The weight fractions of the tetragonal and cubic phases, based on the refined scale factors for the two structural phases, were 26.70% and 73.30%, respectively, at 700 °C. At higher temperatures (950 and 1150 °C), the tetragonal phase is the predominant one (52.17

and 59.74 %, respectively) as revealed by the peaks splitting at around 2θ = 45° in the X-ray diffraction pattern presented in Fig. 5-17a.

Fig. 5-17 also shows XRD diffraction patterns of doped $BaTiO_3$:5%Er, 6%Yb powders prepared at different temperatures without (Fig. 5-17b) and with (Fig. 5-17c) chelating agents. The peaks of $BaTiO_3$ powders, including cubic-tetragonal transformation, are present in both figures. It is well known that the presence of dopants has an effect on the crystal structure, and in this erbium concentration the $Er_2Ti_2O_7$ compound appears as a secondary phase. This erbium stoichiometric pyrochlore has three characteristic peaks at around 2θ=32, 36 and 61º. The pyrochlore $Yb_2Ti_2O_7$ is only detected when single crystal fibers of nanocrystals of $BaTiO_3$ are doped equal to or more than 5 at.% Yb^{3+} [93]. The secondary phase of $Er_2Ti_2O_7$ could have an optical effect on the SHG generation presenting its signal, which is related to the presence of $BaTiO_3$ tetragonal phase particles and the grain size [89]. Additionally, traces of $BaTi_2O_5$ and Ti_8O_{15} compounds were observed, this fact is attributed to the chemical reaction between TiO_2 and the $BaTiO_3$ matrix itself (as observed by Yu et al. [133]). Annealed samples showed an increase of the tetragonality concurrent with the increase of calcining temperature, which could be a direct consequence of the particle size [134-136].

5.4.3 Microstructure of powders

The microstructure of the un-doped $BaTiO_3$ powders with chelating agents at the heat-treated conditions was investigated by high-resolution SEM (Figure 5-18 a-c). In general, barium titanate has a relatively equiaxed shape, with particle size ranging from 80-110 nm, which increased in relation to calcination temperature, as was observed by Wei Li et al. [137].

It was also observed that the average particle size and shape of the particle was controlled by the temperature of heating treatment. In this case, non-equiaxed powders (nanorod shaped structures) can reach ~800 nm in length. On the other hand, the rod-shape structure

particles (related with cubic structure) diminish at 950 °C and disappear at 1150 °C. On the other hand, equiaxed particles consisted of the approximately spherical type of particle (~84 nm in diameter). For example, the shape of $BaTiO_3$ powders at 700 °C and 950 °C results in a combination of non-equiaxed and equiaxed morphology due to the coexistence of the tetragonal phase beside the cubic phase (the tetragonal phase is dominant at higher temperatures). The chelating agents act as a surface ligand and have the ability to control the shape and size of the growing particles. In this case, if a face of a primary nanoparticle docks against a face of another primary nanoparticle, the two crystallites will naturally be oriented at a particular angle. Meanwhile, the chelating agents absorbed on some special crystalline surfaces of the nanoparticles will modify their growth direction [119]. Therefore, the shape and size of the growing particles in the system can be modified by oriented attachment of the primary nanoparticles. Depending on the orientation, further oriented attachment will result in the formation of a rod-shaped structure. Certainly, there is a strong thermodynamic driving force for further oriented attachment because the surface energy is reduced substantially when the interface is eliminated [138].

The typical high resolution SEM micrographs and the size distribution for $BaTiO_3$:Er,Yb samples without chelating agents are shown in Figure 5-19a-c. Apparently, the $BaTiO_3$:Er,Yb synthesized without chelating agents exhibits a higher particle size than that shown for $BaTiO_3$ powders in the presence of chelating agents. It can be seen that powders display agglomerates consisting of very irregular and faceted shapes, with an average size of 137, 254, and 312 nm at 700 °C, 950 °C and 1150º C, respectively. High-resolution SEM micrographs of $BaTiO_3$:Er,Yb powders with chelating agents heat treated at 700 °C, 950 °C and 1150 ºC are shown in Figures 5-20 a-c.

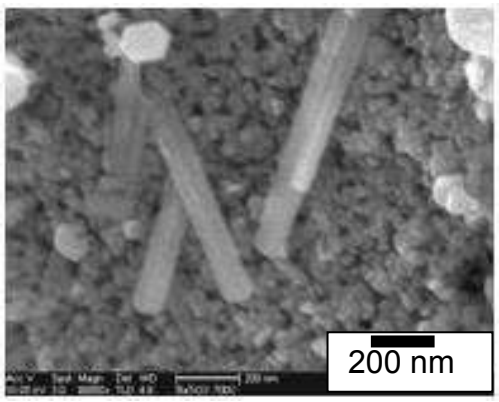

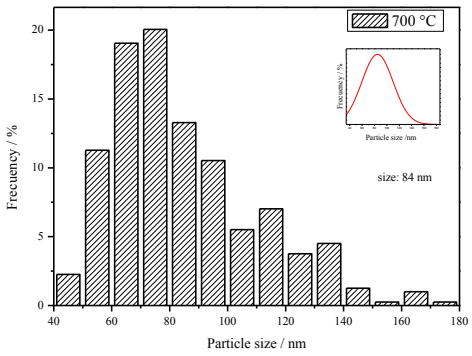

(a)

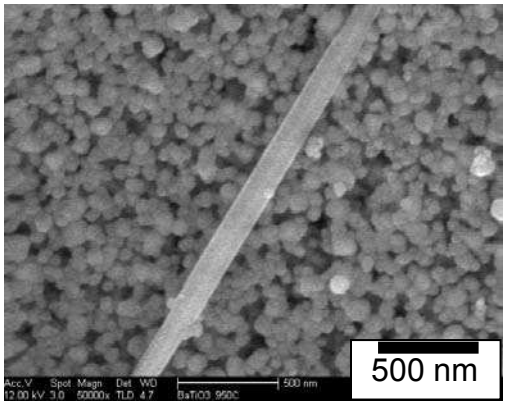

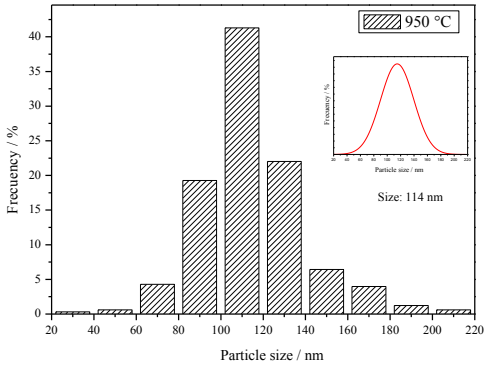

(b)

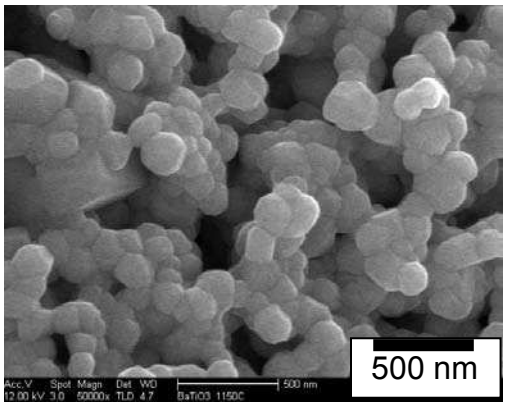

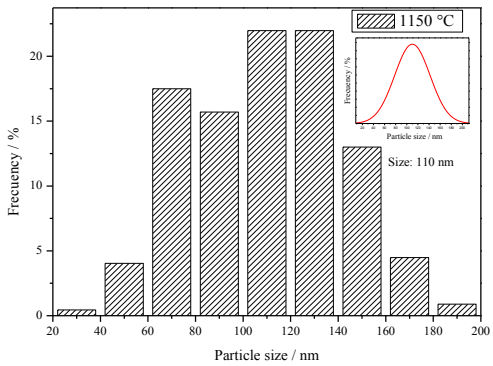

(c)

Figure 5-18. *Evolution of particle morphology of undoped $BaTiO_3$ powders with chelating agents (WCA) heat treated at 700 ºC (a), 950 ºC (b) and 1150 ºC (c).*

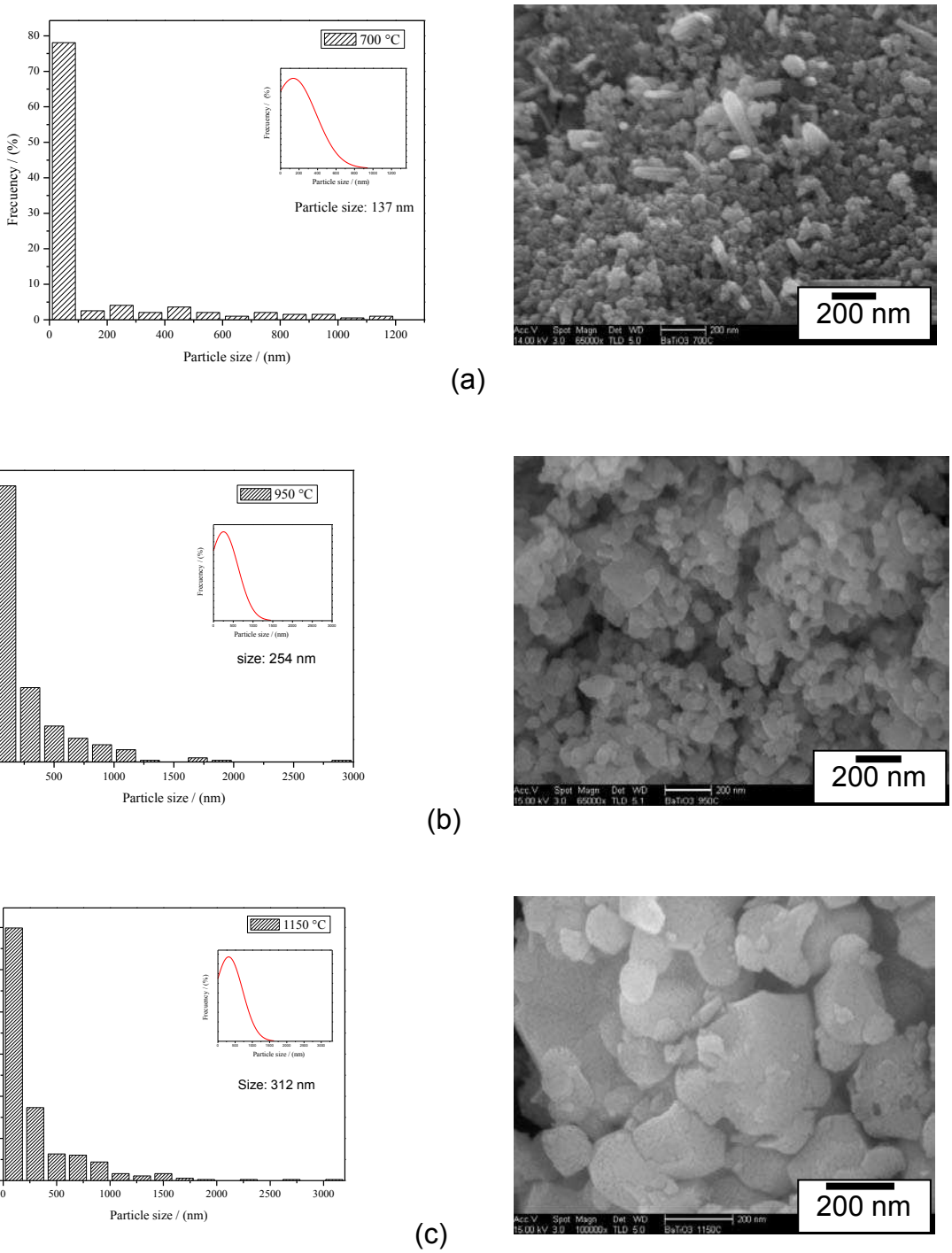

Figure 5-19. *Evolution of particle morphology of $BaTiO_3$:Er,Yb powders without chelating agents (WOCA) heat treated at 700 ºC, b) 950 ºC and c) 1150 ºC.*

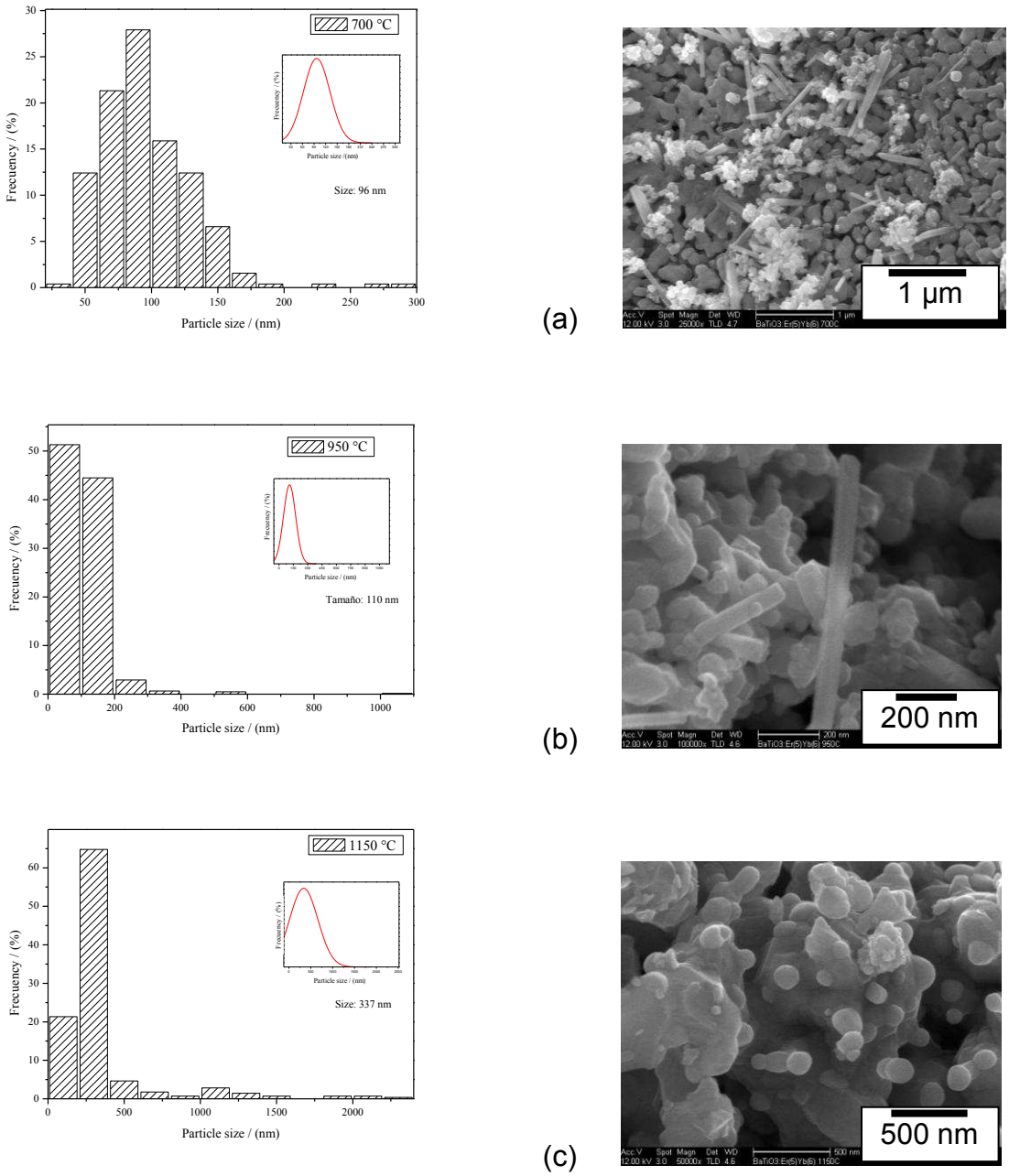

Figure 5-20. *Evolution of particle morphology of $BaTiO_3$:Er,Yb powders with chelating agents heat treated at 700 ºC (a), 950 ºC (b) and 1150 ºC (c).*

$BaTiO_3$:Er,Yb particles display a relatively equiaxed shape with a particle size ranging from 96 to 337 nm. An increase in the average particle size was observed as a function of the calcination temperature, as previously observed for un-doped $BaTiO_3$ particles.

For example, particle size for $BaTiO_3$:Er,Yb synthesized at 700 ºC was approximately 96 nm, which increased to 110 nm at 950ºC. The particle size of powders after a 950 °C heat treatment presented a small increase, as a consequence of an aggregation of small particles on the surface of bigger particles, compared with that observed at 700 °C. Finally, at 1150 ºC further coarsening of the particles occurs with the formation of aggregates (337 nm). Inside the aggregates, partial sintering has occurred, even though the morphology appears to be dominated by coarsening. Coarsening is evident in samples doped with transition metal ions [41]. This result confirms that the powders prepared by the acetylacetone/acetic acid sol-gel method are perovskite phase materials with a more spherical shape than that observed for $BaTiO_3$:Er, Yb without chelating agents. These results suggest a relationship between the morphology of the precursor gel and calcined powders. The frequency separation (Δν) determined from FTIR results obtained for the asymmetric and symmetric modes of $–COO^-$ is 138 cm^{-1} indicate a more highly chelated ligand, which leads to a lower rate of cross-linking and easier pyrolization of the Ti-C-O bonds. As a result, a finer powder can be expected. In contrast, the absence of chelated ligands reveals that the $BaTiO_3$:Er, Yb gels were relatively difficult to convert to a perovskite phase, and a bigger particle size was produced. Textural analyses results obtained for $BaTiO_3$:Er,Yb WOCA (without chelating agents) and WCA (with chelating agents) and calcined at 700, 950 and 1150 °C are presented in Table I.

Table 5-2. *Textural analyses results of $BaTiO_3$:Er, Yb powders.*

	Without chelating agents			**With chelating agents**		
Parameters	Temperature (°C)					
	700	950	1150	700	950	1150
S[a] (m^2g^{-1})	19.26	29.59	7.42	9.20	12.34	5.42
r[b] (nm)	19	16	8	10	90	54
V[c](cm^3g^{-1})	$8.9X10^{-2}$	$1.2X10^{-1}$	$1.5X10^{-2}$	$2.3X10^{-2}$	$5.6X10^{-2}$	$1.5X10^{-2}$

[a] The specific surface area was calculated using BET method.

[b] Pore radius.

[c] Pore volume measurement.

As observed from these values, the BET surface areas decrease for samples in presence of chelating agents, which can be probably attributed to the bigger pore radius than that exhibited by the samples without chelating agents size, and thus the collapse of pores in $BaTiO_3$:Er,Yb WOCA powders.

5.4.4 Microstructure of $BaTiO_3$:Er^{3+}, Yb^{3+} films

The surface morphology of the $BaTiO_3$:Er,Yb films with and without chelating agents at 700 °C, 950 °C and 1150 °C was investigated by high-resolution SEM (Figures 5-21 a-f) at two different magnifications.

The microstructures of the $BaTiO_3$:Er,Yb films in presence of chelating agents were controlled by the calcination temperatures and are presented in Figures 5-21a-c. For example, the films heat treated at 700 °C, 900 °C and 1150 °C consist of fully grown and crack-free structures. The images for the films calcined at 700 °C and 950 °C (Figures 5-21 a-b) show the surfaces are constituted by homogeneous networks. The morphology does not reveal well-formed grains, as was confirmed by AFM studies. The surface morphology revealed by the film annealed at 950 °C (Fig. 9b) is denser than the film annealed at 700°C. The particles are packed closely and well-distributed. Finally, at 1150 °C (Figure 5-21c) the film is characterized by a crack-free structure and the microstructure consists of large and irregular shaped aggregates (mean diameter 1.5 μm).

The microstructures of the $BaTiO_3$:Er,Yb films without chelating agents are presented in Figure 5-21 d-f. In general, the surface morphologies change dramatically from those observed when chelating agents were used. $BaTiO_3$:Er,Yb films heat treated at 700 °C consisted of separate, nearly monodisperse particles (Figures 5-21d).

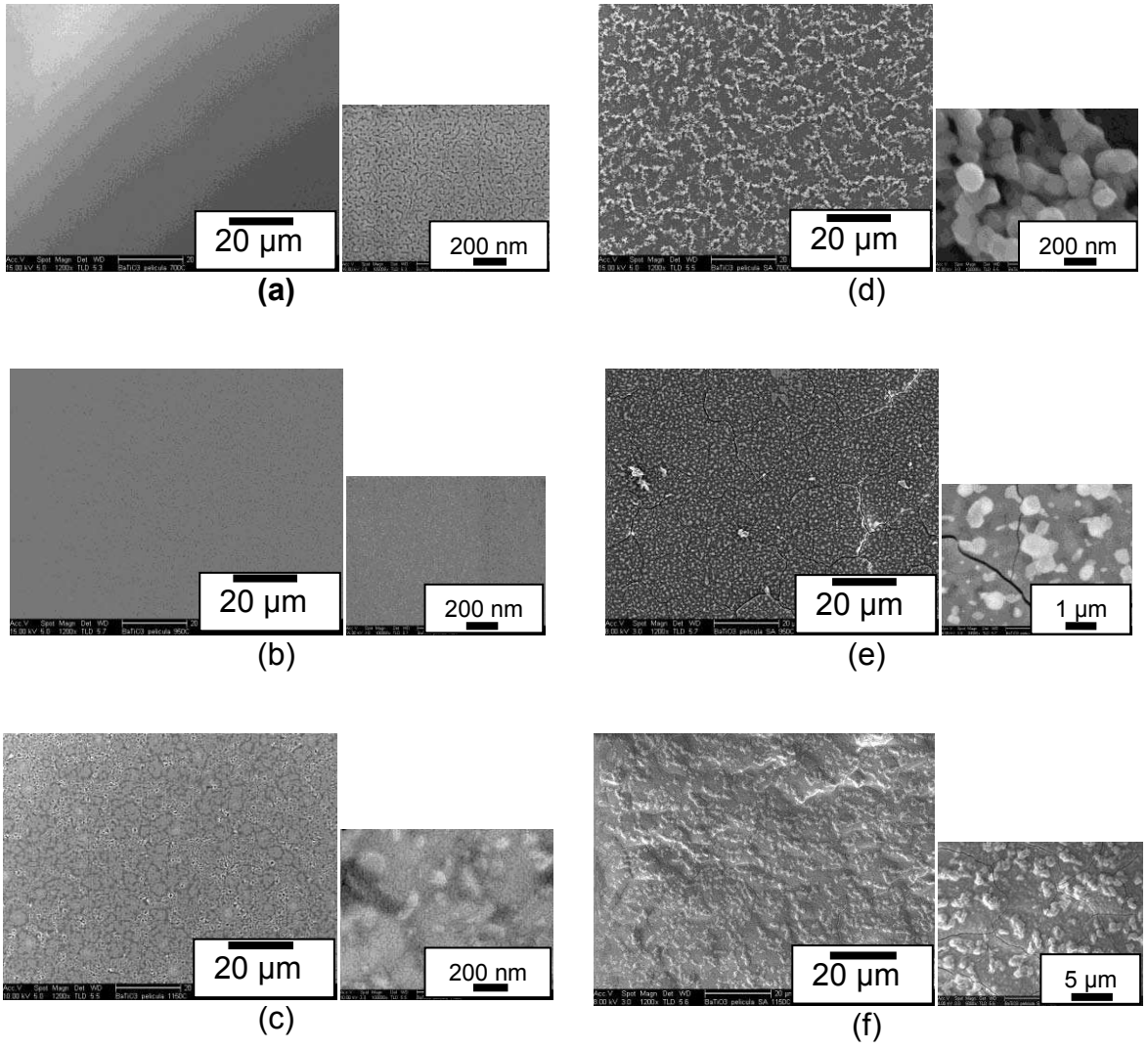

Figure 5-21. *Influence of the chelating agents (with: WCA and without: WOCA) on SEM images of $BaTiO_3$:Er,Yb films heat treated at different temperatures: WCA-700°C (a), WCA-950°C (b), WCA-1150°C (c), WOCA-700 ºC (d), WOCA-950 ºC (e), WOCA-1150 ºC (f).*

The structure is very porous, formed by granular networks, and shows poor adhesive properties toward the substrate. It can be seen that these networks present nearly spherical particles. The surface microstructure related to the film calcined at 950 °C (Figure 5-21e) had many large cracks along the reticulate parts of the film surface. The SEM images of $BaTiO_3$:Er,Yb films heat treated at 1150 °C are shown in Figure 5-21f . The films present a huge porosity, which is similar to that reported by J. Yu et al. [134]. $BaTiO_3$:Er,Yb films with chelating agents (Figure 5-21 a-c) exhibited particles uniformly distributed, in contrast

with those observed for films without chelating agents (Figure 5-21 d-f). We postulate that the uniformity of the microstructure of the films mainly involves the chemical properties of the chelating agents [139]. Regarding the role of H-(OAc) and (AcAc)H in the processes of the gel formation, H-(OAc) in the sol has the ability to strongly adjust the balance of hydrolysis and condensation speeds based on its weak acidity [88]. Moreover, (AcAc)H inhibits the process of condensation, extends the gel time, and leads to the formation of smaller gels. The presence of both (AcAc)H and H-(OAc) results in the formation of highly cross-linked, crack-free, and uniform films.

AFM studies

Roughness measurements were performed on $BaTiO_3$:Er,Yb films WCA in order to determine secondary growth effects and the quality of films. Unfortunately, layers dip-coated without chelating agents displayed a high opacity and were not analyzed by AFM. AFM topography images of the $BaTiO_3$:Er,Yb films heat treated at different temperatures are shown in Figure 5-22 a-f.

The height of the particles forming the film increases with the temperature of the thermal treatment and can be estimated directly from AFM height images (Figure 5-22 a, c, e); however the section analysis and, particularly, the particle analysis, allows more precise quantification (as is shown in Figure 5-22 b, d, f) which indicates that the mean height varies from 4.1 nm, 15.4 and 30.1 nm. In general, the surface morphologies of sol-gel films have a porous structure, and the surface has a larger fluctuation, as shown in these figures. The mean surface roughness is 7.1, 12.4 and 62.8 nm at the range of evaluated temperatures, respectively. The results in mode phase (Figure 5-22 a) also show a non-uniform chemical distribution, with two phases forming the $BaTiO_3$:Er,Yb compound; in contrast, at temperatures higher than 700 ºC (Figure 5-22 c, e), only one homogeneous phase can be observed.

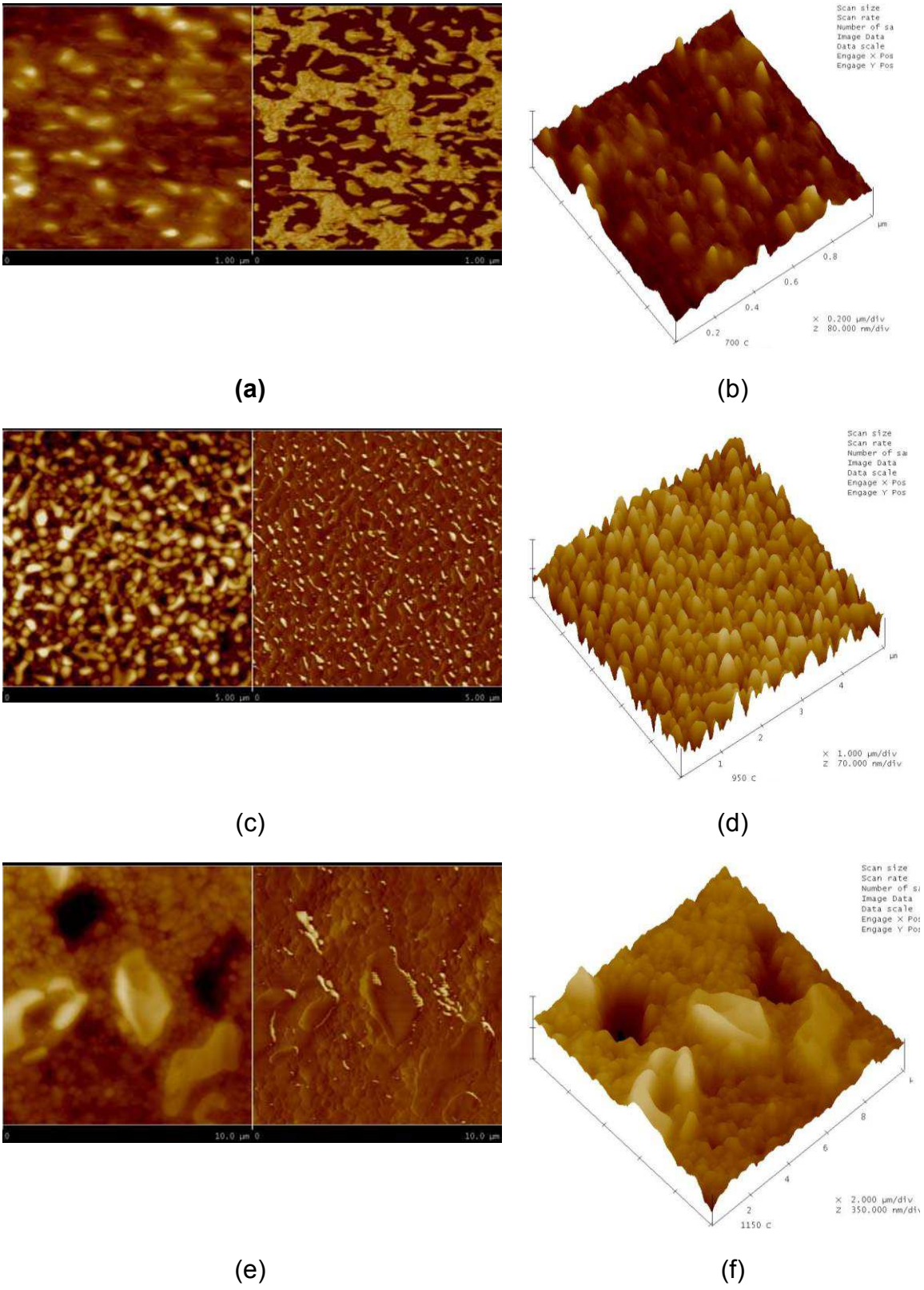

Figure 5-22. *AFM images of $BaTiO_3$:Er,Yb thin films with chelating agents heat treated at 700 ºC (a)(b), 950 ºC (c)(d) and 1150 ºC (e)(f).*

These results can be explained in terms of the internal Ti-OH bond surface, which decreased in relative intensity in the case of heat-treated samples at 950 °C and 1150 ºC, as was observed by the FTIR results. It seems to be that the shape and size of the grains are more uniform at 950 ºC than those observed at 700 ºC and 1150 ºC. This interesting observation could indicate that good control of the sintering temperature allows for good homogeneity in the morphology and composition of the $BaTiO_3$: Er, Yb compound for the preparation of films. At 1150 ºC, some islands of coarsening particles with the same composition of the matrix and an average pore size of 2.3 μm have been obtained, which corroborates the observations made by high resolution SEM.

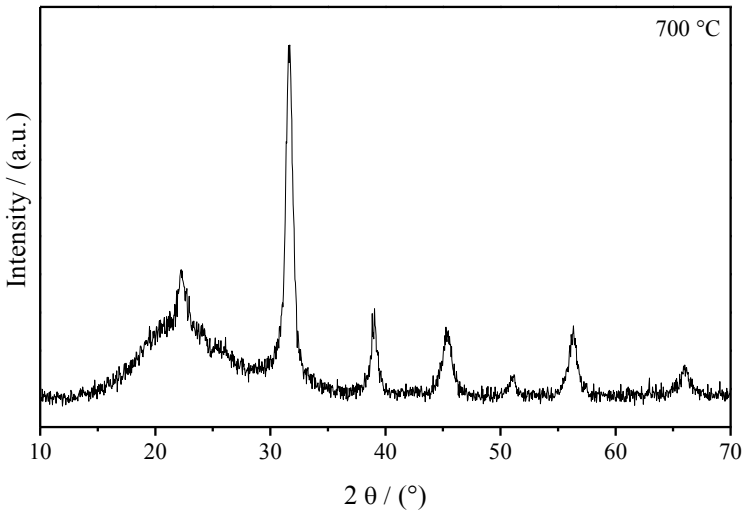

Figure 5-23. *XRD patterns of $BaTiO_3$:Er,Yb films with chelating agents heat treated at 700 ºC.*

Due to the fact that $BaTiO_3$:Er,Yb systems prepared with chelating agents were those which presented optical quality, additional measurements (XRD and thickness evaluation) were performed on it. The phase structure of erbium and ytterbium codoped barium titanate films heat treated at 700 ° C was confirmed by X-ray analysis revealing the well-crystallized structure (Figure 5-23). The thickness of the erbium and ytterbium codoped barium titanate films was measured by using m-lines spectroscopy [140,141]. The $BaTiO_3$:Er,Yb presents a thickness of 710 nm after 700 °C heat treatment.

5.5 $BaTiO_3:Eu^{3+}$ thick films

Transparent $BaTiO_3:Eu^{3+}$ films were prepared via a sol-gel method and dip-coating technique, using barium acetate, titanium butoxide, and polyvinylpyrrolidone (PVP) as modifier viscosity. $BaTiO_3:Eu^{3+}$ films ~500 nm thick, crystallized after thermal treatment at 700 ºC. The powders revealed spherical and rod shape morphology. The optical quality of films showed a predominant band at 615 nm under 250 nm excitation. A preliminary luminescent test provided the properties of the Eu^{3+} doped $BaTiO_3$.

5.5.1 DTA-TGA analyses

TG and DTA curves of the europium-doped $BaTiO_3$ powders dried at 100 °C for 24 h are presented in Figure 5-24. In the first temperature region up to 200 °C, the endothermic peak situated at 115 °C results from the evaporation of alcohol and excess water. One endothermic peak situated at ~350 °C represents the decomposition of organic compounds. The third weight loss at 700-750 °C, associated with an exothermic peak, points out the transformation of amorphous decomposition products in $BaTiO_3$.

During decomposition, there is not significant loss of titanium according to Madarász [142] for the $TiO(acac)_{1.0}$ hydroxo complexes for samples with acetylacetone content higher than 0.49. The acetylacetone anion deficiency is compensated with hydroxide ions considered products of hydrolysis (acac-Ti, + H_2O-Ti.. + acacH) according to the following reaction [143]: $M(OR)_4 + (AcAc)H \rightarrow M(OR)_3(AcAc) + R\text{-}OH$ where M represent the metal atom M and ROH the leaving group. According to the XRD results, crystallization of barium titanate starts at 700 °C Moreover, the weight loss is minimal and the weight remans unchanged afterwards.

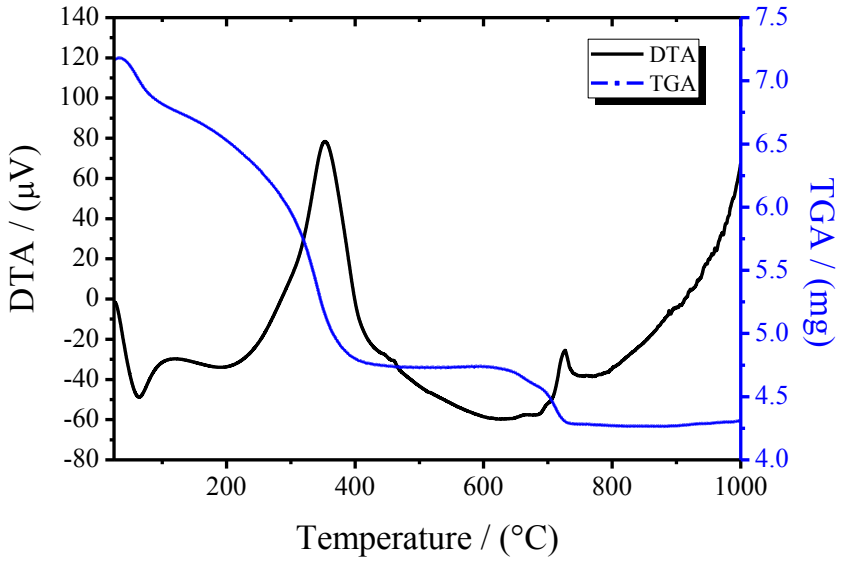

Figure 5-24. *DTA and TGA curves for $BaTiO_3$:Eu xerogel powder.*

It was stated that Ba^{2+} ions in the A site are mainly replaced by rare earth elements [144]. Eu^{3+} ions (0.098 nm) are most probably replaced Ba^{2+} (0.156 nm) cations rather than Ti^{4+} (0.065 nm). When Eu^{3+} was introduced to $BaTiO_3$, three Ba^{2+} sites were substituted by two Eu^{3+} neighbors to maintain electrical neutrality, and so one vacancy was created, then the composition expected is $Ba_{(1-0.05)}Eu_{0.05}TiO_3$, as observed by Rath [145].

5.5.2 FT-IR study

Figure 5-25 shows the FTIR spectrum of $BaTiO_3$:Eu powders, calcined at 700 °C for 2 h. The IR spectrum consisted mainly of three regions: the first region (Figure 5-25 inset) shows bands at 3,428 and 1,630 cm^{-1}, which are due to the OH stretching vibration (υ) and OH deformation vibration (δ), respectively, arising from the water and isopropanol present in the porous structure of the barium titanante xerogel.

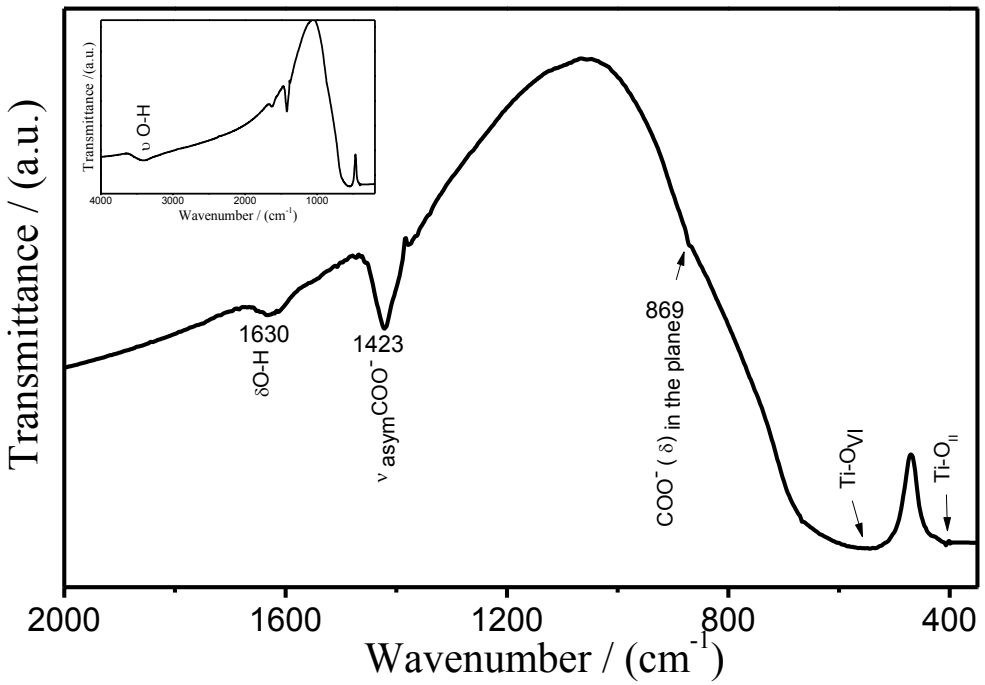

Figure 5-25. *FTIR spectrum of $BaTiO_3:Eu^{3+}$ sol-gel powder calcined at 700 °C.*

The second region corresponds to the absorption bands at 1,423 and 869 cm^{-1}, characteristic for the symmetrical vibrations and bending vibrations (in plane) of COO- groups arising from two types of ligands (the acetylacetone and acetic acid). The third region, 600 - 380 cm^{-1}, represents the characteristic infrared absorptions of the Ti-O vibrations. The band situated around 565 cm^{-1} is due to TiO_6 stretching vibration connected to the barium [41]. Finally, the peak at 414 cm^{-1} can be attributed to normal TiO_{II} bending vibrations [108].

5.5.3 Raman and X-ray diffraction analyses

Raman studies

To complete the investigations of the local structure of the sol-gel $BaTiO_3:Eu^{3+}$ derived powders (Figure 5-26a) and films (Figure 5-26b), Raman spectra were used to measure the samples annealed at 700 °C.

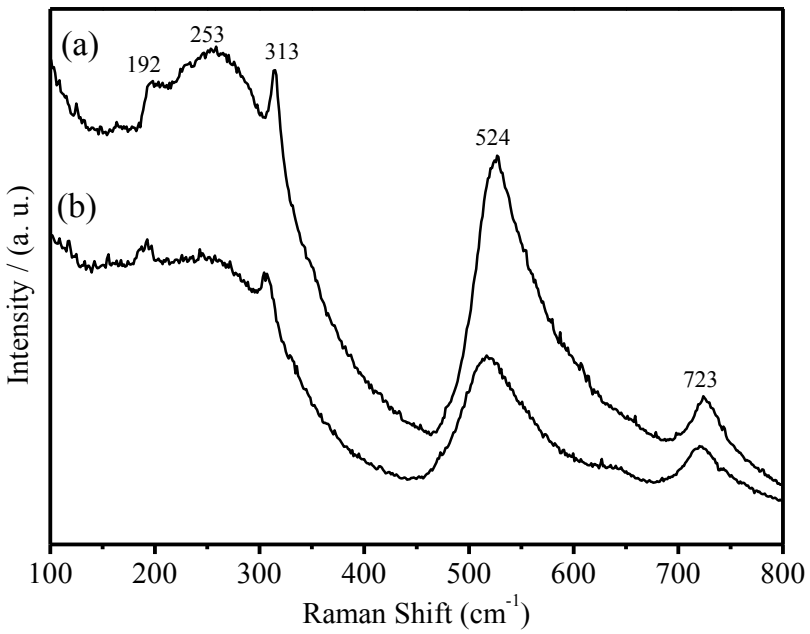

Figure 5-26. *Raman spectra of $BaTiO_3:Eu^{3+}$ powder (a) and film (b).*

Both recorded spectra contain characteristic bands: (a) one weak band [A1(TO), E(LO)] at 192 cm^{-1}, and (b) two intense broad bands A1(TO1) at ~253 cm^{-1} and A1(TO4) at 524 cm^{-1}, with sharp peaks at ~313 cm^{-1} (TO3-LO3) and for the LO4 band at ~723 cm^{-1}. The origin of the above described bands in the cubic phase has been disputed due to the presence of Raman modes in this phase, indicating that it does not have perfect cubic symmetry but has small distortions [93]. By using the Raman-active modes discussed above, it was observed that the tetragonal phase is present in both $BaTiO_3$ powder and film. However, the Raman band positions in the powder spectrum do not exactly match the peak positions in the films, which could be attributed to the internal stresses from the surface tension in the nanocrystals [146].

HT-XRD and XRD Studies

HT-XRD is used to follow *in situ* the formation of the $BaTiO_3:Eu^{3+}$ oxide from the $BaTiO_3$ precursor gel as powder and film (see Figures 5-27a and b, respectively). The first scan is the pattern for the as-synthesized xerogel at room temperature, along with the intense peaks at 2θ values of about 40, 46 and 67 (results from the Pt sample holder).

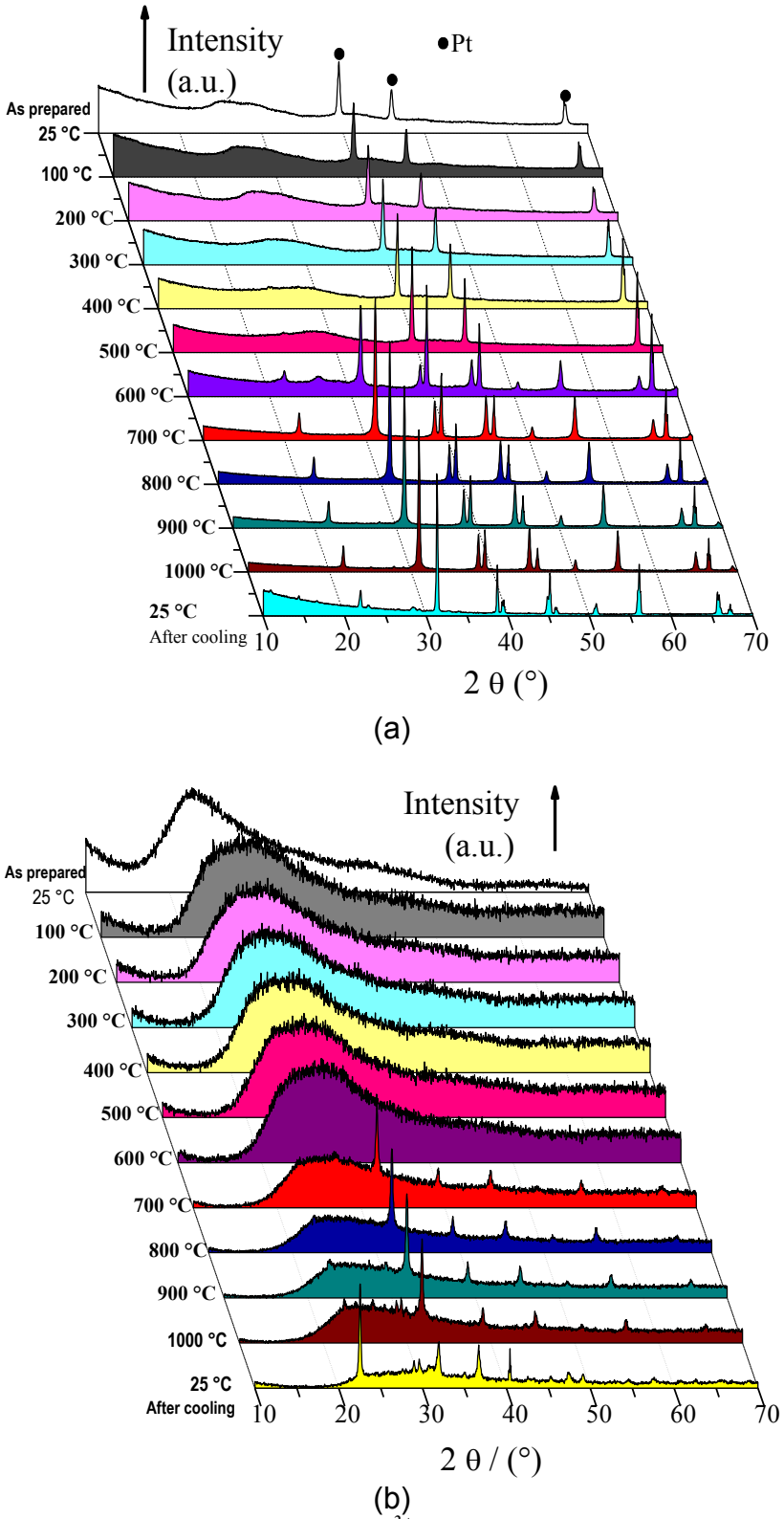

Figure 5-27. *HT-XRD patterns of $BaTiO_3$:Eu^{3+} powders (a) and films (b). Diffraction peaks related to the platinum ribbon are noted with a cross.*

In the scan corresponding to 600 °C (Figure 5-27a), it is shown that some barium carbonate is formed during the decomposition of the precursor into the $BaTiO_3$. This carbonate decomposes between 650 and 700 °C. This led to our conclusion that pure $BaTiO_3$ is fully crystallized after 2 h at 700 °C. Figure 5c shows the full XRD 2θ range of the crystallized powders, showing that two distinct peaks characterize $BaTiO_3$ tetragonal structure [147]. Additionally, *in situ* HT-XRD experiments were performed to understand the phase stability of nanocrystalline $BaTiO_3$:Eu^{3+} sol-gel films. Figure 5-28b shows the multiple plots of the barium titanate gel films scanned in air at various temperatures; from room temperature to 1000 °C, and again at room temperature after cooling.

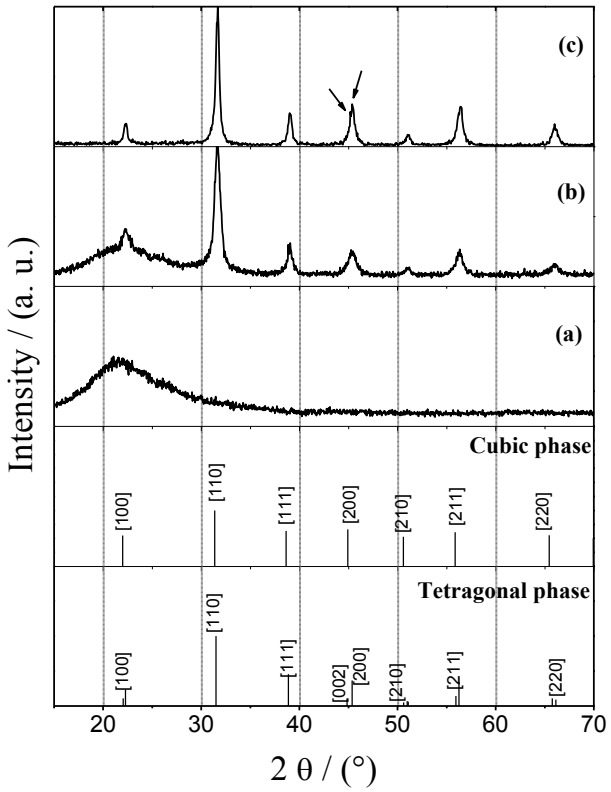

Figure 5-28. *XRD patterns of $BaTiO_3$:Eu^{3+} film calcined at 500 °C (a), 700 °C (b) and powder calcined at 700 °C (c).*

The gel film patterns indicate presence of an amorphous structure character up to 600 °C (Figure 5-28a) and the crystallization of $BaTiO_3$:Eu^{3+} after the films were heated to 700 °C

(Figure 5-27b and Figure 5-28b), in agreement with DTA analyses. The patterns of films calcined from 700 °C to 1000 °C are characterized by nanocrystalline $BaTiO_3$ samples. Due to the very broad diffraction peaks attributed to the presence of the support or to the film thickness, it is not a sensitive enough technique to easily distinguish between ferroelectric tetragonal and paraelectric pseudocubic structure (Figure 5-28b). Nevertheless, it was found that after cooling from 1000 °C to room temperature, the $BaTiO_3$:Eu^{3+} films transform from (1 1 0) orientation dominated to (1 0 0) dominated orientation, probably due to the textured densified films. The rates of cooling are mainly responsible for the high preferential orientation achieved in the $BaTiO_3$ films. The transformation of orientation has been also observed in the case of PB_xT layers films deposited on MgO (1 0 0) substrates [139].

5.5.4 Scanning electron microscopy

The morphology of $BaTiO_3$:Eu^{3+} powder and film calcined at 700 °C was investigated by SEM and is shown in Figure 5-29. The SEM images of $BaTiO_3$:Eu^{3+} powders shown in Figures 5-29a and 5-29b reveal closely-packed fine equiaxed particles, about 100 nm in size. Aditionally, non-equiaxed powders (nanorod shaped structures) reaching ~800 nm in length were observed. On the other hand, equiaxed particles consisted of the approximately spherical type. For example, the shape of $BaTiO_3$:Eu^{3+} powders at 700 °C results in a combination of non-equiaxed and equiaxed morphology due to the coexistence of the tetragonal and cubic phase. From the surface images of $BaTiO_3$:Eu^{3+} films shown in Figures 5-29c and 5-29d, the microstructures were homogeneous, continuous and crack-free.

At high magnification, as shown in Figure 5-29d, there was no evidence of cracks; however, the presence of pores can be associated with the presence of PVP. Kozuka et al. [148] have reported that when the film is heated directly at 700 °C, the decomposition of PVP and the crystallization of the film may occur concurrently.

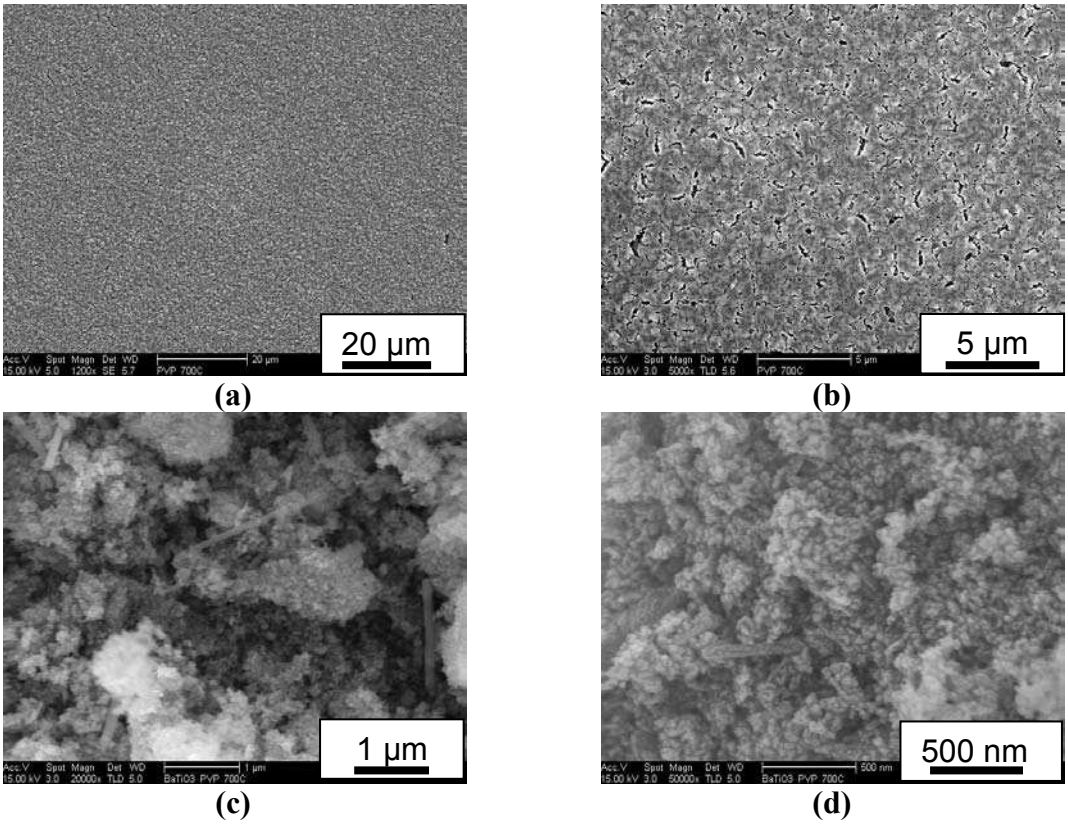

Figure 5-29. *SEM micrographs of $BaTiO_3$:Eu^{3+} of films (a), (b) and powders (c), (d) calcined at 700 °C.*

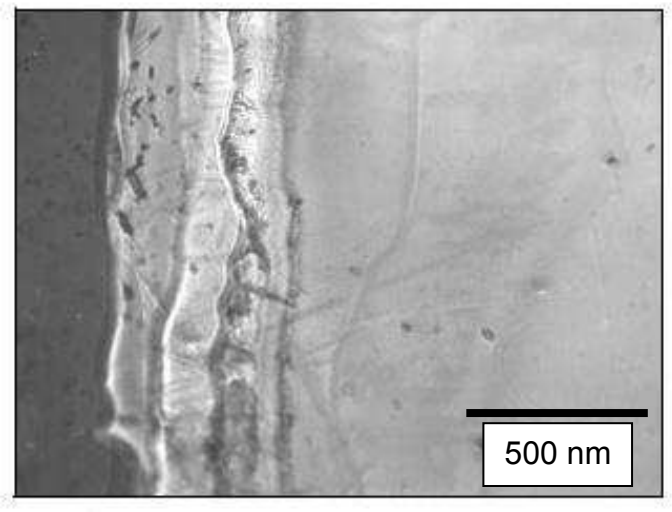

Figure 5-30. Cross section SEM micrograph of $BaTiO_3$:Eu^{3+} film calcined at 700 °C.

This can lead to crystallization with much less densification, which provides higher porosity and smaller tensile stress. Profilometry is a very common method of post-process measurement of films thickness [149]. The thickness of $BaTiO_3$:Eu^{3+} calcined at 700 °C thin film was about 500 nm is in agreement with the determined by cross section SEM, as can be observed in Figure 5-30.

5.6 $BaTiO_3$:Er^{3+} films

5.6.1 XRD studies of films with and without PVP

Figures 5-31a-d show the characteristic X-ray diffraction patterns of $BaTiO_3$:Er (0.5 % mol) films obtained with and without polyvinylpirrolidone (PVP). X-Ray difractograms of Er^{3+} doped $BaTiO_3$ film without PVP corresponding to 15, 17 and 19 layers are shown in Figs. 5-29a, 5-29b and 5-29c, respectively. The presence of diffraction peaks can be used to evaluate the structural order at long-range [150]. $BaTiO_3$:Er^{3+} phase was confirmed by comparing XRD patterns with the respective Joint Committee on Powder Diffraction Standards (JCPDS) card # 05-0626.

All the diffraction peaks are related with tetragonal structure [151]. The percentage (0.5%) in $BaTiO_3$ does not promote the transition from “tetragonal” to “cubic” phase. By increasing the number of coated layers, the optical quality of the film decreases, as is shown in Fig. 5-31c. However, the Er^{3+} doped $BaTiO_3$ single-step film showed optical quality and well-defined crystallization peaks, as shown in Fig. 5-31d. In all cases, there was no additional peak representing a second phase, as with the pyrochlore-type $RE_2Ti_2O_7$ (RE=doping ion) observed by Garcia-Murillo in ytterbium doped $BaTiO_3$ [147].

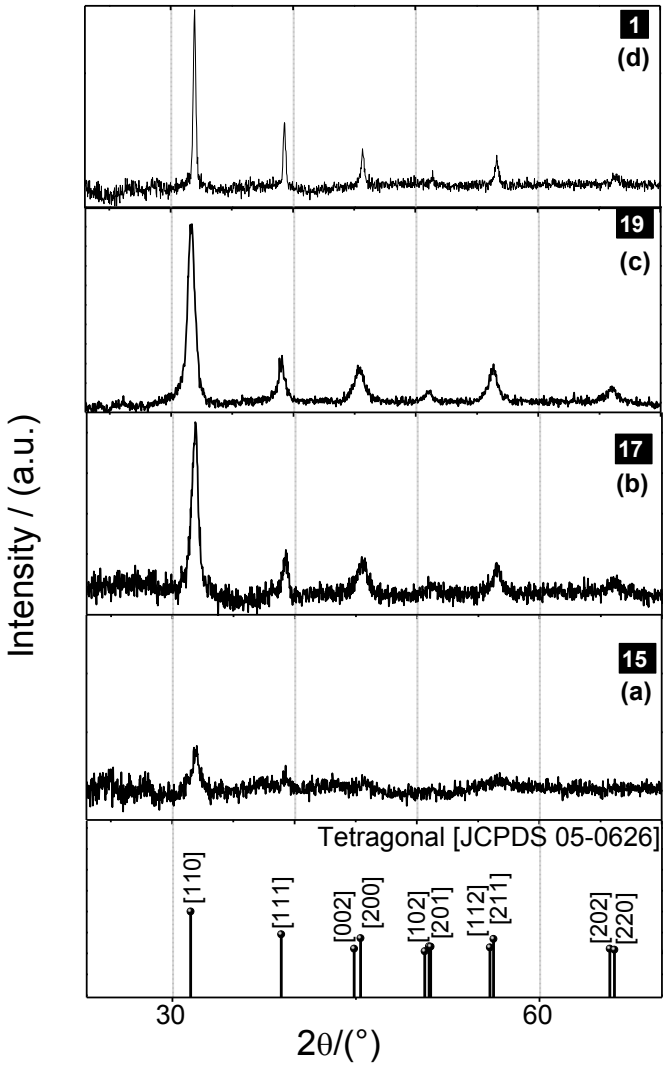

Figure 5-31. *XRD patterns of $BaTiO_3:Er^{3+}$ films with 15 (a), 17 (b), and 19 (c) layers without PVP and single step layer with PVP (d).*

5.6.2 Influence of PVP on films structure

The crystallite sizes D (nm) in films were deduced and estimated by the Debye-Scherer equation [79] from the width of the (1 1 0) diffraction peak line at 2θ = 31.8° of multilayer (17 coatings) and monolayer crystallized $BaTiO_3:Er^{3+}$ films. The crystallite sizes of the $BaTiO_3:Er^{3+}$ films were 12 and 30 nm for multilayer and single-step films, respectively.

These results revealed that when multilayered $BaTiO_3:Er^{3+}$ film was thermally treated at intermediate temperatures without PVP, the crystallite size was 12 nm, while that of the single-step $BaTiO_3:Er^{3+}$ film with PVP was 30 nm (using a continuous heating rate). Both films revealed different crystallization behaviors depending on the heating patterns. The crystallite size is larger in the single-step film with PVP, thus it is hypothesized that when the gel films are heated using a continuous heating rate from room temperature up to 700 °C, the crystallization of $BaTiO_3:Er^{3+}$ can occur after the loss of PVP and/or $[(CH_3)_2CH(CO)_2]^-$. Consequently, the organic blocking species do not hinder the growth of the crystallites, thus resulting in bigger crystallite size. The crystallization process of the gel films without PVP thermally treated at intermediate temperature (300-500, 700 °C) occurs simultaneously with the loss of organic remnants. In this situation, the organic compounds (i.e., $C_5H_8O_2$) hinder the growth of the crystallites, resulting in smaller crystallite size. Previous work has demonstrated that when PVP is incorporated in coating solutions, film thickness increases, leading to the formation of crack-free coatings [148,152-156].

It has been reported that heat treatment patterns influence the transparency of coatings; e.g., transparent $Lu_2O_3:Eu^{3+}$ waveguiding films were obtained using annealing treatments with intermediate temperatures [141]. In the present study, the determination of film thickness was performed by m-lines spectroscopy [157] due to the films' waveguide properties. This method requires the production of high quality thin films; i.e., films that are crack-free, transparent and with as few defects as possible, so as to support low-loss light propagation. Optical quality film is obtained by ensuring uniform wetting and good film adhesion onto the substrate via the formation of –OH groups on the cleaned substrate surface [158]. In the present study, one- and seventeen-layer $BaTiO_3:Er^{3+}$ films, with and without PVP, respectively, were necessary to obtain at least 2 transverse electric (TE) modes and two transverse magnetic (TM) modes to perform thickness evaluation according to m-lines spectroscopy [159]. For single and multilayer coatings, the measured thicknesseses of $BaTiO_3:Er^{3+}$ calcined with different heating patterns were 828 and 510 nm, respectively. The differences in thickness of 1 and 17 stacked layers of erbium doped barium titanate are related with the presence of PVP, which allows an important increase in thickness. Due to

this feature, the addition of PVP to elaborate $BaTiO_3$ films, has been extensively studied (Table 5-3).

Table 5-3. *Studies related with the synthesis of $BaTiO_3$ thick films.*

System	Starting materials/ Chelating agents	PVP (FW)	Mole Ratio	Tech-nique	Coa-ting #	Thick-ness / µm	Com-ments	Ref.
$BaTiO_3$	$Ba(CH_3COO)_2$ $Ti(OPr^i)_4$ / H-(OAc)	630000	PVP/Ti=1	Dip coating	1	1.2	Structural and morphological studies	[148]
$BaTiO_3$	$Ba(CH_3COO)_2$ $Ti(OC_2H_5)_4$ / H-(OAc)	630000	PVP/Ti=1	Spin coating	1	0.56	Dielectric properties	[160]
$BaTiO_3$: Er^{3+}	**$Ba(C_5H_7O_2)_2$ $Ti(OPr^i)_4$ / H-(OAc) (acac)H**	**-**	**-**	**Dip coating**	**17**	**0.5**	**Luminescent properties**	**This work**
		1300000	**Ba/PVP=0 .25**		**1**	**0.82**		
$BaTiO_3$	Metallic Ba $Ti(OC_2H_5)_4$ (reflux method)	360000	Ba/PVP =0–85 wt%	Spin coating	-	1	Dielectric properties	[161]
$BaTiO_3$	$Ba(CH_3COO)_2$ $Ti(OPr^i)_4$	630000	Ba/PVP =0.6	Dip coating	1	1.2	Structural and morphological studies	[148]
$BaTiO_3$	$Ba(CH_3COO)_2$ $Ti(OPr^i)_4$/ H-(OAc)	630000	Ba/PVP =0.6	Dip coating	1	0.9	Dielectric properties	[162]

As can be observed in Table 5-3, previous studies are related with the synthesis of non-doped $BaTiO_3$; moreover, the synthesis of $BaTiO_3$ in those studies was based on the use of $Ba(CH_3COO)_2$ as a precursor. The maximum thickness without cracks was 1.2 µm at

PVP/Ti(or Ba) molar ratios ranging from 0.6 to 1.0 [152]. This behavior can explained as follows: PVP can be hybridized with metalloxane polymers, and this hybridization inhibits stress-induced film cracking due to structural relaxation occurring when the gel films are fired [153, 163]. The most important difference between our results and the results of other studies is the preparation of $BaTiO_3$:Er^{3+} in presence of PVP for the first time, using $Ba(C_5H_7O_2)_2$ as a barium precursor, with a molar ratio Ba/PVP=0.25. In this case, the crack-free film (820 nm thick) was achieved with a single-step process. Figure 5-32 shows the cross-section SEM micrograph appearance of the $BaTiO_3$:Er^{3+} films with PVP thermally treated at 700 °C for 10 min.

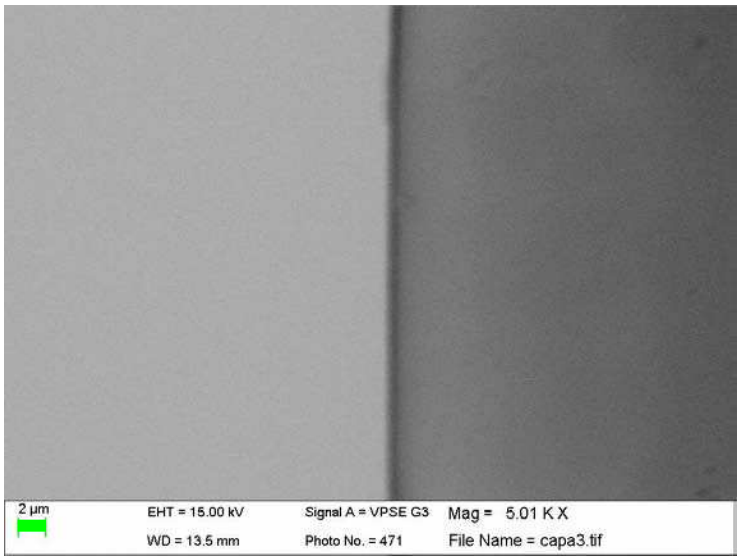

Figure 5-32. *Cross-section SEM micrograph of $BaTiO_3$:Er^{3+} films with PVP.*

The film thickness was found to be about 0.8 µm, in agreement with that determined using m-lines spectroscopy. The obtained thickness was effectively lower than that observed by other authors [152,153]. In this situation, the strategy to increase the thickness of films is to use a higher content and/or higher-molecular-weight of PVP/Ti (or Ba), incorporated into the *sol* in order to achieve an increased *sol* reaction time. It must be noted that an excess amount of PVP is harmful; it leads to crack formation [164] and films become opalescent [152] or non-transparent [165]. The microstructure and optical transmission depends on the PVP content; the experimental conditions for $BaTiO_3$:Er^{3+} single-step film discussed here result in dense, crack-free and transparent films. Multilayer films showed lower thickness;

however, the optical quality was maintained in spite of more rapid structural relaxation than that exhibited by a single $BaTiO_3$:Er^{3+} layer. These optical features were taken into account for film thickness and optical evaluation.

5.6.3 Microstructure of $BaTiO_3$:Er^{3+} films

The surface morphology of the Er^{3+} doped $BaTiO_3$ (both 17 and 1 layers) was investigated by high-resolution SEM, as shown in Figs. 5-31b-d. The top view of FE-SEM micrographs for crystalline Er^{3+} (0.5 %mol) doped $BaTiO_3$ films without PVP (Figures 5-33 a-c) showed a greater surface smoothness than that observed for PVP films (Figures 5-33d); 1, 15 and 17 layer films were transparent and crack-free. Nevertheless, films without and with PVP (Figures 5-33 b and d, respectively) are composed of crystallites with nanometric grain size; the grain size is in agreement with XRD results. The particle grain size (~12 nm) provokes the stabilization of the cubic phase and blocks the formation a tetragonal structure [109]. Similar morphology for $BaTiO_3$ sol-gel thin films has been reported by Lee et. al. [1]. This morphology results in a homogeneous and uniform surface, which can be attributed to a higher volatilization rate (when the films were thermally treated at intermediate temperatures) of the organic materials than that observed for gel films with PVP. SEM images (Figures 5-33d) of film with PVP show significant qualitative differences between films grown without PVP. This film showed entangled flower-like grains with diameters ranging from 0.8–1.2 μm and with variable lengths. They contain particles around 100 nm in size constituted by the agglomeration of nanocrystallites. The flower-like morphology is apparently caused by crystal twinning at the onset of growth, and their shape and size are related with the Ba/PVP=0.25 molar ratio and by [$Ba(C_5H_7O_2)_2$]; this is contrary to the film morphology derived from the use of barium acetate [$Ba(CH_3COO)_2$][152]. These films also exhibit homogeneity and transparence on the surface, attributed to strong hydrogen bonding interactions between C=O groups of PVP and the OH groups of the metalloxane Ti-O polymers from $BaTiO_3$. Such C=O groups can be regarded as the capping agent for the OH groups of the metalloxane polymers (Fig. 5-34); they suppress the condensation reaction and promote structural relaxation.

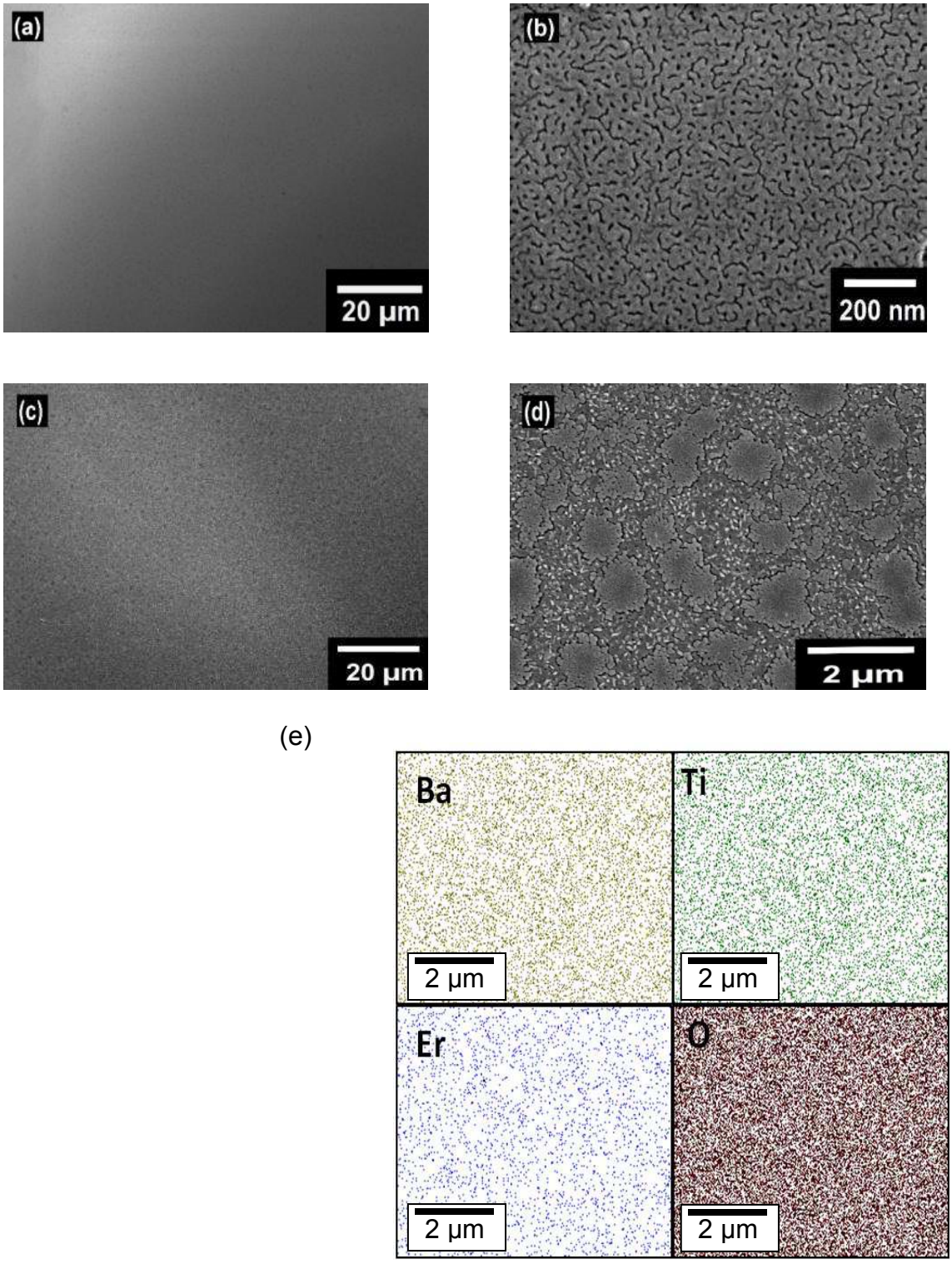

Figure 5-33. *SEM micrographs of $BaTiO_3:Er^{3+}$ films without (a)(b) and with (c)(d) PVP and EDS mapping images of $BaTiO_3:Er^{3+}$ films with PVP (e).*

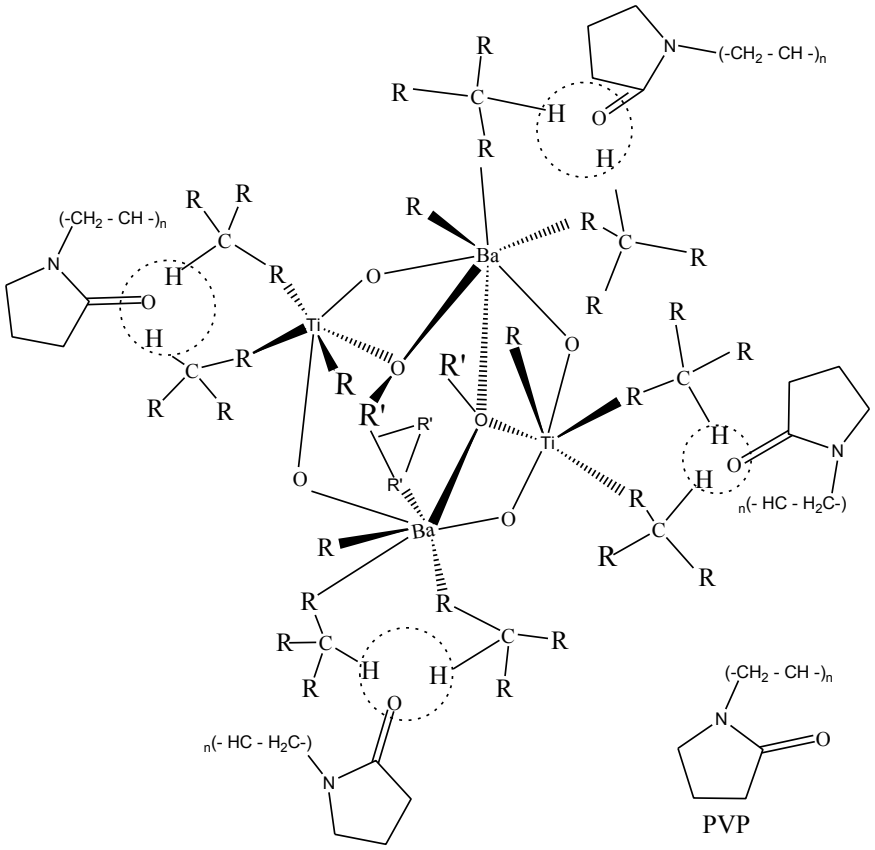

Figure 5-34. *Structure of intermediate alkoxide complexes of barium and titanium in presence of PVP.*

The $BaTiO_3:Er^{3+}$ films were dispersed well in the PVP matrix and demonstrated no aggregation or phase separation, as was confirmed previously by XRD studies. Because the efficiency of the up-conversion process depends on the spatial distribution of the dopant ions [167], EDS mapping images were obtained on the film with PVP. Figure 5-33e shows the bright colors which represent Ba, Ti, O and Er elements, respectively. The films with PVP (single-step) revealed the high homogeneity of element distribution in $BaTiO_3:Er^{3+}$.

Chapter 6. Luminescent properties

6.1 Luminescent properties of $BaTiO_3:Yb^{3+}$ powders

The absorption spectra of $BaTiO_3$ doped 2, 4 and 8 mol% Yb^{3+} powders annealed at 1200 °C is shown in Figure 6-1; the absorption spectrum of $BaTiO_3:Yb^{3+}$ 4 mol % heat-treated at 700 °C is also shown for comparison. The broad absorption band between 900 and 950 nm (splitting of the multiplet $^2F_{5/2}$) on the $BaTiO_3$ crystallized in cubic phase (700 °C) changed to a single band situated around 900 nm in the powder heat-treated at 1200 °C. This absorption of Yb^{3+} is similar to that observed in many other Yb^{3+} doped crystals and is related to the electronic transitions $^2F_{5/2} \rightarrow {}^2F_{7/2}$ within 4f electronic shell of Yb^{3+} ions. Notice that in Figure 6-1 the absorption intensity increases with the doping concentration.

The fluorescence spectra of $BaTiO_3:Yb^{3+}$ (2, 4, and 8 mol%) powders heat-treated at 1200 °C after 940 nm excitation are presented in Figure 6-2. This figure also shows the emission spectrum of the $BaTiO_3:Yb^{3+}$ (4 mol%) annealed at 700 °C. The emission spectrum of the cubic barium titanate gel powder (700 °C) shows an emission peak at 980 nm; nevertheless, when the structure is heat-treated at 1200 °C (presence of the tetragonal phase), the emission spectra consists of a broad band from 970 to 1010 nm, with a maximum at 980 nm corresponding respectively to the $^2F_{5/2} \rightarrow {}^2F_{7/2}$ transitions (5→1). Changes in emission spectra due to the Yb^{3+} ions concentration are shown in Figure 6-2.

In Figure 6-3 are presented the emission spectra of the $BaTiO_3:Yb^{3+}$ (4, 6 y 8 mol%) powders heat treated at 700 °C. In this figure it is observed that the powder with

concentration of 6 mol% of Yb is the most intense. At high concentration values occurs a quenching in the luminescent effect.

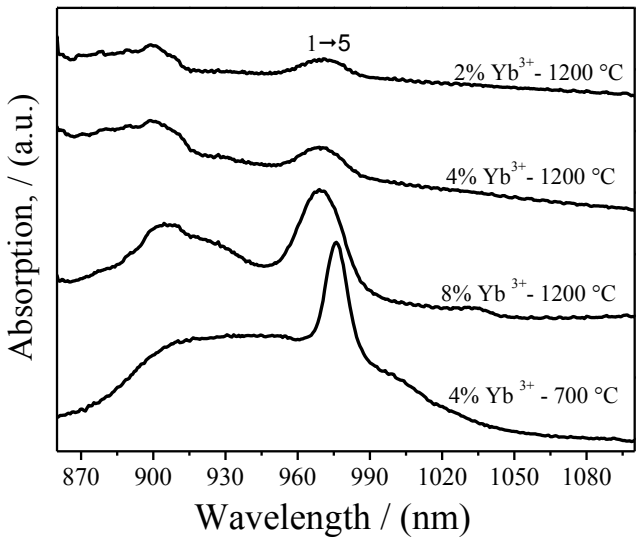

Figure 6-1. *Absorption spectra of $BaTiO_3$:Yb^{3+} powders.*

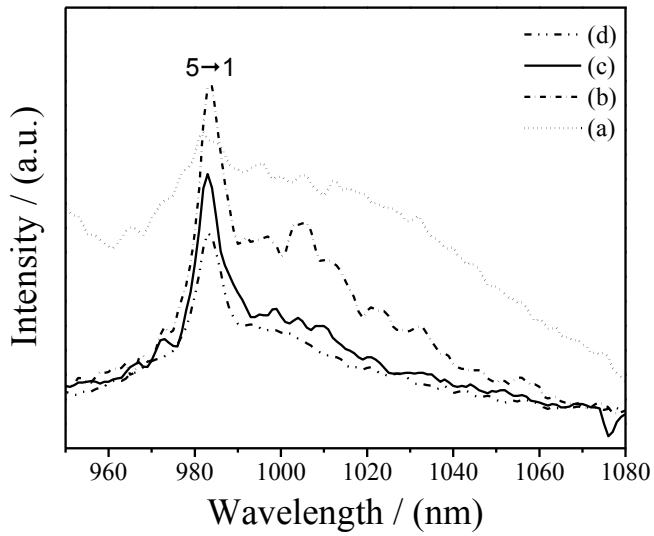

Figure 6-2 *Emission spectra of 2, 4 and 8 mol% Yb^{3+} doped $BaTiO_3$ powders heat treated at 1200 °C and 4 mol% heat treated at 700 °C.*

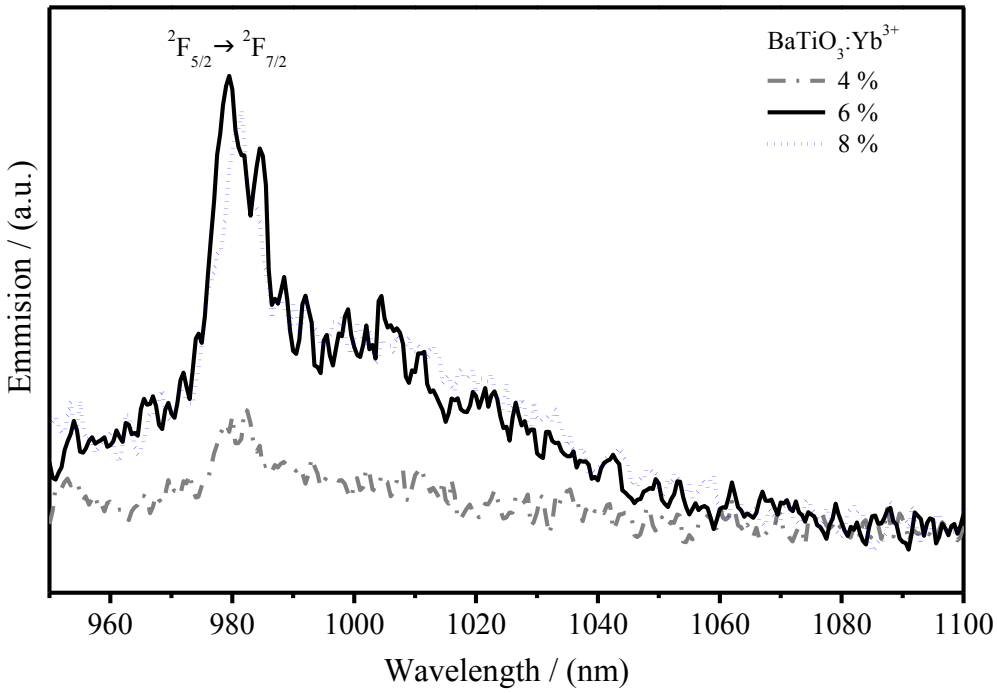

Figure 6-3. Emission spectra of *$BaTiO_3:Yb^{3+}$ (4, 6 y 8 mol%)* powders heat treated at 700 °C.

From this results were prepared codoped $BaTiO_3$:Er, Yb system taking into account that the best emission intensity obtained was 6 % mol. In the same form, films were prepared using these results.

4.1 Luminescent properties of $BaTiO_3:Er^{3+},Yb^{3+}$ powders

$BaTiO_3$:Er,Yb powders heat treated at 700 °C were chosen to analyze luminescent properties for the concentrations presented in the Table 6-1. The sample were excited at wavelength of 485, 520, 970, 940 y 800 nm, all the measurement were performed at room temperature.

Table 6-1. *Concentrations of doped and codoped $BaTiO_3$ sample studied by absorption and emission spectroscopies.*

$BaTiO_3$	
Doping ion concentrations / % molar	
Er	**Yb**
2.5	**-**
5.0	**-**
10.0	
-	**2.0**
-	**4.0**
-	**6.0**
2.5	**6.0**
5.0	**6.0**
10.0	**6.0**

Single erbium doped samples showed the characteristic bands associated with trivalent erbium spectrum in the 450–1600 nm region, while co-doped samples showed the same Er^{3+} absorption bands, but the band at about 1.0 lm is modified by the presence of Yb^{3+} ions, as expected, (Figure 6-4 and 6-5), shows the absorption spectra for samples with 10.0 mol% of Er^{3+} and 6.0 mol% of Yb^{3+}. That is, in this region the band was broadened due to the addition of those ions. According to the absorption spectrum, we pumped at four wavelengths to study the fluorescence, up-conversion and energy transfer processes, i.e. at 485, 970, 940 and 800 nm with the tuneable pulsed laser system.

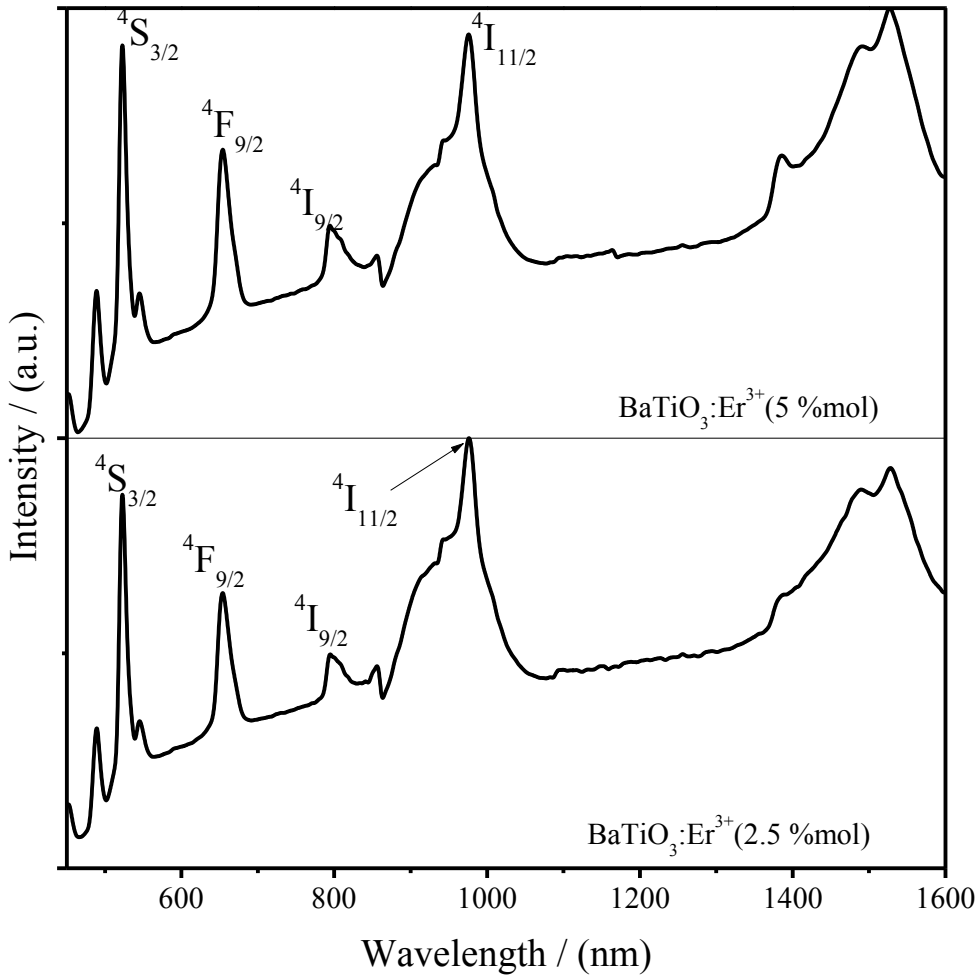

Figure 6-4. *Absorption spectra of the $BaTiO_3:Er^{3+}$ powders heat treated at 700 °C.*

6.2.1 Excitation at 485 and 520 nm

a) Doped sample.

When pumping at 485nm the $^4F_{7/2}$ state of erbium is populated. We found that the emission spectra from this state were similar to the recorded when the $^2H_{11/2}$ state was pumped directly at 520 nm.

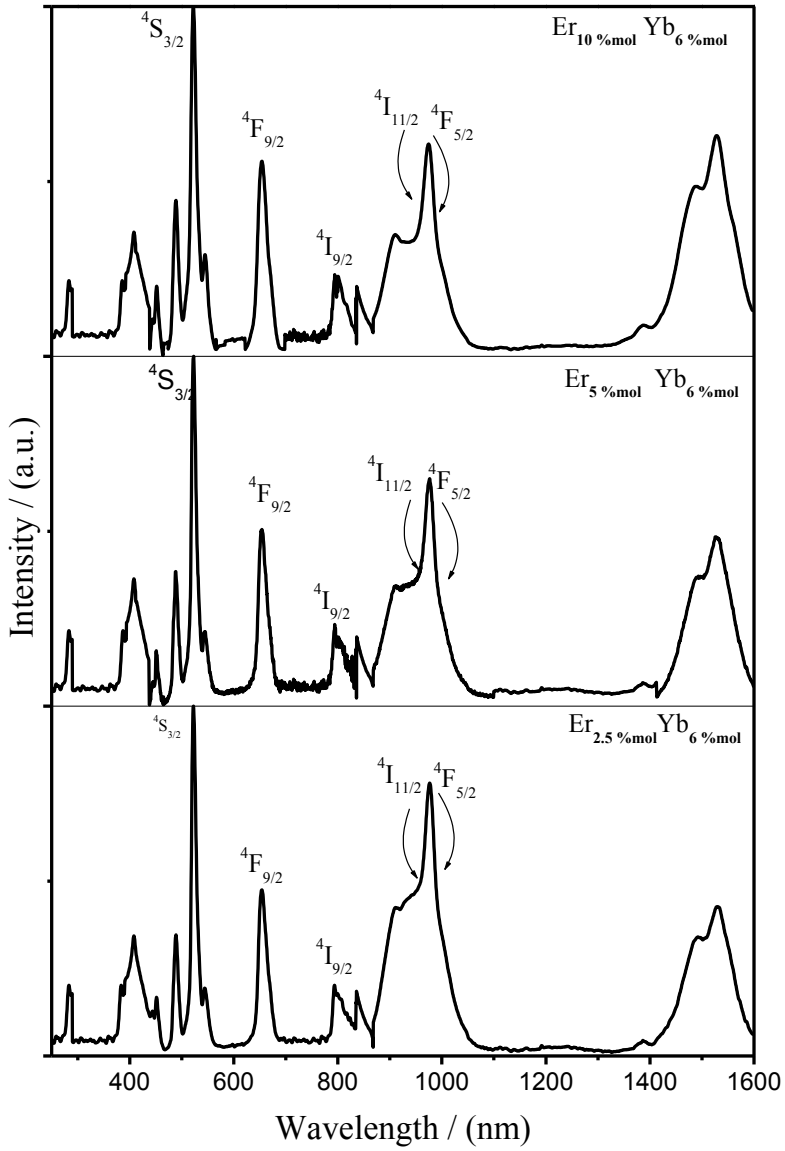

Figure 6-5. *Absorption spectra of $BaTiO_3$:Er^{3+},Yb^{3+} powders heat treated at 700 °C.*

Thus, it can be assumed that from the $^4F_{7/2}$ state of erbium a fast non-radiative decay occurs to the $^2H_{11/2}$ and $^4S_{3/2}$ states, which are thermally coupled. The visible emissions of erbium single doped and erbium-ytterbium codoped $BaTiO_3$ samples are shown in Figure 6-6 when pumped at 520 nm. The five spectra in this figure correspond to $BaTiO_3$:Er^{3+} (2.5 and 5 mol%) and $BaTiO_3$: Er^{3+} (2.5, 5 y 10 mol%), Yb^{3+}(6 mol%).

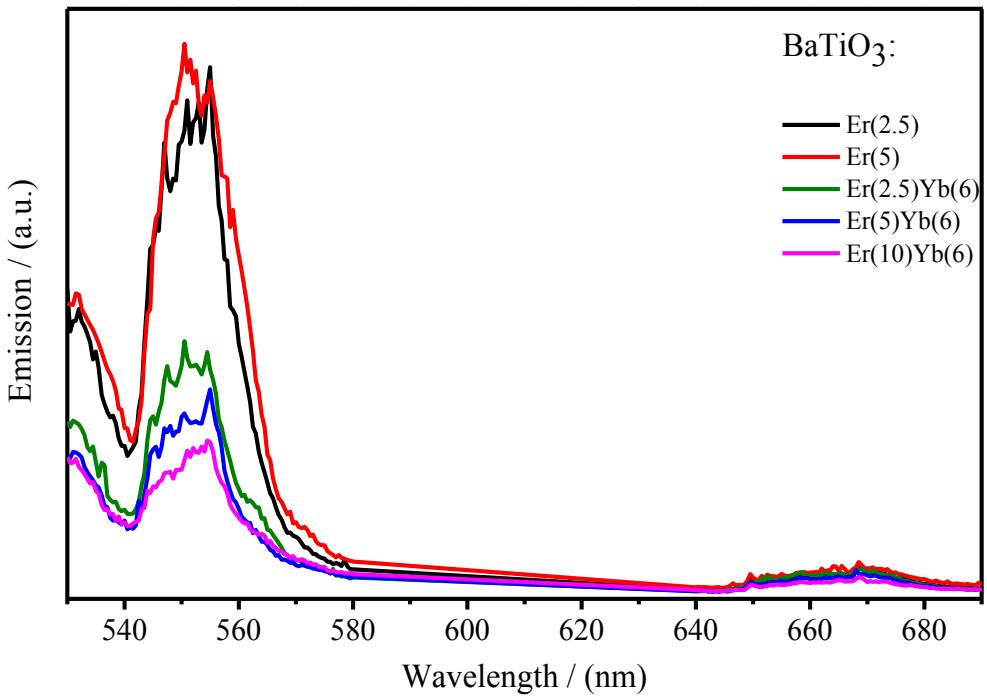

Figure 6-6. *Emission spectra of $BaTiO_3$:Er^{3+},Yb^{3+} powders heat treated at 700 °C, λ_{exc}=520 nm.*

The two former bands are ascribed to the $^2H_{11/2}$, $^4S_{3/2}\rightarrow{}^4I_{15/2}$ Erbium transitions and the later band to $^4F_{9/2}\rightarrow{}^4I_{15/2}$. Figure 6-6 shows that the peak intensity of the green band is different for the single and codoped samples, the former have higher peak intensity than the codoped samples. The single doped spectra in the green region in Figure 6-6 have similar peak intensities even when the erbium concentration was doubled. This is a concentration quenching process. Stronger quenching of the luminescence in the spectra shown in Figure 6-6 can be observed in codoped samples and it is due to the presence of ytterbium ions. Furthermore, the peak intensity for these three spectra diminishes as the erbium concentration increases. In contrast, Figure 6-6 also shows that the peak intensities of the red band do not change for any of these cases. That is, for the single doped and codoped samples the peak intensity of the red band look unchanged no matter if the erbium concentration is increased.

To understand the concentration quenching for the green band of the single doped samples in this figure, one might consider a cross-relaxation process of the type $^4S_{3/2}+^4I_{15/2}\rightarrow{}^4I_{9/2}+^4I_{13/2}$; see Figure 6-7 for all transitions considered for this discussion. This process depends on the erbium concentration as shown below. As the erbium concentration increases the $^2H_{11/2}$ and $^4S_{3/2}$ states populate and then emit, but their green emission diminishes as the erbium concentration increases. Due to the cross relaxation mechanism the $^4I_{9/2}$ populates and a fast non-radiative decay occurs down to the $^4I_{11/2}$; at the same time the $^4I_{13/2}$ state of Erbium gets populated. When the $^4I_{11/2}$ state populates, it might non-radiatively decay to the lower $^4I_{13/2}$ and/or emit at about 974 nm.

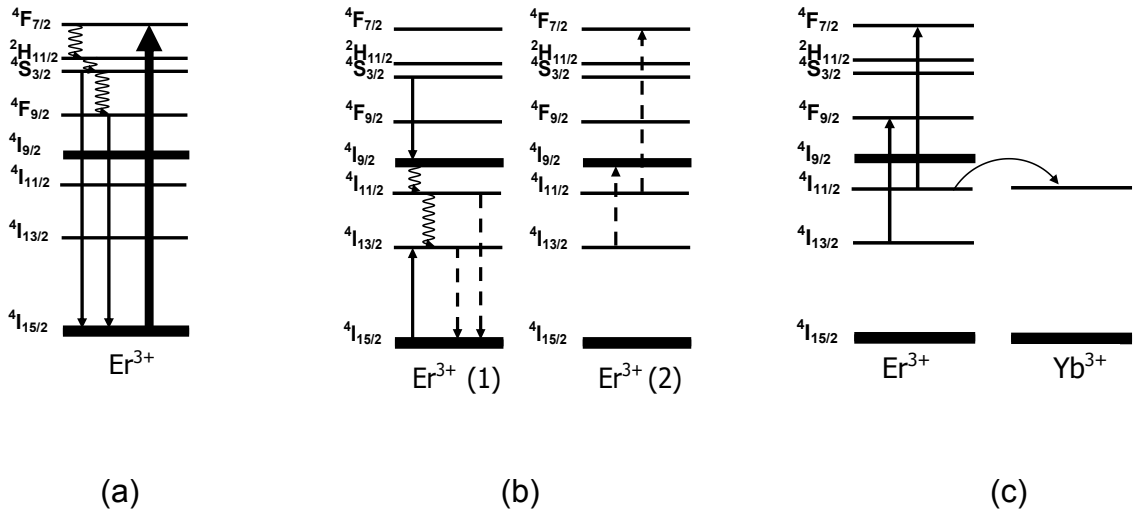

Figure 6-7. *Energy level diagram showing the most relevant transitions of $BaTiO_3:Er^{3+}$ y $BaTiO_3:Er^{3+},Yb^{3+}$ powders heat treated at 700 °C. Red and green emission (a), Schematic of cross-relaxation mechanisms and energy transfer process between erbium ions (b), energy transfer process between erbium and ytterbium ions (c).*

Figure 6-8 shows the emission of the single (with a peak intensity at about 972 nm) and co-doped (with a peak intensity at about 981 nm) samples in the 940-1030 nm region. This figure clearly shows that for the single doped samples the higher peak intensity corresponds to the $BaTiO_3$:Er(5%mol) sample. That is, the emission from the $^4I_{11/2}$ is strong and increases as the dopant concentration increases. Similarly, due to the assumed cross relaxation the $^4I_{15/2}\rightarrow{}^4I_{13/2}$ transition populates the $^4I_{13/2}$ state and emits at about 1500 nm.

Figure 6-9 shows the emission in the 1425-1700 nm region for single and double doped samples. The peak intensity for the single doped erbium with higher concentration is higher. Therefore, we have proved that the assumed cross mechanism that quenches the green emission depends on the erbium concentration and the emission of the $^4I_{11/2}$ and $^4I_{13/2}$ energy levels increase as the erbium concentration increases.

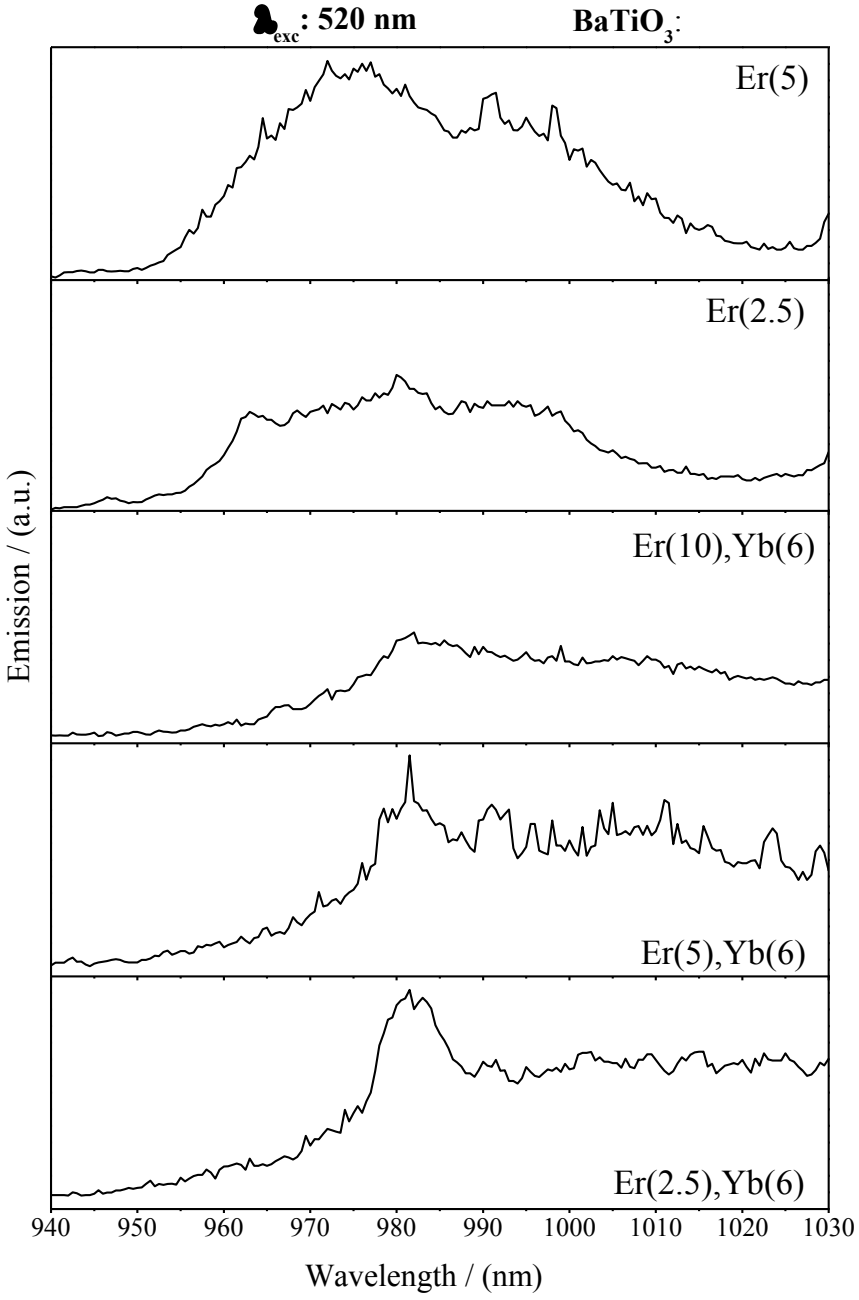

Figure 6-8. *Emission spectra of $BaTiO_3:Er^{3+}$ and $BaTiO_3:Er^{3+},Yb^{3+}$ powders.*

If we now look the emission in the 1.5mm region for codoped samples in Figure 6-9, the peak emission for the $BaTiO_3:Er^{3+}(2.5),Yb^{3+}(6)$ sample is higher when compared to the other peaks of the other two codoped samples. This behaviour is in contrast to the single doped samples where the reverse behaviour is observed. We can explain this behaviour based on our previous results for single doped samples and the presence of Ytterbium ions. That is, the $^4I_{13/2}$ state is mainly populated by the assumed cross relaxation mechanism through the transition $^4I_{15/2} \rightarrow {}^4I_{13/2}$; nevertheless one additional channel contributes to populate such state and as we will see its contribution cannot be neglected. The $^4I_{13/2}$ state is also populated through a fast relaxation from the $^4I_{11/2}$ state.

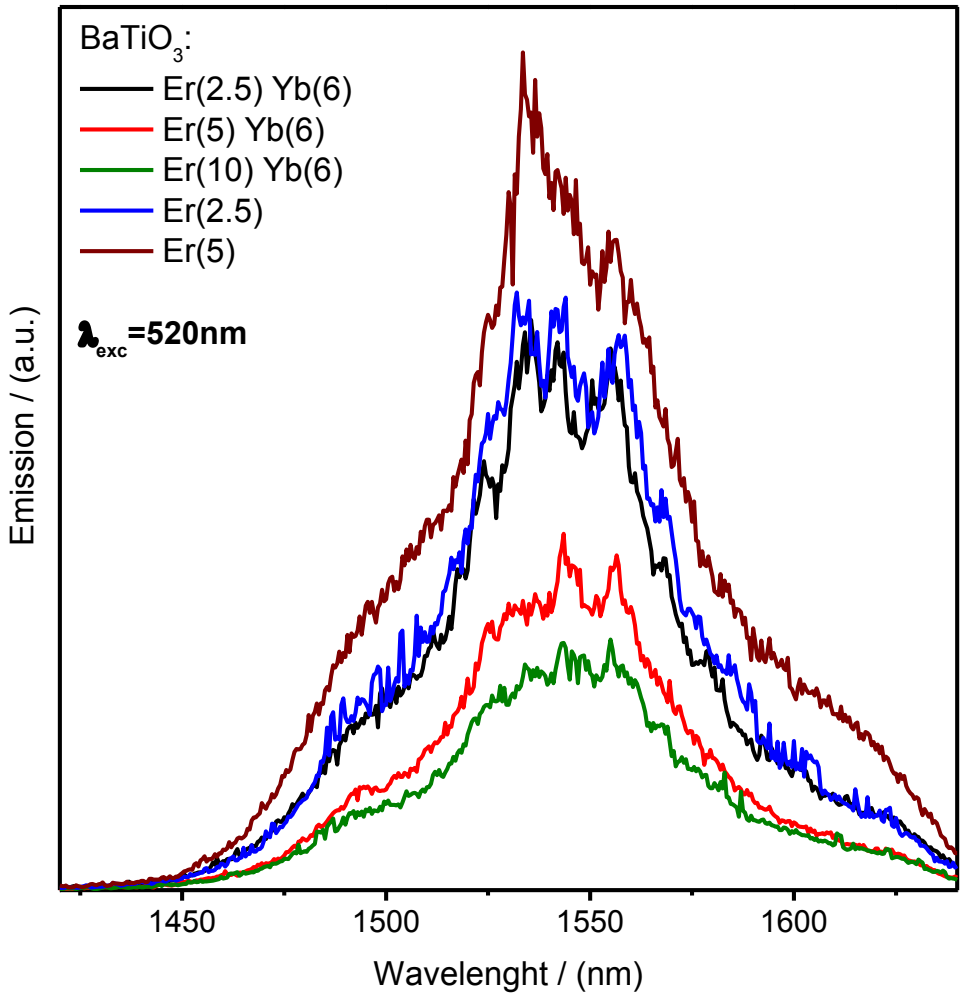

Figure 6-9. *Emission spectra of $BaTiO_3:Er^{3+}$ and $BaTiO_3:Er^{3+},Yb^{3+}$ powders heat treated at 700 °C, λ_{exc}=520 nm (region: 1425-1650 nm).*

However this channel is cut off when the ytterbium ions are present in the sample. This is so because there is a very efficient energy transfer from erbium to ytterbium ions, as shown previously. We now recall that for single doped samples we could not rule out the up-conversion process when the erbium concentration is increased and have two ions in the $^4I_{13/2}$ state. For this case one of the two ions is promoted to the $^4I_{9/2}$ state. When this energy transfer mechanism occurs, the emission of the $^4I_{13/2}$ state also takes place but this emission diminishes since that state is not fed anymore from the above state. The experimental data in Figure 6-9 shows that indeed this emission diminishes as the Erbium concentration increases.

The nature of the red emission for all cases shown in Figure 6-6 can be assumed to take place by a non-radiative decay from the $^2S_{3/2}$ to the $^4F_{9/2}$ and then radiatively from the $^4F_{9/2}$ to the ground state of the Erbium ions. As observed in Figure 6-6, this transition is not affected by the presence of Ytterbium ions and its corresponding intensity peak does not change by changing the Erbium concentrations.

6.2.2 Pumping at 970 and 940 nm

When pumping at 970 nm both rare earth ions are excited and, when pumping at 940 nm the ytterbium ions are the only ones that are excited. The emission spectra for the former case are shown in Figure 6-10 and the latter in Figure 6-11; notice that in the latter figure we only show the emission spectra for codoped samples. The observed green and red emissions can be assigned to the $^2H_{11/2}$, $^4S_{3/2}\rightarrow{}^4I_{15/2}$ and to the $^4F_{9/2}\rightarrow{}^4I_{15/2}$ erbium transitions, respectively. The $^2H_{11/2}$ and $^4S_{3/2}$ states get populate through a two photon up-conversion process, that is, with a 970 nm wavelength laser source the $^4I_{11/2}$ state of erbium ions gets populated; one ion in that state can absorb one photon from the pumping source and be promoted to such excited states. Also, it might happen through a non-radiative energy transfer process between two excited Erbium ions in the $4I_{11/2}$ state; one ion transfers its energy to another ion and populates the $^2H_{11/2}$ and $^4S_{3/2}$ states, see Figure 6-7. To explain the quenching of the luminescence of the green band as the Erbium concentration increases

for single and doped samples, one should consider the cross relaxation of the type $^4S_{3/2}+^4I_{15/2}\rightarrow{}^4I_{9/2}+^4I_{13/2}$ as before for the case when pumping at 520 nm.

For codoped samples the quenching of the green emission is stronger than for the single doped samples and the red band emission peaks higher than the peak emission observed for single doped samples. To give account for the change of the red emission one should consider an additional process besides the up-conversion and cross relaxation mechanisms discussed above. We recall that for codoped samples pumped at 520 nm the $^4I_{13/2}$ state of the erbium ions gets populated by the assumed cross relaxation and that this state is not fed anymore trough the $^4I_{11/2}$ since most of the energy goes to the $^2F_{5/2}$ state of the ytterbium ions. It was also shown that the up-conversion process from the $^4I_{13/2}$ state to the $^4I_{9/2}$ takes place as the erbium concentration increases.

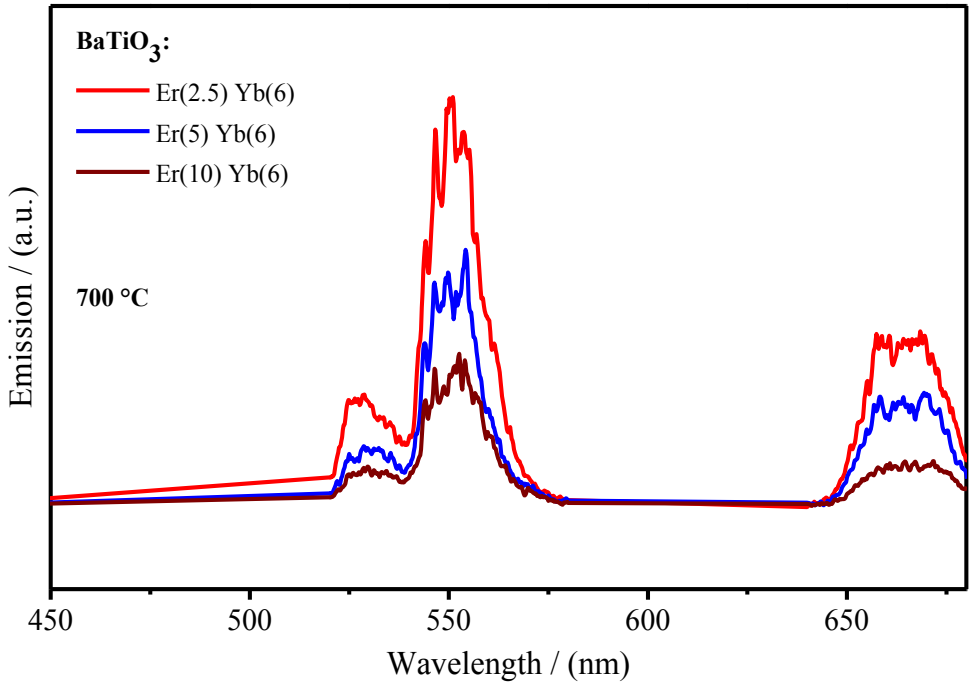

Figure 6-10. *Emission spectra of $BaTiO_3$:Er^{3+},Yb^{3+} heat treated at 700 °C, λ_{exc}=970 nm.*

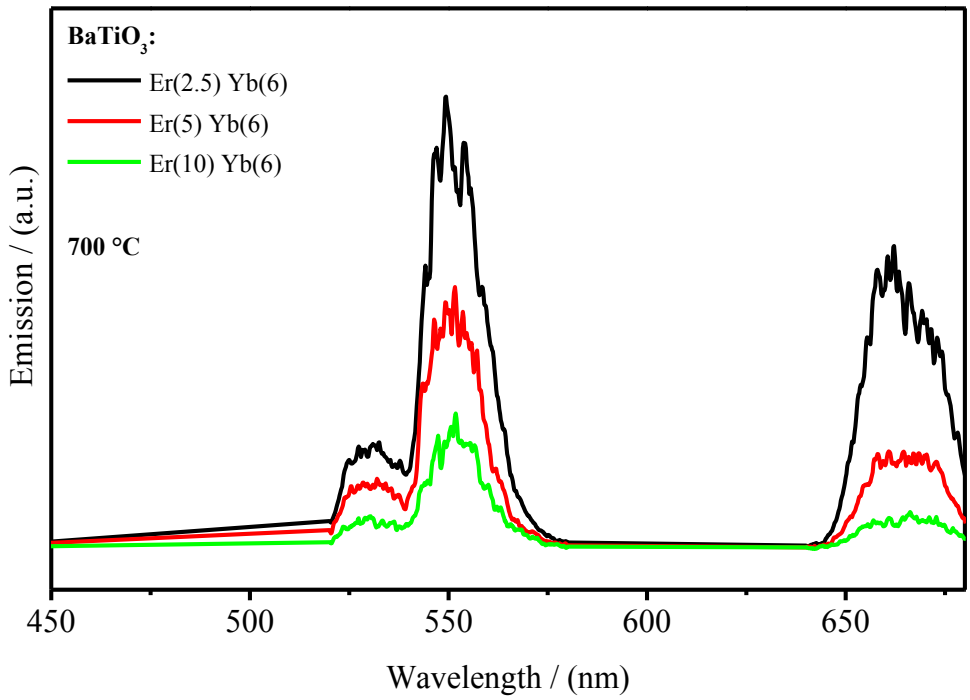

Figure 6.11. *Emission spectra of $BaTiO_3:Er^{3+},Yb^{3+}$ heat treated at 700 °C, λ_{exc}=940 nm.*

All these mechanisms are also valid when pumping at 970 nm but there is also a back energy transfer process from ytterbium ions. This interaction between erbium and ytterbium ions promotes the erbium ions at $^4I_{13/2}$ state to the $^4F_{9/2}$ state and from there the red emission takes place. Therefore, since the assumed mechanism takes place through the ytterbium ions and the emissions of these ions diminish (see Figure 6-6) as the erbium concentration increases we do expect that the red emission from the $^4F_{9/2}$ to the ground state of erbium also diminishes.

The above discussion to explain the changes of the peak intensity of the green and red bands in Figure 6-10 for codoped samples can also be considered for Figure 6-11. The emission spectra shown in this figure correspond to the codoped samples when pumped at 940 nm, i.e the ytterbium ions are the only ions that are excited with the laser source. The general behaviour of the green and red bands is similar to those for Figure 6-11, however it should be notice that in Figure 6-11 the peak intensity of the red band has been enhanced when compared to the green band. That is, the intensity of the red band is comparable to the intensity of the green one. This is so because we now are pumping the ytterbium ions and therefore the non-radiative energy transfer from ytterbium to erbium ions is more efficient

than for the previous case when pumping at 970 nm and where a back energy transfer was considered.

6.2.3 Pumping at 800 nm

We did also pump the codoped samples at 800 nm and Figure 6-12 shows the emission spectra. Therefore, for highly doped samples (single and double doped) with erbium and ytterbium ions in a barium titanate matrix the quenching process plays the main rule. This is in contrast to the results reported by Capobianco with yttrium oxide matrix [66]. The fluorescence emission and up-converted luminescence reported by these authors do not show quenching at all. That is, when pumping at either $^4F_{7/2}$ or $^4I_{11/2}$ states the observed luminescence increases as the dopant concentration increases. From the experimental data and the above discussion we can summarize our results in the following way.

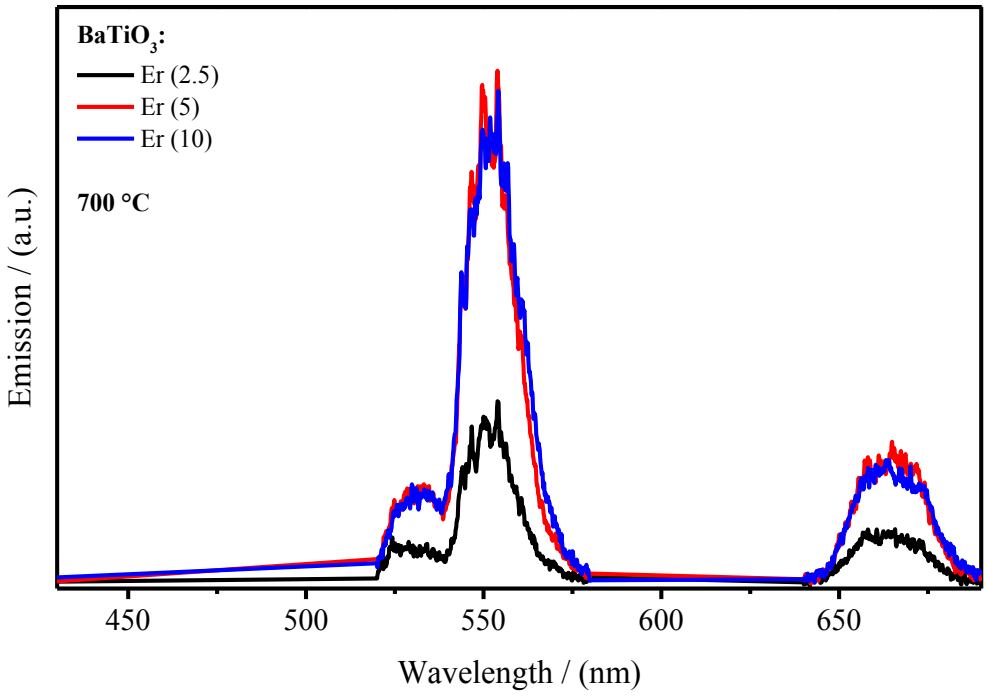

Figure 6.12. *Emission spectra of $BaTiO_3$:Er^{3+},Yb^{3+} heat treated at 700 °C, λ_{exc}=800 nm.*

For the green emission of the single and codoped samples the cross relaxation mechanism of the type $^4S_{3/2}+^4I_{15/2}\rightarrow{}^4I_{9/2}+^4I_{13/2}$ depletes the $^2H_{11/2}$ and $^4S_{3/2}$ states and it depends on the erbium concentration. Due to this mechanism and for single doped samples the fluorescence emissions from the $^4I_{11/2}$ and $^4I_{13/2}$ states become stronger as the erbium concentration increases. Further, two weak up-conversion processes take place from such levels to the $^2H_{11/2}$ and $^4S_{3/2}$ and, $^4I_{9/2}$ states, respectively; these emissions also depend on erbium concentration. However, when the ytterbium ions are present for the codoped samples the fluorescence emission at 1500nm becomes weaker as the Erbium concentration increases. This is so because the $^4I_{13/2}+^4I_{13/2}\rightarrow{}^4I_{9/2}+^4I_{15/2}$ and $^4I_{13/2}(Er)+^2F_{5/2}(Yb)\rightarrow{}^4F_{9/2}+^2F_{7/2}$ up-conversion processes deplete the $^4I_{13/2}$ Erbium state. In addition to these processes the erbium ($^4I_{11/2}$) to ytterbium ($^2F_{5/2}$) energy transfer is very efficient and no fast non-radiative decay from the $^4I_{11/2}$ to the $^4I_{13/2}$ states of erbium occurs. Therefore, it is clear from this depicted picture of the involved mechanisms in our codoped samples that most of the input energy to our samples goes to ytterbium ions. So, it is pertinent to wonder where all this energy ends up. That is most of the involved processes cycle the input energy and two main exits for the input energy can be observed, one is the quenched emissions and the other is the ytterbium ions.

However, Figure 6-12 shows that the fluorescence emission from ytterbium ions diminish as the erbium concentration increases. The expected result should be the reversed behaviour. On the other hand, Boulon et al. reported, recently, that ytterbium ions pairs are formed in barium titanate single doped ytterbium. They show that the emission of these ions pairs is the 500 nm region. We had at hand three samples $BaTiO_3$: Yb with Ytterbium at 2, 4 and 6 mol%. These samples were shines at different wavelengths in the 900 nm region and the Ytterbium ions pairs emission was observed, see Figure 6-13. Therefore, one might consider that this emission is also present in our codoped samples but it is screened by the erbium emission in the 500 nm region, and our detectors could not register it.

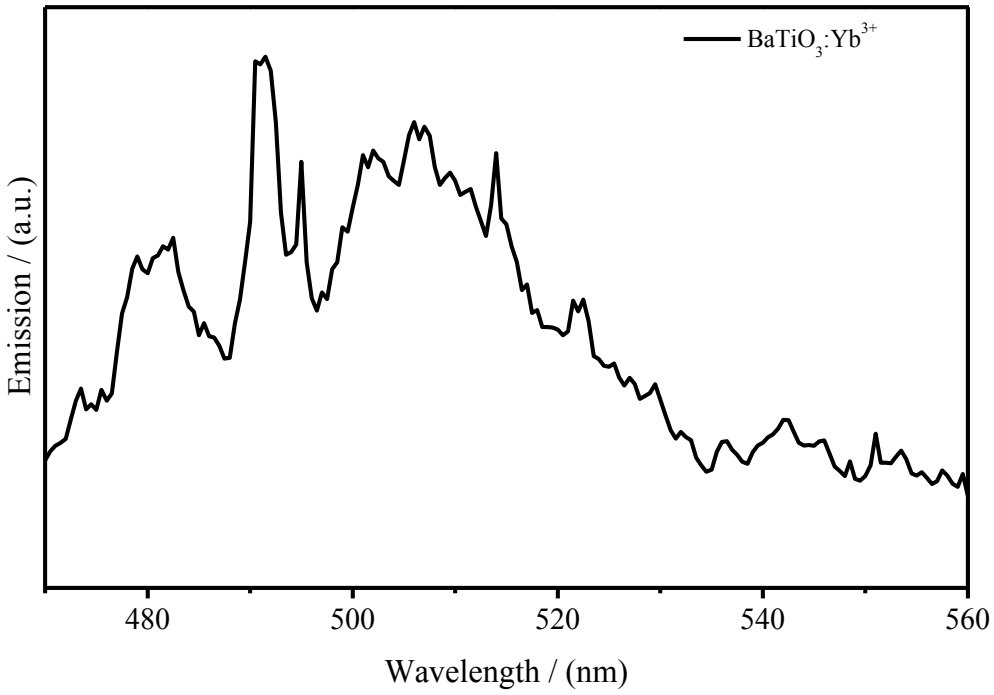

Figure 6-13. *Emission spectra of $BaTiO_3$:Yb^{3+} powders heat treated at 700 °C, λ_{exc}=915 nm.*

6.3 Luminescent properties of $BaTiO_3$:Er^{3+} films

Figure 6-14 shows the up-conversion spectra of Er^{3+} doped $BaTiO_3$. Figure 6-14a shows two emission transitions corresponding to $^4S_{3/2}\rightarrow{}^4I_{15/2}$ at 548 nm and $^4F_{9/2}\rightarrow{}^4I_{15/2}$ at 670 nm; at 974 nm, excitation was observed. For the 974 wavelength, the green emission at 548 is more intense because the $^4S_{3/2}\rightarrow{}^4I_{15/2}$ is spin-allowed; consequently, the emission is bright even to the naked eye. When pumped at 973 nm excitation, cooperative energy transfer (CET) also takes place and results in green up-conversion emission. It is known that $^4I_{11/2}$ has zero emission probability to the ground state. As shown in Figure 6-14 (inside), an Er^{3+} ion in the $^4I_{11/2}$ state relaxes to the ground state non-radiatively and transfers its energy to another neighboring one (also in $^4I_{11/2}$ state), promoting the latter to $^4F_{7/2}$. The $^4I_{11/2}$ state has a much longer lifetime than others [56, 168], which favors the excitation of Er^{3+} from this level to $^4F_{7/2}$ through cooperative energy transfer.

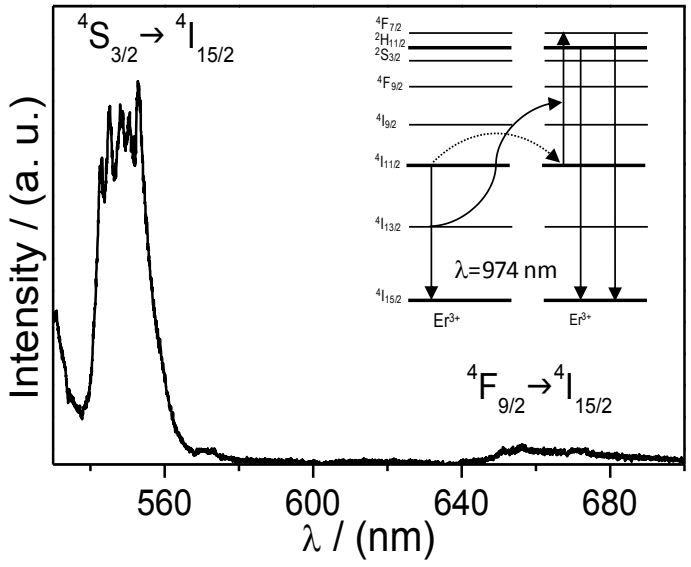

(a)

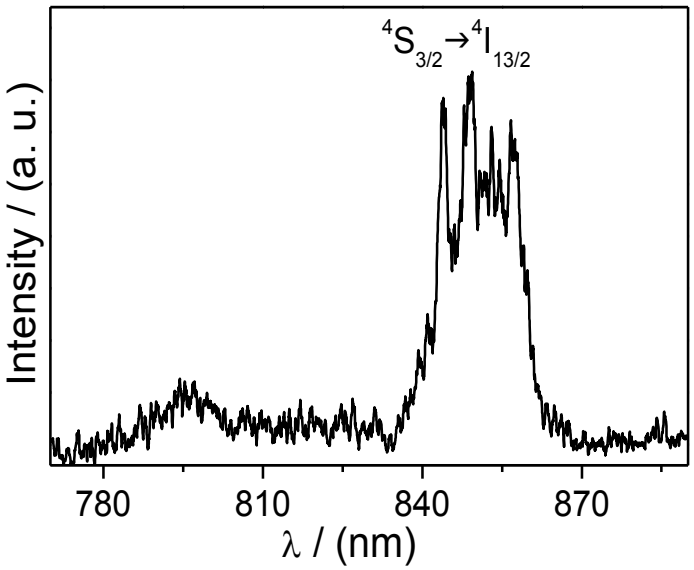

(b)

Figure 6-14. *Emission spectra of $BaTiO_3$:Er (0.5 %mol) after 974 nm excitation.*

Furthermore, Figure 6-14b shows that there is no emission at 800 nm from the $^4I_{9/2}$ level, but an intense luminescence was observed at 860 nm for $BaTiO_3$:Er (0.5 mol%), as was detected by Meneses-Nava in $BaTiO_3$:Er^{3+},Yb^{3+} powders [67] .This is expected because the

$^4S^{3/2}$ level depopulates by means of a cross-relaxation mechanism from $^4S_{3/2} + {}^4I_{15/2} \rightarrow {}^4I_{9/2} + {}^4I_{13/2}$. It is important to note that the green and infrared emissions were detected despite the low concentration of Er^{3+} ions (0.5 %mol) in the $BaTiO_3$ matrix; these features prevent the quenching effect in the luminescence (mainly in the region of 860 nm). Unfortunately, Er doped $BaTiO_3$ multilayer film (without PVP) displayed low thickness, and it was not possible to analyze its luminescent properties.

6.4 Luminescent properties of $BaTiO_3:Eu^{3+}$ films

The room temperature of photoluminescence emission spectra of $BaTiO_3:Eu^{3+}$ (5 mol%) film in the range 550-700 nm exited at 250 nm wavelength is shown in Figure 6-15. Red emission from the film doped with 5 mol% can see with the naked eye when excited with a 254 nm Uv lamp on the film.

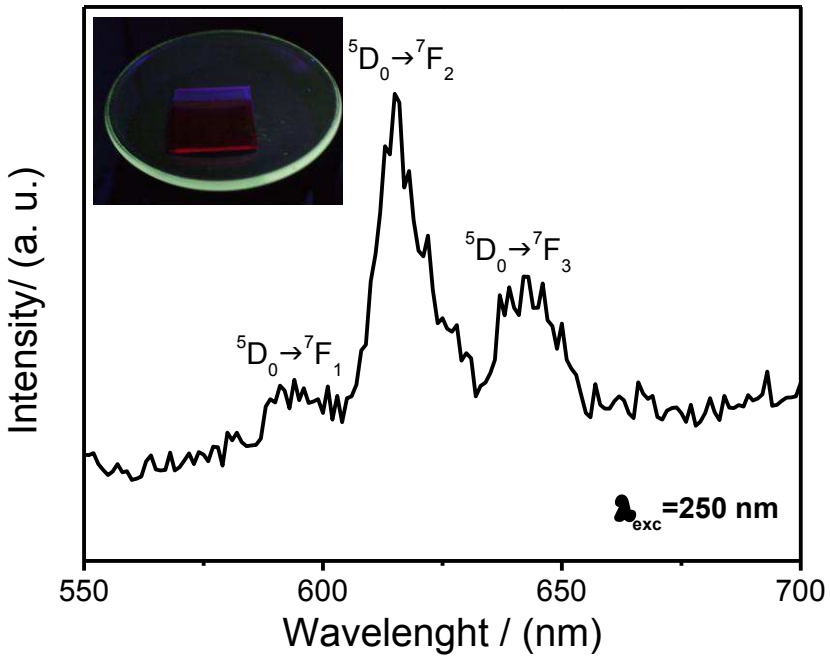

Figure 6-15. *PL spectrum of $BaTiO_3:Eu^{3+}$ of films heat treated at 700 °C and $BaTiO_3:Eu^{3+}$ under UV excitation (inside).*

For the emission spectra of the $BaTiO_3$:Eu^{3+} films, the peaks at 595, 615 and 645 nm are assigned to $^5D_0 \rightarrow {}^7F_1$, $^5D_0 \rightarrow {}^7F_2$ and $^5D_0 \rightarrow {}^7F_3$, respectively, arising from the lowest excited $^5D_0$ level into the split by the crystal field ^7F_J (where J=0, 1, 2, 3, 4, 5, 6) as observed by other authors [147-149]. In most cases, transitions to the higher laying levels ($^7F_5$, $^7F_6$) are difficult to detect due to their low intensity [149]. The dominating peak is observed around 615 nm, corresponding to $^5D_0 \rightarrow {}^7F_2$ transitions of the europium ions. This fact can be explained by the fact that the sample heated at 700 °C has higher level of crystallization, which directly leads to the narrow emission bands. It must be mentioned that the emission lines of the $BaTiO_3$:Eu^{3+} films are weak, probably due to the final thickness, influencing directly the suitable effective value of providing high emission [27]. Additionally, the sample sintered at 700 °C shows the silica substrate contribution (see XRD patterns), where the peaks are superimposed on the glass support. This indicates, probably, that some of the Eu^{3+} ions are placed in the amorphous surroundings, indicating the symmetry of the system is not too high.

6.5 XPS characterization of $BaTiO_3$:Er^{3+} films

The XPS technique was used in this study for investigating valence states of elements in Er doped $BaTiO_3$ by means of photoelectron peaks connecting with core-level binding energy. Figure 6-16a shows the XPS spectrum of the typical Er-doped $BaTiO_3$. The XPS peaks show that the particles contain only Ti, Ba, O and Er and a trace amount of carbon and nitrogen. No other element is detected. The Ti 2p XPS spectrum for the $Ba_{1-x}Er_xTiO_3$ is shown in Figure 6-16b. In this spectrum, two main peaks are identified: Ti $2p_{3/2}$ at 459.4 eV and Ti $2p_{1/2}$ at 465 eV, in agreement with other reports on Ti 2p XPS for $BaTiO_3$ [169], and $SrTiO_3$ [170] with a Ti^{4+} profile. In these samples, the presence of a Ti^{3+} 2p XPS peak was not observed; nevertheless, the Ti^{3+} ion exists if the Δ_{FWHM} value of the Ti $2p_{3/2}$ main peak is wider than that of TiO_2 (1.9 eV) and $BaTiO_3$ (<2.0 eV) [1, 171]. The measured value of Δ_{FWHM} for our sample was 2.73 eV, suggesting that mixed Ti^{4+}/Ti^{3+} ions co-exist.

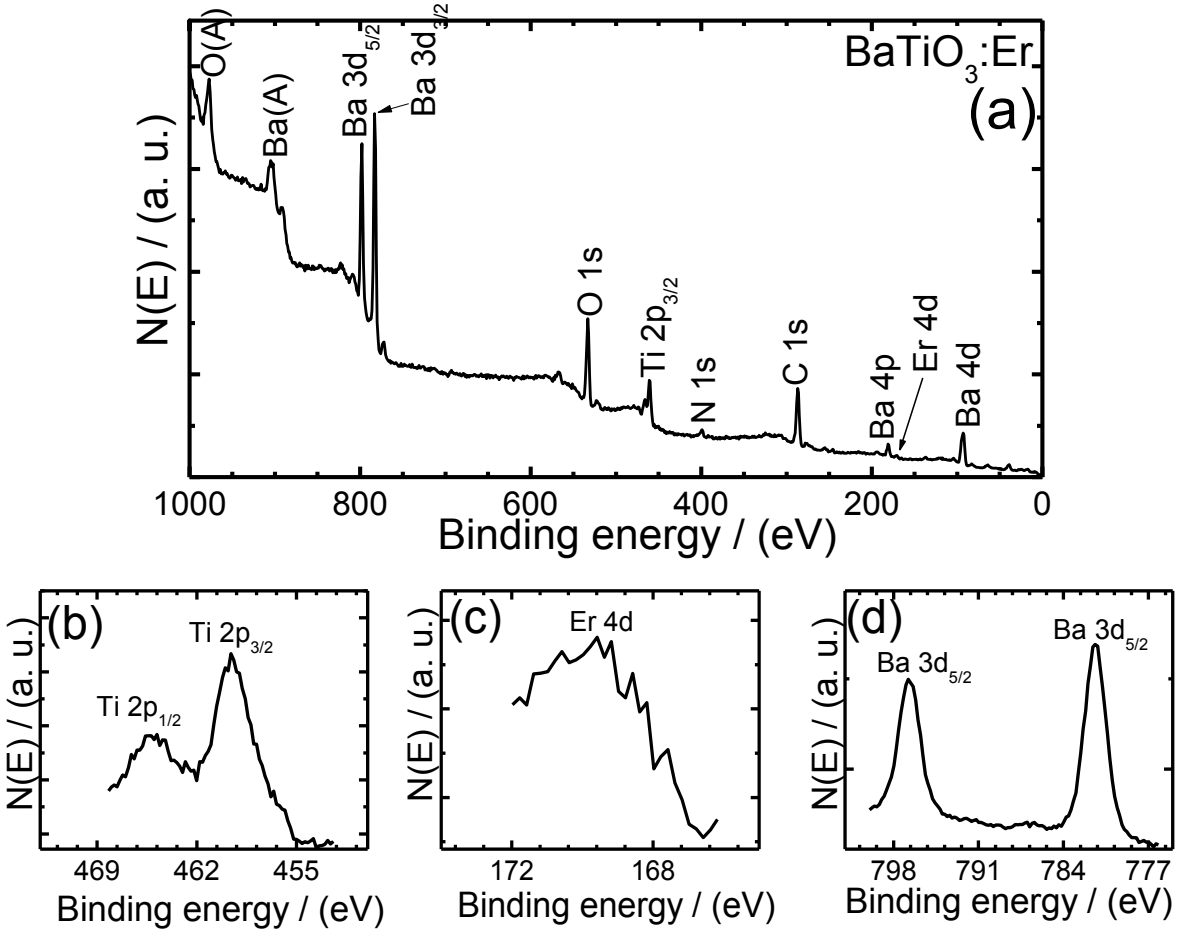

Figure 6-16. *XPS spectra for the $BaTiO_3$:Er (a), Ti 2p (b), Er 4d (c) and Ba 3d (d).*

Particularly, the XPS spectra of Er 4d (Figure 6-16c) at about 169.6 eV, indicate that Er ions in the $Ba_{1-x}Er_xTiO_3$ are in valence of Er^{3+}. Ba 3d XPS spectra in Figure 6-16d showed the core-level binding energies of Ba $3d_{5/2}$ and Ba $3d_{3/2}$ situated at 781.4 eV and 796.8 eV, respectively. Taking into account the XPS observations, the substitution of Er^{3+} for A-site Ba in $BaTiO_3$ let us to establish that the compensating mechanism in the $Ba_{1-x}Er_xTiO_3$ system occurs by the formation of titanium vacancies, due to the fact that V_{Ti} as charge compensation defects is preferred over the formation of barium vacancies when the donor dopant concentration ≥0.5[15] and can be expressed by the dynamic equilibrium: $Er_2O_3 + Ba_{Ba} + 2Ti_{Ti}^{3+} + V_{Ti} \leftrightarrow 2Er_{Ba}^{3+} + Ti_{Ti}^{4+} + BaTiO_3$.

Conclusions

This work was focused to the preparation of $BaTiO_3$ powders, nanoparticles and films synthesized by solid state route, hydrothermal and sol-gel methods as well as to the study to structural and optical properties. $BaTiO_3$ perovskite has the capability to incorporate rare earth ions of different size exhibiting luminescent properties, specifically when is doped by Eu^{3+}, Er^{3+} and Yb^{3+} ions, also, these ions can be employed as optical probe in this matrix.

Europium doped barium titanate prepared by hydrothermal route and solid state reaction presented cubic and/or tetragonal phases depending of the used method. The size of the powder obtained by hydrothermal route was 25 nm meanwhile by using the solid state reaction the particle size was increased up to 200 nm after 1150 °C heat treatment.

The presence of the erbium and ytterbium ions in the $BaTiO_3$ matrix provokes red, green and blue emissions which are originated by $^4S_{3/2}$ and $^4F_{9/2}$ transitions.

In this work emission spectra and lifetime decays of single and co-doped Er^{3+} and Yb^{3+} ions in $BaTiO_3$ polycrystalline sol–gel matrix were measured to describe the mechanisms that drive the fluorescence and the observed quenching. For both systems single and co-doped samples were a cross-relaxation mechanism, $^4S_{3/2} + {}^4I_{15/2} \rightarrow {}^4I_{9/2} + {}^4I_{13/2}$, which quenches the green fluorescence and it was demonstrated that this mechanism depends on Er^{3+} concentration. The enhanced concentration quenching in co-doped samples is due to energy transfer between neighbouring Er^{3+} –Yb^{3+} ions. For this case, emission of the $^4I_{13/2}$ and $^4I_{11/2}$ levels diminished as Er^{3+} concentration increases; but this behavior is the contrary for single doped Er^{3+} samples. The lengthening of the lifetime decay of $^4S_{3/2}$ level, in co-doped samples, is due to an energy back transfer, which also affects the quenching of the $^4I_{11/2}$ level. Further, when single doped Yb^{3+} samples were pumped at 940 nm, an emission from Yb^{3+} pairs was measured at about 500 nm. This process should be present in co-doped Er^{3+}–Yb^{3+} samples and contributes to the quenching of emission at about 1.0 μm.

The heat treatment at intermediate temperature and the use of chelating agents allows to control the shape of the particles in the sol-gel systems. The particle shape and size could be tailored in the un-doped and codoped $BaTiO_3$ system by tailoring the chelating agents and the heat treatment temperature. The morphology of $BaTiO_3$ (undoped and codoped) compounds with and without chelating agents differs greatly. The microstructure of the derived materials is more spherical than non-chelating agents and the size of the particles is lower (96–337 nm) than that obtained without (AcAc)H and acetic acid (137–312 nm). Further, the morphology of the undoped and codoped $BaTiO_3$ particles in presence of chelating agents at 700 and 950 °C results in a combination of nanorods and nearly spherical structures associated with the cubic and tetragonal phase, respectively. At 1150 °C, the $BaTiO_3$ and $BaTiO_3$:Er, Yb powders exhibit a tetragonal phase (predominant), and only nearly spherical particles were observed. Isolated cubic structure un-doped and co-doped $BaTiO_3$ nanorods, with diameters ranging from 100 to 120 nm and reaching 800 nm in length, presenting for both undoped and codoped system. From the addition of chelating agents as the acetylacetone and acetic acid were observed an important change in the morphology of the powders was observed, i.e. the presence of the chelating agents allow to form quasi spherical particles (tetragonal structure). Tetragonal structure, can be fabricated by this route when $Ba(C_5H_7O_2)_2$, $Ti(OPr^i)_4$ are selected as starting materials and (AcAc)H, H–(OAc) are chosen as chelating agents. The influence of calcination temperature and chelating agents on the surface area, pore radius and pore volume of $BaTiO_3$:Er, Yb were also investigated

A notable result associated with the elaboration of $BaTiO_3$:Er, Yb films was the influence of the chelating agents in the synthesis on the films. $BaTiO_3$:Er, Yb optical thin films are only obtained in the presence of chelating agents, in contrast with the films prepared without them, which were characterized by granular networks showing poor adhesive properties toward the substrates and cracks. The best film, in terms of homogeneity in morphology, was obtained using chelating agents at 950 °C, resulting in the formation of highly cross-linked and uniform films, composition, low porosity, and a mean surface roughness of 12.4 nm.

The good optical films formation of $BaTiO_3$:Er, Yb system concerning the high quality, do not allow the high thickness, so it was establish the addition of polyvinylpirrolidone (PVP) during the process arising for the first time monolayer of high thickness (828 nm), value determined by m-lines spectroscopy technique. Using PVP the morphology resulted in a flower-like morphology characterized by high homogeneity, low porosity, and even distribution of doping ions. XPS analysis indicates that the compensating mechanism in $BaTiO_3$:Er^{3+} can be expressed by the dynamic equilibrium $Er_2O_3 + Ba_{Ba} + 2Ti_{Ti}^{3+} + V_{Ti} \leftrightarrow 2Er_{Ba}^{3+} + Ti_{Ti}^{4+} + BaTiO_3$. The optical studies showed the up-conversion properties of Er^{3+} doped $BaTiO_3$ films upon 974 nm infrared excitation and demonstrated that the green emission at 548 nm was predominant under this excitation. This effect was explained in terms of cooperative energy transfer between two Er^{3+} ions.

Finally, $BaTiO_3$:Eu^{3+} systems were obtained in powders and films using sol-gel method incorporating a viscosity modifier (PVP) in the sol. Both systems exhibited crystalline $BaTiO_3$ phase at 700 °C within 2 h as revealed the HT-XRD studies. The powders were mainly spherical with some rod shapes; however, the films presented good surface morphology as detected by SEM. The obtained films exhibit the room temperature photoluminescence of the europium ions, with the predominant band at 615 nm ($^5D_0 \rightarrow {}^7F_2$) transition). The obtained thickness (~500 nm) of $BaTiO_3$:Eu^{3+} films must be optimized to be promising for luminescent applications.

References

1. B. I. Lee. J. Electroceram. 3 (1999) 53.
2. J. Xu, W. Menesklou and E. Ivers-Tiffee. J. Eur. Ceram. Soc. 24 (2004) 1735.
3. B. C. Frazer, H. R. Danner and R. Pepinsky. Phys. Rev. 55 (1955) 745.
4. Woo-Seok C. J. Phys. Chem. Solids 59-5 (1998) 659.
5. T. A. Colson, M. J. S. Spencer, I. Yarovsky. Comput. Mater. Sci. 34 (2005) 157.
6. M.-S. Zhang, J. Yu, W.-C. Chen, Y. Zhen. Prog. Cryst. Growth Charact. Mater. 40 (2000) 33.
7. W. Strek, D. Hreniak, G. Boulon, Y. Guyot, R. Pazzik. Opt. Mater. 24 (2003) 15.
8. J. Amami, D. Hreniak, Y. Guyot, R. Pazik, C. Goutaudier, G. Boulon, M. Ayadi, W. Strek. J. Lumin. 119–120 (2006) 383.
9. A. Lotnyk , A. Graff, S. Senz, N.D. Zakharov, D. Hesse. Solid State Sci. 20 (2007) 1.
10. J. H. Lee, C. W. Won, T. S. Kim, H.S. Kim. J Mater. Sci. 35 (2000) 4271.
11. T. Fukui, C. Sakurai, M. Okuyama. J Mater. Sci. 32 (1997) 189.
12. S. Doeuff, M. Henry, C. Sanchez and J. Livage. J Non-Cryst. Solids. 89 (1987) 206.
13. M. Boulos, S. Guillemet-Fritsch,T. F. Mathieua, B. Durand, T. Lebey, V. Bley. Solid State Ion. 176 (2005) 1301.
14. D. M. Smyth. Solid State Ionics 129 (2000) 5.
15. M.T. Buscaglia, V. Buscaglia, M. Viviani, O. Nanni, M. Hanuskova. J. Eur. Ceram. Soc. 20 (2000) 1997.
16. F. Auzel, E. J. Trzebiatowska, J. Lengendziewics Strek W. Rare earth spectroscopy. World Scientific. Singapure, 1985
17. J.E. Geusic, H. M. Marcos, L. G. Van-Uitert. Appl. Phys. Lett. 4 (1964) 182.
18. K. A. Levine, P. C. Frank. Appl. Phys. Lett. 5 (1964) 118.
19. Z. Cheng Li, B. Bergman. J. Eur. Ceram. Soc. 45 (2004) 4987
20. H. X. Zhang, C.H. Kam, Y. Zhou, X.Q. Han, Q. Xiang, S. Buddhudu, Y.L. Lam, Y.C.Chan J. Alloys Compd. 308 (2000) 134.
21. N. Setter, R. Waser, Acta Mater. 48 (2000) 151.
22. Jin Hyun Hwang, Young Ho Han. Solid State Ionics 140 (2001) 181.
23. H. X. Zhang, C.H. Kam, Y. Zhou, X.Q. Han, S. Buddhudu, Y.L. Lam. Opt. Mater. 15 (2000) 47.
24. J. Amami, D. Hreniak, Y. Guyot, R. Pazik, W. Strek, C. Goutaudier and G. Boulon. J. Phys. Condens. Matter. 19 (2007) 1.
25. E. E. Oren and A. C. Tas. Metall. Mater. Trans. B. 30, (1999) 1089.
26. B. Denker, B. Galagan, V. Osiko, S. Sverchkov, A.M. Balbashov, J.E. Hellstrom , V. Pasiskevicius, F. Laurell. Opt. Commun. 271 (2007) 142.
27. K. Battisha, Y. Badr, and A. G. A. Darwish. Inter. J. of Mater. Sci. 3 (2008) 95.

28. L. Laversenne, S. Kairouani, Y. Guyot, C. Goutaudier, G. Boulon, M.Th. Opt. Mater. 19 (2002) 59.
29. L. Min, W. Shiwei, Z. Jian, A. Liqiong, C. Lidong. J. Rare Earth 24 (2006) 732.
30. Ebelmen M. Ann. Chim. Phys. 15 (1845) 319.
31. M. Yoshimura, K. Byrappa. J. Mater Sci. 43 (2008) 2085.
32. Livage J. Lemerle J. Ann. Rev. Mater. Sci. 12 (1982) 103.
33. E. Matijevic, "Preparation of Uniform Inorganic Colloidal Particles," Encyclopedia of Surface and Colloid Science, Marcel Dekker, NY, 4322 (2002).
34. C. J. Brinker and G. W. Scherer. Sol-gel science: the physics and chemistry of sol-gel processing. Academic Press. ISBN 0-12-134970-5
35. Mazdiyasni K. S., Lynch C. T. Smith II J. S., J. Am. Ceram. Soc. 48 (1965) 372.
36. Wheat T. A., J. Canad. Ceram. Soc. 46 (1981) 22.
37. P. J. Flory, Principles of polymer chemistry. Cornell Univ. Press, Ithaca, N.Y. 1953
38. H. K. Henisch. Crystal growth in gels. Penn. state univ. Press, University Park, Pa. 1970 pag.41
39. Donald R. Uhlman, Donald R. Ulrich. Ultrastructure processing of avanced materials. ISBN 0-471-52986-9
40. A. Mosset, I. Gautier-Luneau, J. Galy, P. Strehlow And H. Schmidt. J. Non-Cryst. Solids. 100 (1988) 339.
41. O. A Harizanov. Mater. Lett. 34 (1998) 232.
42. Byrappa K, Yoshimura M (2001) Handbook of hydrothermal technology. Noyes Publications, NJ, USA.
43. M. Yoshimura. K. Byrappa. Hydrothermal processing of materials: past, present and future. J. Mater. Sci. 43 (2008) 2085.
44. K. Byrappa (2005) In: Kirk-Othmer encyclopedia of chemical technology. John Wiley & Sons, London.
45. M . Yoshimura J. Ceram. Soc. Jpn. 114 (2006) 888
46. K Byrappa, M. Yoshimura,Handbook of hydrothermal technology, ISBN:0-8155-1445-X
47. Ecker J. O. Jr., Hung-Houston, C. C. Gesrten, B. L. Lencka, M. M. and Riman R.E., J. Am. Ceram. Soc., 79 (1996) 2929.
48. H. Schmalzried. Solid State Reactions (Verlag Chemie: Weinheim, 1981)
49. S. Elliot. The Physics and Chemistry of Solids (John Wiley & Son, NY, 1998) Cap. 1
50. Tony Owen. Fundamentals of UV-visible spectroscopy. Agilent Technologies (2000) pp 2-6.
51. Scheps R. Prog. Quantum Electron. 20 (1996) 271.
52. L. Min, W. Shiwei, Z. Jian, A. Liqiong, C. Lidong. J. Rare Earths 24 (2006) 732.
53. Scheps R. Prog. Quantum Electron. 20 (1996) 271.
54. E. Heumann, S. Bär, K. Rademaker, G. Huber, S. Butterworth, A. Dienng, W. Seelert. Appl. Phys. Lett. 88 (2006) 061108.

55. E. Downing, L. Hesselink, R. Macfarlane. Science 273 (1996) 1185
56. F. Xu, Z. Lv, Y. G. Zhang, G. Somesfalean, Z. G. Zhang. Appl. Phys. Lett. 88 (2006) 231109.
57. G. S. Yi, H. C. Lu, S. Y. Zhao, Y. Ge, W. J. Yang, D. P, Chen, L. H. Guo. Nano Lett. 4 (2004) 2191.
58. G. Seisenberger, M. U. Ried, T. Endre, H. Büning, M. Hallek, C. Bräuchle. Science 294 (2001) 1929.
59. J. H. Zeng, J. Su, Z. H. Li, R. X. Yan, Y. D. Li. Adv Mater 17 (2005) 2119.
60. G. Huber, E. Heumann, T. Sandrock, K. Petermann. J. Lumin. 1 (1997) 72.
61. U. Hömmerich, E. Nyein, S. B. Trivedi. J. Lumin. 113(2005) 100.
62. G. Y. Chen, Y. G. Zhang, G. Somesfalean, Z. G. Zhang, Q. Sun, F. P. Wang. Appl. Phys. Lett. 89 (2006) 163105.
63. G. Y. Chen, Y. Liu, Y. G. Zhang, G. Somesfalean, Z. G. Zhang, Q. Sun, F. P. Wang. Appl. Phys. Lett. 91 (2007) 133103.
64. G.Y. Chen, G. Somesfalean, Y. Liu, Z. Zhang, Q. Sun, F.P. Wang. Phys. Rev. B. 75 (2007) 195204
65. S. L. Hinojosa Ruiz. Thesis: Espectroscopia y procesos de tranferencia de energía no radiativa en la matriz poli-cristalina YAG codopada con Yb3+ y Er3+ done in Centro de Investigaciones en Óptica A.C. (2005)
66. J. A. Capobianco, F. O. Vetrone, C. Boyer, A. Speghini and M. Bettinelli. J. Phys. Chem. B 106 (2002) 1181.
67. M. A. Meneses-Nava, O. Barbosa-García, J.L. Maldonado, G. Ramos-Ortíz, J.L. Pichardo, M. Torres-CisneroS, M. García-Hernández, A. García-Murillo, F.J. Carrillo-Romo. Opt. Mater. 31 (2008) 252.
68. L. Simon-Seveyrat, A. Hajjaji, Y. Emziane, B. Guiffard, D. Guyomar. Ceram. Int. 33 (2007) 35.
69. C. Sanchez, J. Livage, M. Henry, F. Babonneau. J. Non-Cryst. Solids 100 (1988) 65.
70. J. Livage, C. Sanchez, M. Hernry, S. Doeuff. Solid State Ion. 32–33 (1989) 633.
71. A. García Murillo, F. J. Carrillo Romo, M. García Hernández, J. Ramírez Salgado, M. A. Domínguez Crespo, S. A. Palomares Sánchez, H. Terrones. J. Sol-Gel Sci. 53 (2010) 121.
72. M. Bahtat, J. Mugnier, L. Lou, C. Bovier, J. Serughetti, M. Genet. J. Opt. 23 (1992) 215.
73. M. Stockenhuber, H. Mayer, J. A. Lercher. J. Am. Ceram. Soc. 76-5 (1993) 1185.
74. M. N. Kamalasanan, N. D. Kumar, S. Chandra. J. Appl. Phys. 76 (1994) 4603.
75. D. F. Hennings, C. Metzmacher, B. S. Schreinemacher. J. Am. Ceram. Soc., 84 (2001) 179.
76. G. Arlt, D. Hennings, G. D. With. J. Appl. Phys., 58(4) (1985) 1619–1625.
77. Y. Gao, Y. Masuda, Z. Peng, T. Yonezawa, K. Koumoto. J. Mater. Chem., 13 (2003) 608.
78. K. Sadhana, T. Krishnaveni, K. Praveena, S. Bharadwaj and S.R. Murthy. Scripta Mater. 59 (2008) 495.
79. A. L. Patterson. Phys. Rev. 56 (1939) 978.

80. S. Lee and C. A. Randall. J. Am. Ceram. Soc., 90-8 (2007) 2589.
81. W. G. Fateley, F. R. Dollish, N. T. McDevitt, F. F. Bentley. Infrared and Raman Selection Rules for Molecular and Lattice Vibrations; Wiley; New York, 1972.
82. J. D. Freire, R. S. Katiyar. Phys. Rev. B, 37, (1988) 2074.
83. X. Zhu, J. Wang, Z. Zhang, J. Zhu, S. Zhou, Z. Liu, and N. Ming. J. Am. Ceram. Soc. 91-3 (2008) 1008.
84. C. Chen. Mat. Chem. and Phys. 110 (2008) 186.
85. C. An. Mater. Res. Bull. 43 (2008) 932.
86. S. W. Lu, B. I. Lee, Z. L. Wang, W. D. Samuels. J. Cryst. Growth 219 (2000) 269.
87. R. Asiaie, W. Zhu, S.A. Akbar, P.K. Dutta, Chem. Mater. 8 (1996) 226-234.
88. H. Un-Yeon, P. Hyung-Sang, K. Kee-Kahb. J. Am. Ceram. Soc. 87-12 (2004) 2168.
89. M. H. Frey, D. A. Payne. Physical Rev. B, 54, (1996) 3158-3168.
90. L. Preda, L. Courselle, B. Despax, J. Bandet, A. Ianculescu. Thin Solid Films 389 (2001) 43.
91. G. Yang, Z. Yue, T. Sun, J. Zhao, Z. Yang, L. Li. Appl. Phys. A 91, (2008) 119-125.
92. D. Hreniak, W. Strek, J. Amami, Y. Guyot, G. Boulon, C. Goutaudier, R. Pazik. J. Alloys Comp. 380 (2004) 348.
93. J. Amami, D. Hreniak, Y. Guyot, R. Pazik, W. Strek, C. Goutaudier and G. Boulon, J. Phys.: Condens. Matter 19 (2007) 1.
94. L. M. Li, Y. J. Jiang, and L. Z. Zeng. J. Raman Spectrosc. 27-7 (1996) 503.
95. Y. J. Jiang, L. Z. Zeng, R. P. Wang, Y. Zhu and Y. L. Liu. J. Raman Spectrosc. 27-1 (1996) 31.
96. N. Baskaran, A. Ghule, C. T. Bhongale, R. Murugan, and H. Chang. J. Appl. Phys. 91-12 (2002) 10038.
97. R. Vivekanandan, T.R.N Kutty. Powder Technol. 57 (1989) 181.
98. R. Waser. J. Am. Ceram. Soc., 71, (1988) 58-63.
99. G. Busca, V. Buscaglia, M. Leoni, and P. Nanni, Chem. Mater. 6 (1994), 955.
100. E. W. Shi, C. T. Xia, W. E. Zhang, B. G. Wang and C. D. Feng,. J. Am. Ceram. Soc. 80 (1997) 1567.
101. L. Guo, H. Luo, J. Gao, L. Guo, L. Guo, J. Yang, Mat. Letters, 60 (2006) 3011.
102. M. Z. C. Hu, V, Kurian, E. A. Payzant, C. J. Rawn, R. D. Hunt, Powder Technol., 110 (2000) 2.
103. Y. B Khollam, A. S. Deshpande, A. J. Patir. Materials Sci. Communication, Mater. Chem. Phys. 71 (2001) 304.
104. L. Li, Y. Chu, Y. Liu, L. Dong, L. Huo, F. Yang. Mat. Lett. 60 (2006) 2138.
105. P. Yu, B. Cui, Q. Shi. Mater. Sci. Eng., A. 473 (2008) 34.
106. H. Kumazawa, K. Masuda. Thin Sol. Films 353 (1999) 144.
107. C. B. Samantaray, Anushree Roy, M. Roy, M. L. Mukherjee and S. K. Ray. J. Phys. Chem. Solids, 63 (2002) 65.
108. S. Ghosh, S. Dasgupta, A. Sen, H. S. Maiti. Mat. Lett. 61 (2007) 538.

109. M. H. Frey, Z. Xu, P. Han, and D. A. Payne, Ferroelectrics, 206-207 (1998) 337-353.

110. A. Y. Emelyanov, N.A. Pertsev, S. Hoffmann-Eifer, U. Bo Ttger and R. Waser. Journal of Electroceramics, 9 (2002) 5.

111. Y. L. Du, M. S. Zhang, Q. Chen, Z. Yin. Appl. Phys. A 76 (2003) 1099–1103.

112. V. Buscaglia, M.T. Buscaglia, M. Viviani, T. Ostapchuk, I. Gregora, J. Petzelt, L. Mitoseriu, P. Nanni, A. Testino, R. Calderone, C. Harnagea, Z. Zhao, M. Nygren. J. Eur. Ceram. Soc. 25 (2005) 3059.

113. X. Y. Deng, X. H. Wang, H. Wen, A. G. Kang, Z. L. Gui, L.T. Li. J. Am. Ceram. Soc. 89 (2006) 1059.

114. R. Cho, S.H. Kwun, T.W. Noh, M.S. Jang, Jpn. J. Appl. Phys. 36 (1997) 2196.

115. W.K. Kuo, Y.C. Ling. J. Mater. Sci. 29 (1994) 5625.

116. L. Kaiser, M.D. Vaudin, G. Gillen, C.S. Hwang, L. H Robins, L.D. Rotter. J. Crystal Growth 137 (1994) 136-140.

117. C.J. Xiao, C.Q. Jin, X.H. Wang, Crystal structure of dense nanocrystalline BaTiO3 ceramics, Materials Chemistry and Physics 111 (2008) 209–212.

118. H.X. Zhang, C.H. Kam, Y. Zhou, X.Q. Han, Y.L. Lam, Y.C. Chan, K. Pita. Mater. Chem. Phys. 63 (2000) 174–177.

119. S. Zhang, F. Jiang, Gang Qu, C. Lin, Materials Letters 62 (2008) 2225.

120. N. C. Pramanik, S. I. Seok, B. Y. Ahn, J. Colloid Interface Sci. 300 (2006) 569.

121. I.J. Clark, T. Takeuchi, N. Ohtori, D.C. Sinclair, J. Mater. Chem. 9 (1999) 83.

122. M. Stockenhuber, H. Mayer and Lercher. J. Am. Ceram. Soc. 76-5 (1993) 1185.

123. D. Hennings, S. Schreinemacher, J. Eur. Ceram. Soc. 9 (1992) 4.

124. S. Wada, T. Suzuki, T. Noma, J. Ceram. Soc. Jpn. 104 (1996) 383.

125. E.W. Shi, C.T. Xia, W.E. Zhang, B.G. Wang, C.D. Feng, J. Am. Ceram. Soc. 80 (1997) 1567.

126. J. Livage, M. Henry, C. Sanchez. Progress in solid state chemistry, 18-4, (1988) 259.

127. L. G. Hubert-Pfalzgraf. New J. Chem. 11 (1987) 663.

128. K. H. Von Thiele and M. Panse. Z. Anorg, Allg.Chem. 44 (1978) 23.

129. T. Yoko, K. Kamiya, K. Tanaka. J. Mater. Sci. 25 (1990) 3922.

130. C. Legrand-Buscema, C. Malibert, S. Bach. Thin Sol. Films. 418 (2002) 79.

131. J. Livage and M. Henry, in: J. D Mackenzie and D. R. Ulrich, Eds. Ultrastructure Processing of Advanced Ceramics, Wiley, New York (1988) p. 183.

132. M. Cernea, O. Monnereau, P. Llewellyn, L. Tortet, C. Galassi. J. European Ceram. Soc. 26 (2006) 3241.

133. J. Yu, J. Chu, M. Zhang. Applied Physics A 74, 645-647 (2002).

134. T. Takeuchi, K. Ado, T. Asai, H. Kageyama, Y. Saito, C. Masquelier, O. Nakamura. J. Am. Ceram. Soc. 77 (1994) 1665.

135. S.-W. Know, D.-H. Yoon. Ceram. Int. 33 (2007)1357.

136. P. Yu. X. Wang, B. Cui. Scripta Mat. 57 (2007) 623.
137. W. Li, Z. Xu, R. Chu, P. Fu, J. Hao. J. Alloys and Comp. 484 (2009) 137.
138. F. Huang, J.F. Banfield. Nano. Lett. 3 (2003) 373.
139. W.-D. Yang, S. M. Haile. J. European Ceram. Soc. 26 (2006) 3203.
140. A. García Murillo, A. de J. Morales Ramírez, F. Carrillo Romo, M. García Hernández, Miguel A. Domínguez Crespo. Mater. Lett. 63 (2009) 1631.
141. A.García Murillo, F. de J. Carrillo Romo, C. Le Luyer, M. García Hernández, S. Palomares Sánchez. J. Sol-gel Sci. and Technol. 50-3 (2009) 359.
142. J. Madarasz, S. Kaneko, M. Okuya, G. Pokol. Thermochim. Acta. 489 (2009) 37.
143. A. Legrand-Buscema, C. Malibert, S. Bach. Thin Sol. Films. 2002, 418, 79-84.
144. K. Watanabe, H. Ohsato, H. Kishi, Y. Okino, N. Kohzu, Y. Iguchi, T. Okuda. Solid State Ion. 108 (1998) 129.
145. M. K. Rath, G. K. Pradhan, B. Pandey, H. C. Verma, B. K. Roul, S. Anand. Mat. Lett. 62 (2008) 2136.
146. M.W.H. Zhang, M.S.Yin. J. Korean Phys. Soc. 32 (1998) 1137.
147. A. García-Murillo, F. J. Carrillo-Romo, M. G arcía-Hernández, O. Barbosa-García, A. Meneses-Nava, S. Palomares-Sánchez, A. Flores-Vela. Mat. Trans. 50 (2009) 1850.
148. H. Kozuka, S. Takenaka. J. Am. Ceram. Soc. 85 (2002) 2696.
149. S. M. Gary, J. S. Costas, Fundamentals of Semiconductor Manufacturing and Process Control; Wiley-Interscience, A John wiley & Sons, Inc.: Hoboken, NJ, USA, 2006, p. 63.
150. V.S. Marques, L.S. Cavalcante, J.C. Sczancoski, D.P. Volanti, J.W.M. Espinosa, M.R. Joya, M.R.M.C. Santos, P.S. Pizani, J.A. Varela and E. Longo. Solid State Sci. 10 (2008) 1056.
151. EC Paris, MFC Gurgel, TM Boschi, MR Joya, PS Pizani, AG Souza, ER Leite, JA Varela, E Longo J Alloys Compd. 462(1–2) (2008) 157.
152. H. Kozuka and M. Kajimura, Chem. Lett., (1999) 10, 1029.
153. H. Kozuka and M. Kajimura, J. Am.Ceram. Soc., (2000) 83, 1056.
154. H. Kozuka, M. Kajimura, T. Hirano, and K. Katayama, J. Sol-Gel Sci. Technol., (2000) 19, 205.
155. H. Kozuka, M. Kajimura, K. Katayama, Y. Isota, and T. Hirano, Mater. Res. Soc. Symp. Proc., (2000) 606, 187.
156. Kozuka H, Katayama K, Isota Y, Takenaka S (2001) In: Feng X, Klein LC, Pope EJA, Komarneni S (eds) Sol–gel commercialization and applications, vol 123. American Ceramic Society, Westerville.
157. Urlich R, Torge R, Appl. Opt. (1973) 12, 2901.
158. S. Suzuki, M. Tanaka, M. Ishigame, Jpn, J. Appl. Phys., (1985) 26, 401.
159. H. Nishihara, M. Haruna, T. Suhara, Optical Integrated Circuits, McGraw-Hill, New York, (1985), p. 363.

160. N. Ledermann, P. Muralt, J. Baborowski, S. Gentil, K. Mukati, M. Cantoni, Seifert, and N. Setter, Sensors Actuators A, (2003) 105, 162.
161. Y. Kobayashi 1, A. Kosuge, M. Konno, Applied Surface Science 255 (2008) 2723.
162. H. Kozuka and A. Higuchi, J. Am. Ceram. Soc., 86 (2003) 33.
163. Hirimitsu Kozuka and Masahiro Kajimura, J. Am. Ceram. Soc. 83, (2000) 1056.
164. Wen-Chen Chien, J. of Crystal Growth 290 (2006) 554.
165. M. Yoshida and P. N Prassad, Mater. Res. Soc. Symp. Proc., 392 (1995) 103-108.
166. Jinbao Xu, Jiwei Zhai, Xi Yao, Jianqiang Xue, Zhiming Huang, J Sol-Gel Sci Techn 42 (2007) 209.
167. F. Vetrone, J. C. Boyer, J. A. Capobianco, A. Speghini, M. Bettinelli. J. Phys. Chem. B, 107-5 (2003) 1107.
168. O.S. Wenger, D.R. Gamelin, H.U. Gudel, A.V.Butashin, A.A. Kaminskii, Phys. Rev. B 60 (1999) 5312 .
169. L. Da-Yong, M. Sugano, S. Xiu-Yu, S. Wen-Hui, Applied Surface Science 242 (2005) 318.
170. M. Oku, K.Wagatsuma, S. Kohiki, Phys Chem. Chem. Phys. 1 (1999) 5327.
171. J.-P. Miao, L.-P. Li, H.-J. Liu, D.-P. Xu, Z. Lu, Y.-B. Song, W.-H. Su, Y.-G. Zheng, Mater. Lett. 42 (2000) 1.

APPENDIX. PUBLICATIONS

Publications related to this thesis

1. **Yb^{3+} Quenching Effects in Co-doped Polycrystalline $BaTiO_3$:Er, Yb**
   M. A. Meneses-Nava, O. Barbosa-García, J.L. Maldonado, G. Ramos-Ortíz, J.L. Pichardo, M. Torres-Cisnero, **M. García-Hernández**, A. García-Murillo, F.J. Carrillo-Romo. *Optical Materials* 31 (2008) 252–260.
   DOI:10.1016/j.matlet.2009.04.034 **ISSN:** 0925-3467

2. **Eu-doped $BaTiO_3$ powders and films from sol-gel process with polyvinylyrrolidone**
   M. García Hernández, F. Carrillo Romo, A. García Murillo, D. Jaramillo Vigueras, E. de la Rosa, G Chadeyron, D. Boyer, R. Mahiou.
   *International Journal of Molecular Science***,** Vol. 10 (2009) 4088-4101.
   DOI: 10.3390/ijms100x000x ISSN 1422-0067

3. **Structural and Optical Characteristics of $BaTiO_3$:Yb^{3+} powders**
   A. García Murillo, F.J. Carrillo Romo, **M. García Hernández**, O. Barbosa García, A. Meneses Nava, S. Palomares Sánchez, A. Flores Vela.
   *Material Transactions***,** Vol. 50, No. 7 (2009) 1850-1854.
   DOI:10.2320/matertrans.MRA2008407 ONLINE ISSN: 1347-5320, PRINT ISSN: 1345-9678

4. **The influence of polyvinylpyrrolidone on thick and optical properties of $BaTiO_3$:Er^{3+} thin films prepared by sol-gel method**
   M. García Hernández, A. García Murillo, F. de J. Carrillo Romo, D. Jaramillo Vigueras, M. A. Meneses Nava, P. Bartolo Pérez, G. Chadeyron
   Journal of Sol-Gel Science and Technology (2010) 53:246–254
   DOI: 10.1007/s10971-009-2084-1 PRINT ISSN: 0928-0707, ONLINE ISSN: 1573-4846

5. **Structural and morphological characteristics of polycrystalline $BaTiO_3$:Er^{3+},Yb^{3+} ceramics synthesized by the sol-gel route: Influence of chelating agents**
   A. García Murillo, F. J. Carrillo Romo, **M. García Hernández**, J. Ramírez Salgado, M. A. Domínguez Crespo, S. A. Palomares Sánchez, H. Terrones.
   Journal of Sol-Gel Science and Technology 53(2010)121-133
   DOI: PRINT ISSN: 0928-0707, ONLINE ISSN: 1573-4846

Other publications …

6. **Structural and luminescence characterization of silica coated $Y_2O_3:Eu^{3+}$ nanopowders**
   F. Carrillo Romo, A. García Murillo, D. López Torres, N. Cayetano Castro, V. H. Romero, E. de la Rosa, V. Garibay Febles, **M. García Hernández**
   Optical Materials 32 (2010) 1471–1479

7. **Synthesis of $Gd_2O_3:Eu^{3+}$ nanocrystallites emmbeded in SiO_2 using polyvinylpyrrolidone (pvp) by sol-gel process**
   A. García Murillo, F. Carrillo Romo, **M. García Hernández**, Juan C. Badillo, E. de la Rosa and Tzarara López-Luke
   Revista Mexicana de Física
   Accepted July, 2010

8. **Properties of $Gd_2O_3:Eu^{3+},Tb^{3+}$ nanopowders obtained by sol-gel process**
   A. de J. Morales Ramírez, A. García-Murillo, F.J. Carrillo-Romo, **M. García-Hernández,** D. Jaramillo-Vigueras, G. Chadeyron, D. Boyer.
   Materials Research Bulletin, 45 (2010) 40–45
   DOI: 10.1007/s10971-009-2069-0 **ISSN:** 0025-5408

9. **Synthesis, structural and optical studies of sol-gel $Gd_2O_3:Eu^{3+},Tb^{3+}$ films**
   A. García Murillo, A. de J. Morales Ramírez, F. Carrillo Romo, **M. García Hernández**, Miguel A. Domínguez Crespo.
   Material Letters 63 (2009) 1631–1634.
   DOI:10.1016/j.matlet.2009.04.034 **ISSN:** 0167-577X

10. **Sol-gel elaboration and structural properties of $Lu_2O_3:Eu^{3+}$ optical layers for X-ray imagery**
    García Murillo, F. de J. Carrillo Romo, C. Le Luyer, A. de J. Morales Ramírez, **M. García Hernández**, J. Moreno Palmerin.
    J. Sol-gel Sci. and Technol. Vol. 50 (2009) 359-367.
    DOI 10.1007/s10971-009-1929-y PRINT ISSN: 0928-0707, ONLINE ISSN: 1573-4846

11. **Preparation of $Y_3Al_5O_{12}:Eu^{3+}$ waveguide films by sol-gel method**
    A. García Murillo, Felipe de J. Carrillo Romo, N. Cayetano Castro, Claudia Torres Orozco, V. Garibay Febles, **M. García Hernández**, Esther Ramírez Meneses.
    *NSTI Nanotech 2009***,** ISBN 978-1-4398-1782-7 Vol 1 (2009) 383-386.